

An Electromechanical Hydrocephalus Shunting System

By:

OSMAN SALIH

A thesis submitted in partial fulfilment of the requirements of Liverpool John
Moores University for the degree of Doctor of Philosophy

June 2024

List of Content

List of Content	2
List of Figures	5
List of Tables	7
Abbreviations.....	8
Abstract.....	10
Acknowledgement.....	14
Chapter 1.....	15
INTRODUCTION	15
1.1 Introduction.....	15
1.2 Motivation.....	17
1.3 Aim and Objectives	19
1.4 Methodology	20
1.5 Contribution	23
1.6 Conclusion.....	24
1.7 Thesis Structure.....	25
Chapter 2.....	27
LITERATURE REVIEW.....	27
2.1 Introduction.....	27
2.2 Background Information.....	28
2.2.1 Shunt Valves.....	30
2.2.2 Current Shunt Systems Failures and Issues.....	37
2.2.3 Normal Pressure Hydrocephalus (NPH).....	40
2.3 Current Research	43
2.3.1 The Active Shunt	43
2.3.2 Advances in The Valve Mechanism.....	52
2.4 Conclusions.....	63
Chapter 3.....	65
ACTIVE SHUNT CONCEPT.....	65
3.1 Introduction.....	65
3.2 Main System Components	66
3.2.1 Pressure Sensing Unit.....	68
3.2.2 Body Position Sensing Unit.....	70

3.2.3 Controllable Valve	71
3.2.4 Power Source	72
3.2.5 Control Unit.....	74
3.2.6 Algorithm	74
3.3 System Layout.....	75
3.4 Conclusion.....	79
Chapter 4.....	80
VALVE MECHANISM	80
4.1 Introduction.....	80
4.2 ICP Dynamics.....	81
4.2.1 Mathematical Model	81
4.2.2 Dynamic Simulation Setup.....	85
4.2.3 Dynamic Simulation Results	88
4.3 Valve Concept.....	90
4.3.1 Valve Components.....	91
4.3.2 Valve Layout	94
4.4 Conclusion.....	97
Chapter 5.....	98
ELECTROMECHANICAL VALVE DESIGN	98
5.1 Introduction.....	98
5.2 Computational Fluid Dynamics (CFD) Analysis.....	99
5.2.1 CFD Model Setup	100
5.2.2 CFD Results.....	105
5.3 Spring Design	108
5.3.1 Initial Design	108
5.3.2 Finite Element Analysis (FEA).....	116
5.4 Ultrasonic Motor Design.....	120
5.4.1 Piezoelectric Materials	121
5.4.2 Modal Analysis.....	123
5.4.3 Dynamic Analysis.....	128
5.5 Conclusion.....	132
Chapter 6.....	135
NPH GAIT ANALYSIS	135
6.1 Introduction.....	135
6.2 Wearable Device Design.....	136

6.2.1 Device Components	136
6.2.2 Circuit Description	140
6.3 Wearable Device Assembly	142
6.4 Wearable Device Programming.....	146
6.5 Conclusion.....	148
Chapter 7.....	149
VALIDATION AND EVALUATION	149
7.1 Introduction	149
7.2 The Electromechanical Valve.....	150
7.2.1. Valve Validation	150
7.2.2. Valve Evaluation.....	156
7.3 The Wearable Device.....	164
7.3.1. Wearable Device Validation.....	164
7.3.2. Wearable Device Evaluation	172
7.4 Conclusion.....	176
Chapter 8.....	178
CONCLUSION	178
8.1 Conclusion.....	178
8.2 Limitations	180
8.3 Future Work	180
References	182
Appendix-1: Simulink ICP Model Blocks.....	190
Appendix-2: CFD Simulation Methodology.....	194
Appendix-3: Additional CFD Results	196
Appendix-4: Spring Mathematical Model	198
Appendix-5: Additional Spring Designs.....	200
Appendix-6: Additional Spring FEA Results	202
Appendix-7: Additional Modal Analysis Results.....	205
Appendix-8: Microcontroller C++ Code	207
Appendix-9: Python Code	208
Appendix-10: NPH Device Trial Design.....	211
Appendix-11: E. Valve Experiment Design	213

List of Figures

Figure 1.1: The choroid plexus and CSF brain circulation [7]	16
Figure 2.1: Cerebrospinal ventricular shunt system [47]	29
Figure 2.2: Differential pressure valves	31
Figure 2.3: The effects of hydrostatic pressure.....	32
Figure 2.4: Suction-controlled device	34
Figure 2.5: Flow-regulating device	35
Figure 2.6: Gravitational valve	35
Figure 2.7: Programmable valves [56].....	36
Figure 2.8: Momani et al. [10] proposed system layout.....	46
Figure 2.9: Alkharabsheh et al. [12] proposed system layout.....	46
Figure 2.10: Momani and Alkharabsheh [24] closed-loop scenario	50
Figure 2.11: Chung et al. [25] shunt design.....	52
Figure 2.12: Johansson et al. [13] shunt.....	53
Figure 2.13: Chappel [26] cylindrical valve	54
Figure 2.14: Webster et al. [27] shell valve	55
Figure 2.15: CSF drainage through the sagittal sinus.....	57
Figure 2.16: Passive miniature valves in current research.....	59
Figure 2.17: Miethk [35] patented valve design	63
Figure 3.1: Active shunt components.....	67
Figure 3.2: Different locations for sensor implantation for ICP monitoring [96]	69
Figure 3.3: Implanted hardware components of the active shunt.....	76
Figure 3.4: Data flow and components of the active shunt	78
Figure 4.1: Simulink simulation block.....	87
Figure 4.2: ICP shunting simulation results.....	89
Figure 4.3: Proposed electromechanical valve design layout.....	95
Figure 4.4: Butterfly and ultrasonic element valve concept	96
Figure 5.1: Parameters used for pressure calculation [132].....	102
Figure 5.2: Fluid compartment CFD model.....	104
Figure 5.3: CFD simulation results at 10 mmHg in the supine position.....	106
Figure 5.4: CFD simulation results at 20 mmHg in the standing position.....	107
Figure 5.5: Buckling relation to spring ends [136].....	111
Figure 5.6: Spring FEA model.....	117
Figure 5.7: Spring von-mises stress results.....	119
Figure 5.8: Spring maximum principal stresses at max loading condition	120
Figure 5.9: Piezoceramic element model	121
Figure 5.10: Piezoelectric phenomenon on a molecular level	122
Figure 5.11: Piezoceramic frequency analysis model	125
Figure 5.12: Piezoceramic sheet E (3,1) resonance mode results.....	127
Figure 5.13: Piezo element partial excitement model	129
Figure 5.14: Ultrasonic motor one-cycle step.....	130

Figure 5.15: Ultrasonic element tip displacement	131
Figure 6.1: Attiny 85 microcontroller [147]	137
Figure 6.2: HC-05 bluetooth module [148].....	138
Figure 6.3: ADXL335 accelerometer layout [149].....	139
Figure 6.4: NPH gait device circuit layout.....	141
Figure 6.5: Initial prototype of the wearable sensor.....	143
Figure 6.6: VOLTERA PCB printing machine	144
Figure 6.7: The printed PCB	144
Figure 6.8: Completed version of the wearable accelerometer-based sensor.....	145
Figure 6.9: PCB acceleration data gathering flowchart	147
Figure 7.1: CFD simulation mesh independence chart	151
Figure 7.2: FEA simulation mesh independence chart.....	153
Figure 7.3: Piezoceramic sheet deformation results.....	155
Figure 7.4: The electromechanical valve simulation block	157
Figure 7.5: Electromechanical valve dynamic modelling results	158
Figure 7.6: K2004E004 miniature shaker	165
Figure 7.7: Wearable device axes orientation.....	165
Figure 7.8: Acceleration results of the X-axis shaker test.....	168
Figure 7.9: Acceleration results of the Y-axis shaker test.....	169
Figure 7.10: Acceleration results of the Z-axis shaker test.....	169
Figure 7.11: Gait pattern filtered readings	171
Figure A1.1: CSF production volume block.....	190
Figure A1.2: ABP sine wave block	190
Figure A1.3: CSF reabsorbed volume block.....	191
Figure A1.4: Standard valve block.....	191
Figure A1.5: Closed-loop valve block.....	192
Figure A1.6: Blood volume block	192
Figure A1.7: Tissue volume block.....	193
Figure A1.8: Total volume block.....	193
Figure A1.9: ICP and total volume block	193
Figure A3.1: CFD simulation results at 12 mmHg.....	196
Figure A3.2: CFD simulation results at 15 mmHg.....	197
Figure A3.3: CFD simulation results at 18 mmHg.....	197
Figure A4.1: Model for the mass-spring-damper mechanical system.....	198
Figure A6.1: FEA principal stress results at 10 mmHg at the supine position.....	202
Figure A6.2: FEA principal stress at 20 mmHg at the supine position.....	203
Figure A6.3: FEA von-mises stress results at 20 mmHg at the supine position	203
Figure A6.4: FEA principal stress results at 10 mmHg at the standing position.....	204
Figure A6.5: FEA von-mises stress results at 10 mmHg at the standing position	204
Figure A7.1: Resonance mode of the $7 \times 3 \times 1$ piezoelectric sheet at 318 KHz.....	205
Figure A7.2: Resonance mode of the $13 \times 6 \times 2$ piezoelectric sheet at 81.9 Hz.....	206
Figure A7.3: Resonance mode of the $20 \times 9 \times 2$ piezoelectric sheet at 143 KHz.....	206
Figure A11.1: Electromechanical shunt valve experimental setup	215

List of Tables

Table 1.1: Objectives location within the thesis	26
Table 2.1: Summary of current research regarding the topic of active shunting.....	51
Table 2.2: Summary of current research on valve mechanism.....	61
Table 3.1: Solutions to passive shunting failures and required components.	66
Table 3.2: Different types of implanted batteries	73
Table 4.1: Parameters used for mathematical modelling of CSF	86
Table 4.2: Options available for shunt valve actuation.....	93
Table 5.1: CSF properties used for the simulation [129].....	100
Table 5.2: Electromechanical valve pressure points	103
Table 5.3: Force and flow results for ICP pressure points.....	108
Table 5.4: Design parameters for the spring design process.....	113
Table 5.5: Calculated spring parameters and properties	114
Table 5.6: ICP pressure points and their relative spring length.....	115
Table 5.7: PZT-5H properties	125
Table 5.8: Aluminium oxide properties	128
Table 5.9: Ultrasonic motor parameters.....	131
Table 5.10: Required voltage cycles for the setup of each pressure point.....	132
Table 6.1: ADXL335 accelerometer specifications	139
Table 7.1: CFD mesh independence analysis force output.....	152
Table 7.2: FEA measured reaction forces (RFs).....	152
Table 7.3: FEA mesh independence analysis force output	154
Table 7.4: Performance evaluation of the electromechanical valve.....	163
Table 7.5: Calibration values for the used accelerometer.....	168
Table 7.6: Evaluation of the wearable device.....	175
Table A5.1: Calculated spring parameters for a wire diameter (d) of 0.08 mm.....	200
Table A5.2: Calculated spring parameters for aluminium 6061-T6.....	201
Table A11.1: Upscaled electromechanical valve experiment components.....	213

Abbreviations

HC	Hydrocephalus
ICP	Intracranial Pressure
CSF	Cerebrospinal Fluid
NPH	Normal Pressure Hydrocephalus
iNPH	Idiopathic Normal Pressure Hydrocephalus
ETV	Endoscopic Third Ventriculostomy
VA	Ventriculo-atrial Shunt
DP	Differential Pressure
OP	Opening Pressure
MEMS	Micro-electromechanical Systems
STB	Snap Through Buckling
AGs	Arachnoid Granulations
PDMS	Polydimethylsiloxane
IPS	Inferior Petrosal Sinus
PCB	Printed Circuit Board
MRI	Magnetic Resonance Imaging
TCD	Transcranial Doppler Ultrasonography

NIRS	Near Infrared Spectroscopy
EVD	External Ventricular Drainage
ABP	Arterial Blood Pressure
VBP	Venous Blood Pressure
USE	Ultrasonic Element
PZT	Lead zirconate titanate
CFD	Computational Fluid Dynamics
SG	Specific Gravity
Re	Reynolds Number
BC	Boundary condition
FV	Finite Volume
FEA	Finite Element Analysis
RF	Reaction Force
ADC	Analogue to Digital Converter
UART	Universal Asynchronous Receiver / Transmitter
SPP	Serial Port Protocol
THM	Through-hole Mount
RC	Resistor-capacitor Circuit
AVR	Advanced Virtual RISC

Abstract

Hydrocephalus (HC) is a disease that occurs as a result of the increased cerebrospinal fluid (CSF) amount in the brain. The disease is managed by what is termed a shunt, which is a medical tool that is implanted surgically to divert CSF from the brain. As a result of their passive design nature, these shunts have multiple fundamental shortcomings and failures, causing considerable inconvenience and risks to the patient. The aim of this research is to design an agile and active HC management framework that is capable of addressing the shortcomings and failures of the currently used CSF shunts in the most convenient manner for the patient and to advance research regarding hydrocephalus management.

Thus, this work proposes an active patient shunting and monitoring system layout for CSF drainage and patient follow-up. The system layout is designed so that each component is put in place to address the shortcomings of passive shunts. To achieve this, the shunting system proposed is a closed-loop system that consists of multiple sensory inputs for patient monitoring and CSF drainage control to keep the patient's intracranial pressure (ICP) at the required level. As various studies looked at new shunting systems concepts from the perspective of algorithms, the novelty and focus of this work is on the hardware side of the active shunting system.

The proposed electromechanical shunting system's core hardware component is the valve it uses. Hence, this study provides a detailed design and methodology of a novel electromechanical valve. This is where the main gap of knowledge has been identified, as current research is still focused on passive valves. Mathematical modelling was conducted during the valve conceptualisation process. The results showcased that although current passive valves cannot address hydrostatic pressure effects, they are three times more active than automated valves and can generate a smoother pressure profile. Based on this, a novel concept

of a hybrid electromechanical valve that utilises an ultrasonic element attached to a ball-in-cone system is proposed. The design methodology of the valve components included the use of computer modelling, where forces inside the flow compartment were obtained using computational fluid dynamics (CFD). Spring sizing and ultrasonic element design were carried out using finite element analysis (FEA). The designed valve operates under a 3.5 V high-frequency current, has a 10 – 20 mmHg range, and can drain CSF up to 300 mL/h. The proposed electromechanical valve showcased that it possesses multiple features that the current passive valves do not. This includes malfunction detection, event recognitions, and wireless pressure settings revisions. Its main drawback is its lack of blockage management.

A wearable device was developed to diagnose and monitor normal pressure hydrocephalus (NPH) patients, as NPH is not associated with increased intracranial pressure (ICP). The device consists of a 3-axis ± 3.7 g accelerometer to measure gait patterns, an HC-05 bluetooth module, a 3.7 V battery, and an Attiny85 microcontroller. A functionality test was carried out on the device by conducting a vibrational analysis assessment using a miniature shaker. After calibration, the device proved that it could supply accurate acceleration data on all three axes. The device range, sensitivity, placement, and multi-axis use show that it may produce more accurate results compared to those used in the literature.

DECLARATION

This is the author's declaration that no portion of the work referred to in the thesis has been submitted in support of an application for another degree or qualification at this or any other university or other institutes of learning. Approvals were obtained for any materials used that require copyright permission.

Dedication:

This work is dedicated to my father, the best man I know. And to my mother, Batoul, for her support throughout my life. To my aunt Manal, My very first teacher.

Acknowledgement

There is a long list of individuals that the author would like to thank who assisted with different aspects of this project and were crucial to the completion of this work.

The author would like to first thank Dr. Marco Messina for his continuous help, guidance, and assistance, without which this work could not have been finished. I would also like to give him special thanks for his support and for being a supportive supervisor and a friend through these five years.

Special thanks to Prof. Dhiya Al-Jumeily. He is an experienced professor with a wealth of knowledge in the e-health field. I would like to thank him for helping me navigate and network within the neurology sector.

Particular Thanks to Catherine McMahon of the Walton Neurological Centre. She was of great assistance in understanding the physiology of NPH and its diagnosis process. Her feedback on the design and shunting process was of great value.

Many thanks go to Prof. Conor Mallucci of the Alder Hey Children's Hospital. His point of view and technical feedback on the design and specs of the shunts were of great importance.

The author acknowledges that the idea of this project was conceived by Dr Mohammed Al-Jumaily, Prof. Conor Mallucci, and Prof. Dhiya Al-Jumeily and their respective teams.

Osman Salih

Liverpool, UK

June 2024

Chapter 1

INTRODUCTION

1.1 Introduction

Hydrocephalus (HC) is defined by Leinonen et al. [1] as the disorder caused by “the dynamic imbalance between the production and absorption of cerebrospinal fluid (CSF) leading to enlarged ventricles”. It is simply the result of increased CSF amount in the ventricles caused by a disruption in flow, absorption, or formation [2,3]. CSF is a colourless transparent liquid that plays an essential role in protecting the brain and neural tissues by serving as a cushioning medium. It also carries away toxic chemical products resulting from metabolism [2]. The choroid plexus forms about 70%-80% of CSF being cycled in the brain [1,2,4]. Statistics show that HC is prevalent in 85 per 100,000 of the overall global population. However, these statistics significantly change when considering age groups, as the condition occurs in 88 per 100,000 paediatric population and 11 per 100,000 adults [5]. Statistics are even higher in the case of the elderly population, as HC occurs in 400 per 100,000 elders above 80 years old.

Figure 1.1 shows the circulation and production of CSF in the brain. It is formed at a rate of 500 ml/day, where the total amount of CSF in an adult body is about 120-150 ml. This shows that CSF is recycled around three times per day [3]. The normal intracranial pressure (ICP) is between 5 and 15 mmHg in the supine position and between -5 and +5 mmHg in the standing position [1]. This difference is the result of siphoning effects [6].

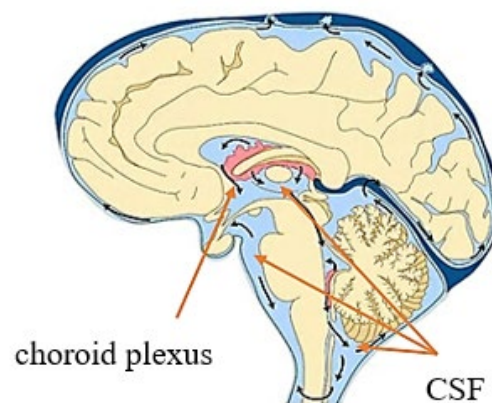


Figure 1.1: The choroid plexus and CSF brain circulation [7]

Hydrocephalus is classified based on numerous aspects, which include (i) acute (temporary) versus chronic HC, (ii) acquired versus congenital (present from birth), and (iii) communicative versus obstructive [1,2]. The latter classification is considered the most important as it depends on the flow of CSF. If there is no apparent blockage impeding CSF flow but rather an issue with its absorption, it is considered a communicative HC. However, if there is a blockage in the flow of CSF, it is considered obstructive. Simply put, HC is considered communicative if CSF is able to leave the ventricular system and obstructive if it is not [2,4,6,8]. Chronic HC in adults is sometimes called Normal-Pressure HC (NPH) as it slowly develops over time. When the causality – such as brain trauma or haemorrhage – of NPH is known, it is termed secondary NPH (sNPH). When there are no known causes for NPH, it is termed idiopathic NPH (iNPH), which is the most common form of HC in adults [1].

Diagnosis of HC starts with the symptoms which differ for infants, older children, young adults, and the elderly. Generally, symptoms can include vomiting, headache, drowsiness, reduced mental capacity, dementia, gait, and increased head circumference [1,6,8]. Compiling symptoms by using investigative pieces of equipment is used to diagnose HC. Computerised tomography (CT) is used to evaluate the size of the ventricles and compare them with the size

range for normal ventricles [3,4]. Also, magnetic resonance imaging (MRI) can detect tumours that are sometimes not visible to CT scans and can detect flow voids in the third ventricle. ICP can also be monitored using CSF infusion tests that keep track of the pressure status inside the brain [3,8].

HC is currently managed using passive drainage devices known as shunts. They are medical tools that are implanted surgically to divert the flow of CSF from the brain ventricular system to a suitable drainage site for absorption [9]. These passive shunts have been in use since the 1980s, when the last major development took place with the introduction of adjustable shunts. These shunts have multiple opening pressure settings and can be non-invasively adjusted.

1.2 Motivation

As mentioned, HC is managed using shunts consisting of passive valves that drain CSF into specified locations. They have fundamental issues and failures related to their design and nature of operation. These issues include over/under drainage, lack of proactivity as it does not reflect the changes the patients undergo as their condition evolves, increased shunt dependency, and late detection of malfunctions [7,10–13]. Other issues include the high revision rates these passive shunts require, negatively affecting both the shunting costs and patients' quality of life. Statistics show that around 58% of shunt operations are for revisions as opposed to first-time installation. Patients tend to ensure they remain near their neurosurgical clinic as shunt adjustments are frequently needed. The shunting surgical operation costs around £8,500 to £10,200 per surgery, where an adjustable shunt costs about £2,300 and a fixed one is about £1,100 [14–16]. Overall shunting costs from hospital admission to discharge are estimated to be between £30,000 and £64,000 [17,18]. In addition, shunt revisions and adjustments are estimated to cost around £6,000 to £17,000 per patient per year [19].

A gap in knowledge exists when it comes to the methods by which the issues and failures of current CSF shunts can be addressed. However, there is an agreement in the scientific community that automated and active shunting is the way forward in the attempt to resolve these issues. Although the notion of active shunting is not new, attention to research and innovation around the topic has been lacking as most of the literature regarding the topic is on the conceptual level and is focused on algorithms [10,12,20–24]. Specifically, there is a lack of development regarding the hardware needed for the operation of an active shunt, such as a controllable electromechanical valve.

Several studies produced other types of passive valves for shunts [13,25–32]. Some of these new designs make use of silicon membranes and are planted near the brain to navigate the operational issues with current shunts. Others have a built-in blockage removal mechanism, and some attempt to combat the over-drainage issue. However, all these new designs are shown to possess most of the fundamental issues mentioned above. The cause for this lack of innovation is mainly a result of the small market of HC shunts compared with other neurosurgical devices [33]. This can be clearly seen in the case of ICP sensors, where great attention has been given to them because ICP monitoring is not only of importance for hydrocephalus patients but also necessary for head trauma, intracranial haemorrhage, subarachnoid haemorrhage from ruptured brain aneurysms, and intracranial tumours. Another factor in the lack of research – specifically regarding electromechanical valves – could be the actuation method. Traditionally, physical movement is delivered in controllable systems using magnetic actuation. However, the implantability, miniaturisation, tolerance, precision, and the effects of such a method – magnetic fields – on patients is a point of question [34]. Currently, all work surrounding the idea of active shunting is on the conceptual level, as only two research teams – Miethke [35] and Ludin and Mauge [36] – have a conceptual design of an electromechanical valve that an active shunt would need to function properly.

It must be noted that despite active research on hydrocephalus, the exact underlying mechanism of how it occurs – the reasons behind CSF flow disruption – is not yet fully understood [1,37]. An active shunting system would offer new insight into the condition as the constant monitoring and sensory output can generate large amounts of data that can improve clinical understanding of HC.

This research attempts to investigate and advance the research on the active shunting topic by proposing a layout for such a system. The research provides a novel approach to managing HC patients based on their needs and the feedback of NHS physicians by utilising the concept of active shunting. It provides the design and evaluation of a hybrid electromechanical valve that can be used in such an active shunting system, considering different criteria and operating conditions.

1.3 Aim and Objectives

This research aims to design an agile and active HC management framework that is capable of addressing the shortcomings and failures of the currently used CSF shunts in the most convenient manner for the patient and to advance research regarding hydrocephalus management. The different parts of this framework, the nature and components of its shunting system, and its ability to manage all types of HC are major research questions. Thus, the objectives necessary to achieve this research aim are:

- a. To produce a novel active shunting system layout that can keep ICP at desired levels, consider the influence of patient movements and body position, and combat unnecessary drainage resulting from ICP spikes causing events such as coughing and sneezing. Such a system needs to be a closed-loop system that uses sensory input in the decision-making process.

- b. To conduct mathematical simulations regarding ICP response when CSF is managed using passive and automated shunt valves in order to understand their operational differences, such as their level of activeness and accuracy. This is crucial for constructing an appropriate design concept for the electromechanical shunt and selecting both fluid diversion and actuation mechanisms.
- c. To design the electromechanical valve responsible for CSF drainage, which consists of three major design steps. These are fluid compartment sizing, spring specification design, and actuator operation analysis. The design process is carried out using a combination of computer modelling and general design methods. The valve must be compatible with the active shunting system mentioned above.
- d. To design, prototype, and assemble an accelerometer-based NPH gait analysis wearable printed to aid with diagnosing and monitoring NPH patients by identifying the patient's gait pattern before and after CSF drainage. This is achieved by selecting the necessary components – such as microcontrollers and accelerometer type – for the sensor to function and then implementing a code on both the sensor and machine end to produce, stream, and handle data. Those selected components are then assembled on an in-house manufactured printed circuit board (PCB) in a specific layout.

1.4 Methodology

As mentioned above, the proposed HC management framework relies on the concept of active shunting. The first step is to point out the specific issues with current shunts that the active shunt system must address. This is achieved by conducting an extensive review of used systems and current active research. The active shunting system layout is based on the identified failure points of current systems, where different components are added to the system to address or negate one or more of these failure points. In addition to addressing these issues, the active

system must carry on with its main tasks of CSF drainage and ICP management. The conducted review and the proposed active shunting system layout showcased that the core component of this system is the shunt valve. This electromechanical valve is the area where research is most lacking and where the gap in knowledge has been identified. In addition to diverting CSF, the valve is a crucial component that defines the system's nature, layout and operation.

A new design of the electromechanical valve must be conceptualised first, which is carried out with the aid of mathematical models that showcase how different valves manage CSF. The hydrodynamics of CSF are modelled using Anthony Marmarou's theory. The electromechanical valve design options are reviewed based on the outcome of these models. The option with the most optimal features is selected. These features refer to valve activeness level, ability to combat hydrostatic pressure, ability to keep ICP at the required levels, and power draw.

The design process of the conceptualised electromechanical valve in the previous stage is sectioned into three design steps. Each step is concerned with the design of one of the valve components. The first step is the design of the CSF flow chamber, which is carried out by conducting a computational fluid analysis (CFD). The results of this analysis are then used in the second step, which is concerned with designing the spring system of the valve. The spring design relies on finite element analysis (FEA) computer simulation and general design formulas. The last step is designing the ultrasonic piezoelectric motor used to actuate the valve system. The motor design is carried out by conducting a modal analysis (frequency analysis) to obtain the operating frequency of the piezoelectric actuator. A dynamic analysis is then conducted by utilising that operating frequency to find out the resulting motor properties and parameters such as speed, step definition, and operating voltage.

It is important to ensure that the proposed HC management framework is able to manage all types of HC, including NPH. The active shunting system is not able to monitor NPH patients as their condition is not associated with elevated ICP. Since NPH is not monitored the same way as average HC, a different method is required to monitor and diagnose the condition. As gait disorder is the most prevalent symptom in NPH patients, an accelerometer-based wearable device is developed. Multiple components – such as a micro controller and a 3-axis accelerometer – are used to ensure that this device can measure gait data. These components are assembled on a printed circuit board (PCB) in a designed layout. The device is programmed to gather and stream gait data to a nearby computer that utilises a Python script to manage, plot, and store data. The wearable is first prototyped, and an initial version is produced to ensure the operation of components and the validity of the code used to operate it.

The last step is validating and evaluating both the designed electromechanical valve and the developed wearable gait device. The validation of the valve is carried out by validating each one of the three design steps mentioned earlier, either by verifying the simulation results or by comparing the obtained results to other studies. The valve is then evaluated based on how many of the fundamental failures with current shunts the valve manages to negate compared to other types of valves researched in the literature.

The gait device is validated by conducting a functional vibrational analysis test. This test can confirm the accuracy of the data obtained by the device during operation. The device is validated by measuring its parameters – such as range, sensitivity, and data type – against other gait devices available in the literature.

Further details on the exact methodology of each step are available in each chapter's introduction.

1.5 Contribution

The contribution of this research can be summarised as follows:

- a. Provided a concept for an active shunting system layout that consists of a catheter tip implanted ICP sensor, a 3-axis accelerometer, a controllable electromechanical shunt valve, and a control unit. The system can resolve the shortcomings of currently used shunts and can stream ICP data to the hospital database. Its settings can be changed remotely to reduce patient and physician inconvenience. This was published in a conference paper titled “Smart Shunting and Monitoring of Hydrocephalus Patients” [38].
- b. Provided a detailed design and methodology of a novel electromechanical shunt valve that can be used as a part of the proposed active shunting system. The valve consists of a fluid compartment, a linear spring, and an ultrasonic element that is used to actuate the system. The valve is hybrid in nature, possessing both the activeness advantages of passive valves and the accuracy and controllability of automated valves. This is the most crucial section of the research as the design is novel since no valve is available in either the literature or the market that offers this controllability feature. The valve has an operational range of 10 – 20 mmHg, a speed of 1 mm/s, a step definition of 4 nm, and operates with a 5 V input. Based on this, a conference paper titled “An Intelligent Hydrocephalus Shunt: A New Concept” [39] and a journal paper titled “Design of a Piezoelectrically Actuated Hydrocephalus Shunt Valve” [40] were published.
- c. Developed a wearable ankle-attached sensor that can analyse NPH patients' gait for use during both diagnosis and patient monitoring. It can generate acceleration data – 3-axis acceleration patterns – that can assist physicians in performing gait tests on patients. The sensor generates gait data using a 3-axis accelerometer and then streams

data to a nearby computer. The sensor can read acceleration values up to ± 3.7 g and has a sampling rate of 100 Hz.

1.6 Conclusion

Hydrocephalus is a condition that results from the excess amount of CSF in the brain and is currently managed through passive mechanical devices called shunts. The aim of this research is to challenge the failures, shortcomings, and issues surrounding these passive mechanical shunting systems. This is achieved by proposing a layout for an active shunting system that keeps ICP at the desired level and mitigates the effects of patient movement and sudden ICP spikes causing events. This system is intended to be a closed-loop system, which requires it to make use of multiple sensory inputs. The system's main component is a shunt valve that can be controlled electronically to achieve the required drainage.

This electromechanical valve is considered the fundamental part of the system and is the area where knowledge is most lacking. Thus, it is given greater attention as it is considered the core of this research. A design process is followed to develop this valve, starting with understanding how automated valves handle CSF drainage compared with passive valves. Detailed design and analysis are conducted on each component of the valve. This included the use of dynamic modelling, computational fluid dynamics, and finite element modelling. The valve has the characteristics of a passive and an automated valve, which are achieved using a spring system controlled by an ultrasonic element. The design is compatible with operation conditions associated with an implanted system.

Due to the fact that NPH is not associated with an increase in ICP, a wearable sensor is developed to aid with the diagnosis and monitoring of NPH. Additional sensory input is necessary to monitor the progress of NPH patients. This is achieved through gait monitoring using the accelerometer-based wearable sensor.

1.7 Thesis Structure

This thesis is structured into seven chapters, starting with the current introductory chapter that showcases the research background, aim, and objectives. Chapter two is a literature review of practices used to manage hydrocephalus and current CSF shunts. Research around the topic of active shunting and shunt valves is reviewed in this chapter.

Chapter three contains an overview of the active shunting system layout and components. It explains the rationale behind the chosen system layout. Chapter four shows the dynamics of different valves and their management of CSF drainage and ICP control. A mathematical model is simulated to understand the difference between automated and passive valves, as it is necessary to improve the design process of the electromechanical valve and is considered the first step in that process. Chapter five outlines the entire design process of the electromechanical valve. It contains three main sections where a CFD analysis of CSF flow, the design of the spring mechanism, and the design of an ultrasonic element actuator are carried out. This chapter is considered the main section of the thesis. Chapter six showcases the wearable device design required for diagnosing and monitoring NPH patients. It shows the design and components of the accelerometer-based wearable device. Chapter seven showcases the validation and performance evaluation of both the designed electromechanical valve and the wearable sensor. Simulation and general engineering techniques – in addition to vibrational testing – are carried out in this chapter.

Chapter eight is the conclusion, where the thesis findings are outlined and summarised. Future work regarding the thesis topic is suggested, and any limitations of the study are discussed. Table 1.1 shows the locations of the objectives mentioned above within the thesis.

Table 1.1: Objectives location within the thesis

NO.	Objective	Chapter
(a)	Active shunting system layout	Chapter Three
(b)	ICP mathematical Simulation	Chapter Four
(c)	Electromechanical valve design	Chapter Five
(d)	Wearable device development	Chapter Six

Chapter 2

LITERATURE REVIEW

2.1 Introduction

The two main methods to approach hydrocephalus are medical management and surgical intervention. The condition is medically managed through diuretics such as furosemide and acetazolamide, as they can reduce the production of CSF since they are inhibitors of the carbonic anhydrase enzyme, which is an essential enzyme for the production of CSF found in the choroid plexus. Although it is usually the first option to consider, this process has minimal and unsustainable effects as it may be able to reduce CSF but not reduce ICP due to the inhibitor's effect on cerebral vessels and blood flow in the cerebrum [4,37]. There are two common approaches for the surgical intervention method, both of which are considered long-term options. The first one is Endoscopic third ventriculostomy (ETV), in which an endoscope is placed within the ventricular system to generate an opening in the floor of the third ventricle. This creates a fistula between the third ventricles and the subarachnoid space in front of the brainstem. Although ETV has the attraction of relieving the patient of the complications – discussed later – associated with the use of CSF shunts, the literature states that it is considered ineffective in children under one year of age and most effective in adults with obstructive HC. It also states that the long-term success of ETV depends highly on the cause of HC, as certain tumours react differently to it than others [3,4,37,41]. The second approach to surgical intervention – and the focus of this study – is HC management through the use of CSF shunts.

This chapter outlines present-day practices and currently used shunts, including their types, operation methods, and their shortcomings. The current research and advances regarding shunts are also discussed and summarised.

2.2 Background Information

A shunt is a medical tool that is implanted surgically to divert the flow of CSF from the brain ventricular system to a suitable drainage site for absorption. It provides a uni-directional controlled flow of CSF from the brain [9]. The two general types of shunts are the lumbar-peritoneal shunts (LP) and the ventricular shunts. The LP shunt is designed to drain CSF from the lumbar thecal sac into the peritoneal cavity (the abdomen). The ventricular shunt – shown in Figure 2.1 and is the focus of this study – drains CSF directly from the brain ventricular system and is placed inside the head of the patient [42]. It must be noted that both shunts are opened-loop, purely passive mechanical systems. There are three main components of the ventricular shunts which are:

- a. The shunt valve:** This is the core component of the shunt – shown in Figure 2.1 – as it controls the CSF drainage process. These valves range from types based on their mechanism to types based on their pressure settings. The common classification – discussed further in section 2.2.1 – is based on whether they are fixed single-pressure point valves or adjustable valves.
- b. The proximal catheter:** This is the component – shown in Figure 2.1 – responsible for draining CSF from the ventricular system in the brain. The catheter is basically a tube that has a titanium tip on the ventricular end. As one of the common causes of shunt failure is the obstruction of the proximal catheter, many catheter end (tip) shapes – such as straight, flanged, and J-shaped ends – were designed to minimize the chance of obstruction due to debris. However, it was found that these shapes have a very minimal effect on the blockage

in the proximal catheter. The catheter's length ranges between 15 and 23 cm, with an inner diameter between 1 and 1.6 mm and an outer diameter between 2.1 and 3.2 mm [43,44].

c. The distal catheter: This component – shown in Figure 2.1 – is responsible for delivering the CSF into the drainage site. One of the ventricular shunt classifications is based on the drainage site, where the peritoneum (abdomen) and the heart's right atrium are the two common draining sites. The upper is termed ventriculo-peritoneal shunt (VP), and the latter is termed ventriculo-atrial shunt (VA). Other drainage sites used include the pleural cavity, where the shunts used for this site are termed ventricular-pleural (VPL) [45]. The catheter length ranges between 90 and 120 cm, with an inner diameter between 0.7 and 1.3 mm and an outer diameter between 2.1 and 2.5 mm. Draining holes are found toward the end of the catheter (the drainage end) and are between 0.25 and 0.5 mm in size and about 1 to 1.5 cm from the distal tip [43,44,46].

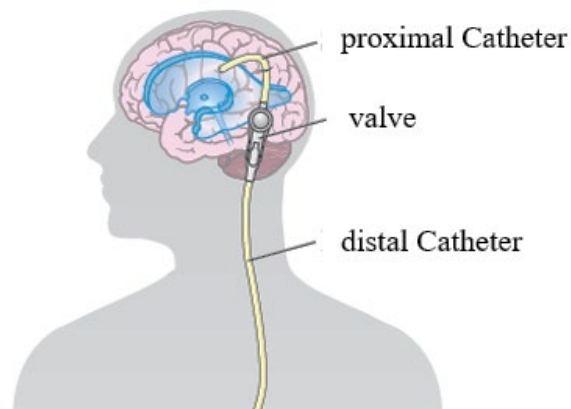


Figure 2.1: Cerebrospinal ventricular shunt system [47]

In terms of the material used for the catheter, early-stage versions used materials such as rubber and silver wires. They proved unsuccessful as they were bio-incompatible and released toxins into the tissues. Silicon was then found to be non-reactive with human tissues and has been

used in shunts since 1956 [46]. However, the main issue with silicon is its hydrophobic nature, which causes it to absorb bacteria to its surface, causing infections. Some methods were adopted to navigate this issue, such as coating silicon with polyvinylpyrrolidone (PVP) to make it hydrophilic. As a result, water moulded around the catheter and stopped bacterial colonisation but made the catheter very smooth and slippery. Thus, this method was eventually abandoned as it caused the catheter to detach from the connectors easily. Another method involved the use of an antibiotic-impregnated catheter (AIC) through embedding antibiotics with the silicon in the catheter [45]. Other practices included coating both the proximal and distal catheters with barium, making them visually apparent on X-ray images. However, the barium results in a higher calcification rate, which makes the catheters more susceptible to breakage [44,45].

2.2.1 Shunt Valves

The valve is considered the main component of the shunt and is responsible for regulating the flow of CSF and ensuring that it is uni-directional. The main types of valves are:

- a. Fixed differential pressure valves (DPV).
- b. Hydrostatic valves (HSV).
- c. Programmable (adjustable) valves.

a. Fixed differential pressure valves (DPV)

DPVs are the first-generation valves designed and used to manage CSF. Their operation is based on the difference between the intracranial pressure (ICP) and the drainage site pressure (differential pressure (DP)). These valves have an opening pressure (OP) at which the valve opens, allowing the flow of CSF toward the distal end. This indicates that the valve remains closed until DP is higher than OP, and only then will CSF be allowed to flow across the valve. Other types of these valves operate based on closing pressure (CP), as the valve remains open

until DP is lower than CP [48]. One of the types of DPV valves is the slit valve shown in Figure 2.2a, which consists of a slit opening placed at the end of a tube. As the pressure increases and DP exceeds the designed OP – Figure 2.2b – of the valve, the slit opens. Another type is the ball-in-cone valve, which consists of a spring that holds a metallic ball – Figure 2.2c – to block the opening. As DP rises above the valve designed OP, the opening is gradually unblocked by the metallic ball – Figure 2.2d – allowing CSF to flow. Lastly is the diaphragm valve, which consists of a diaphragm positioned to close an opening. This diaphragm remains to block the opening – Figure 2.2e – until DP exceeds OP, at which point it unblocks the opening – Figure 2.2f – and allows CSF to flow [45].

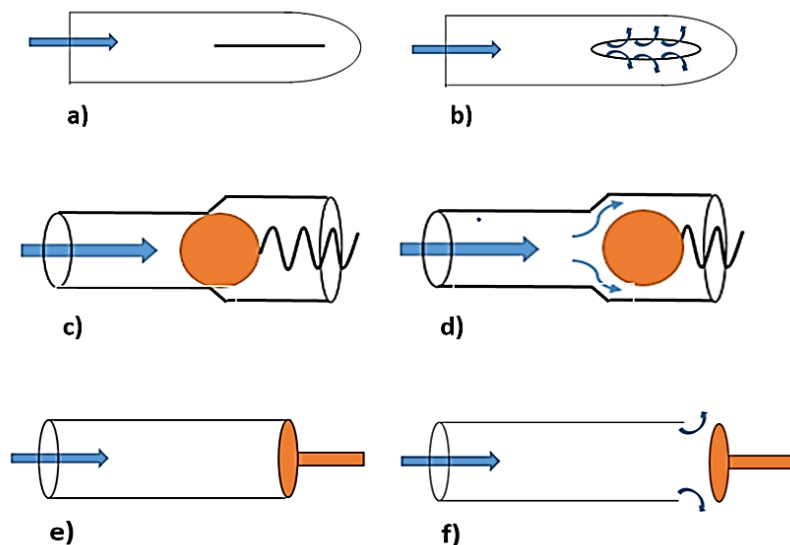


Figure 2.2: Differential pressure valves. (a) Closed slit valve ($DP < OP$). (b) Opened slit valve ($DP > OP$). (c) Closed ball-in-cone valve ($DP < OP$). (d) Opened ball-in-cone valve ($DP > OP$). (e) closed diaphragm valve ($DP < OP$). (f) Opened diaphragm valve ($DP > OP$)

The main shortcoming of DPVs is the fact that they are fixed-pressure valves. Thus, if any change in the patient's status that may require an alteration in the optimal amount of CSF to be drained occurs, the valve must be changed surgically. This is even more problematic for children as they are developing individuals with constant changes to their bodies [49,50]. This becomes more of an issue when the effect of hydrostatic pressure comes into account. Assuming a patient is in the supine position and suddenly stands, the CSF column's weight causes an increased ICP pressure. This leads to an increased DP, causing the valve to open, resulting in over-drainage (siphoning effect) [48,51].

b. Hydrostatic Valves (HSV)

HSV valves – also termed anti-siphon valves – emerged from the need to address the hydrostatic pressure effect in DPVs in order to prevent over-drainage [51]. Figure 2.3 showcases how when a patient with an HC shunt is supine, the height difference between the intracranial cavity and the drainage site is minimal, so the drainage occurs slowly. When the patient stands up, the difference in height between the drainage site and the intracranial cavity increases. This results in a rapid rise in hydrostatic pressure, causing an increase in CSF flow. This results from the CSF column's weight acting on the valve inlet [44].

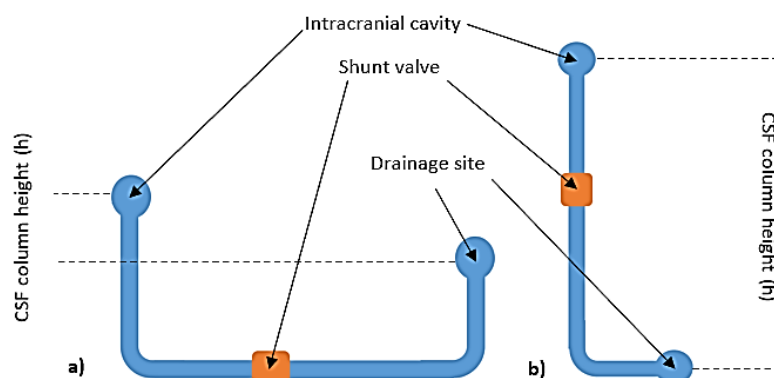


Figure 2.3: The effects of hydrostatic pressure. (a) The supine position where hydrostatic pressure is minimal. (b) The standing position as the weight of the CSF column is significant

HC shunt valves operate using differential pressure between the valve's inlet and outlet. The hydrostatic pressure is taken into account as follows:

$$OP = ICP + \rho gh - DSP \quad \text{eq 2.1}$$

Where OP is the valve opening pressure (mmHg), ICP is the intracranial pressure (mmHg), and DSP is the drainage site pressure (mmHg). The term ρgh represents the hydrostatic pressure where ρ is CSF density (g/cm^3), g is the acceleration due to gravity (m/s^2), and h is the height of the column of CSF (cm) representing the distance between the cranial cavity and the drainage site. Depending on the drainage site (heart or abdomen) and the patient's body dimension, h is usually between 10 and 40 cm. The introduction of the HSV was required to combat this issue, and they are divided into three types discussed below.

The first type is suction-controlled devices showcased in Figure 2.4 that contain a flexible film or membrane so that the flow is blocked – Figure 2.4a – when the patient is supine with DP lower than OP. The film stretches – Figure 2.4b – outward when DP exceeds OP, permitting CSF to pass through. The sudden increase in ICP pushes the film's upper half outward when the patient stands, with the lower half of the film sucked inward due to the siphoning effect. This makes the device block the path of CSF flow – Figure 2.4c – when a pressure rise occurs. Some of the drawbacks of this device are that it needs to be positioned perfectly for the siphoning pressure to be equal to the ICP pressure, and the flexible nature of the film makes it vulnerable to external pressure [44]. The second type is flow-regulated devices that keep the flow constant by controlling the resistance of the shunt to CSF flow [51]. One type of these flow-regulated devices is the binary flow control device shown in Figure 2.5. There are two pathways for CSF to flow in this device, which are the low – the small coiled tube – or the high – the ball-spring system – resistance pathway. The flow goes through the low-resistance – Figure 2.5a – pathway when the patient is supine. When the patient stands, the high pressure

and flow push the ball into the hole, closing the low-resistance pathway and forcing CSF to take the high-resistance – Figure 2.5b – pathway [44,52]. One of the drawbacks of this system is that due to the small diameter of the coiled tube, it is very susceptible to blockage by monocytes (large white blood cells) [44]. The third type is the gravitational valves presented in Figure 2.6. They work by using two to four metal balls to control the flow of CSF. The way they operate is that when the patient is supine, the CSF flows normally – when DP exceeds OP – through the first chamber – Figure 2.6a – with the ball-spring system. The second chamber pathway is open as the metal balls system does not block the opening in this position, allowing CSF to flow normally through the second chamber. When the patient stands, the CSF flows through the first chamber as normal. However, due to gravity, the metallic balls close the opening to the second chamber –Figure 2.6b – in this position. This means that the OP has been increased in this position, which in turn counters the HSP [53]. When installed, the longitudinal axis of these devices must be parallel to the spine [54].

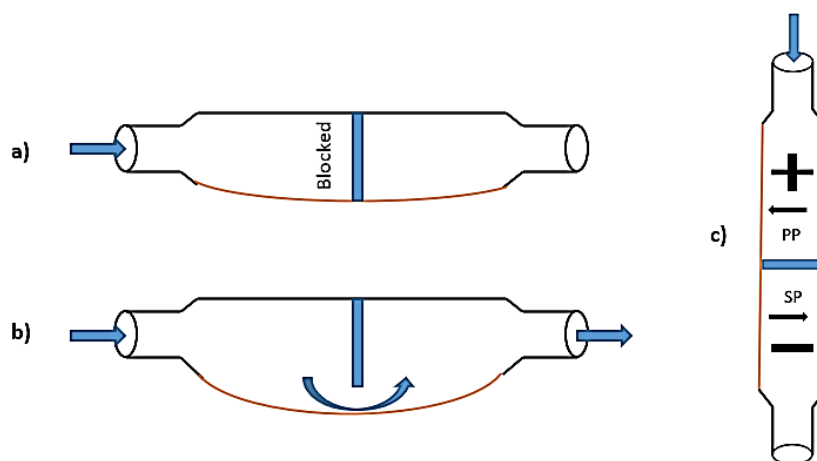


Figure 2.4: Suction-controlled device. (a) The patient is supine with $DP < OP$. (b) The patient is supine with $DP > OP$. (c) When the patient stands. PP represents the positive pushing pressure, and SP represents the negative sucking pressure

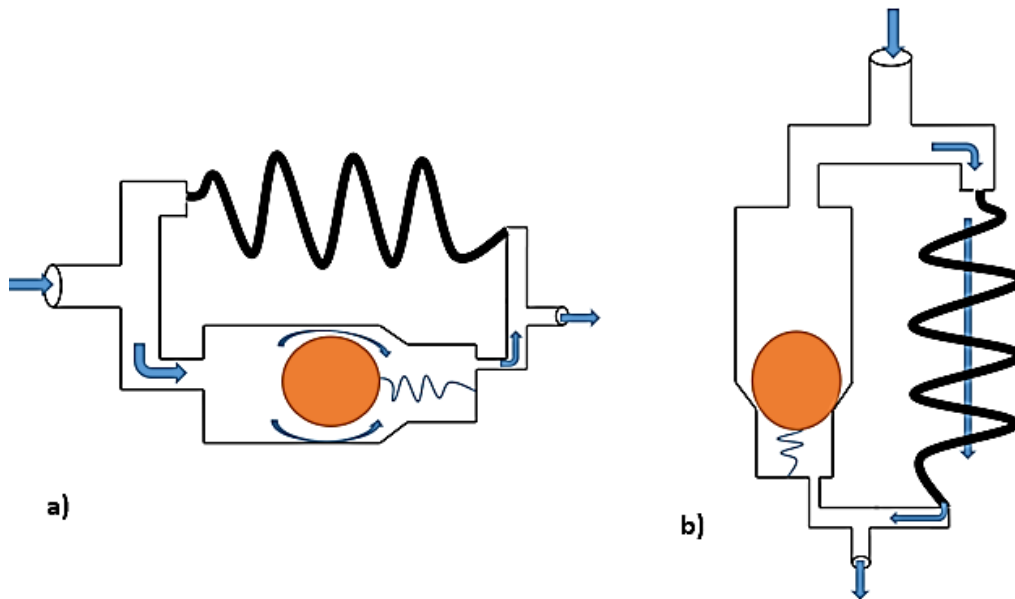


Figure 2.5: Flow-regulating device. (a) The patient is supine, so CSF is going through the low-resistance path. (b) When the patient stands, the ball closes the low-resistance path, causing CSF to take the high-resistance path

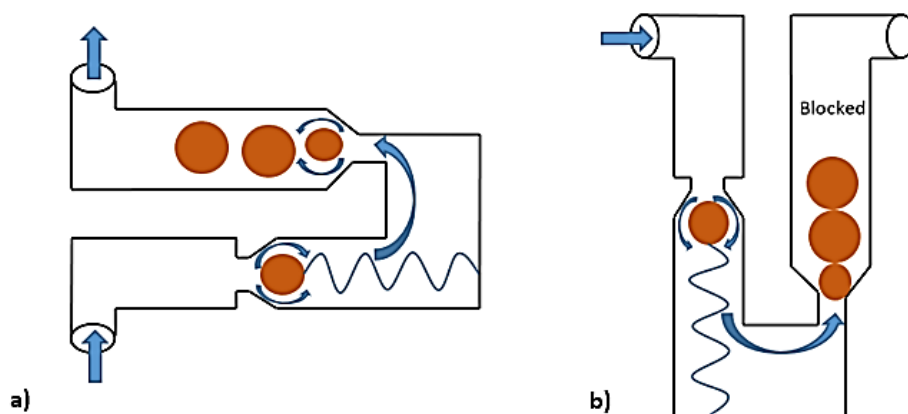


Figure 2.6: Gravitational valve. (a) The patient is supine, so CSF flows through both chambers when $DP > OP$. OP is only related to the ball in the first chamber. (b) When the patient stands, the new higher OP is related to the steel balls in the second chamber blocking CSF

c. Programmable (Adjustable) Valves

Adjustable valves were developed in the late 1980s to address the fixed-pressure issue with DPVs. The term “programmable” is not in any way related to computer programming, as these valves are basically DPVs with the feature of changing their OP non-invasively. A rotating magnetic system – Figure 2.7a – is used to control the active length of the spring attached to the ball. This causes the stiffness of the spring to change, thus controlling the OP of the valve. This removed the need for surgery to change the valve when different pressure settings were needed [50,51]. One example is the Sophy® Mini SM8 adjustable valve that comes in four different ranges (0.5 – 3, 2 – 15, 3.5 – 22, 5.5 – 30) mmHg, each with eight pressure steps [55]. However, it must be noted that once the pressure is set, the adjustable valve performs as a fixed DPV valve with an OP that controls CSF flow. This means that over- or under-drainage can still occur. Furthermore, these types of valves use an external magnet – as seen in Figure 2.7b – to change the OP of the valve, which can be problematic when MRI is used on a patient as it interferes with valve settings [45].

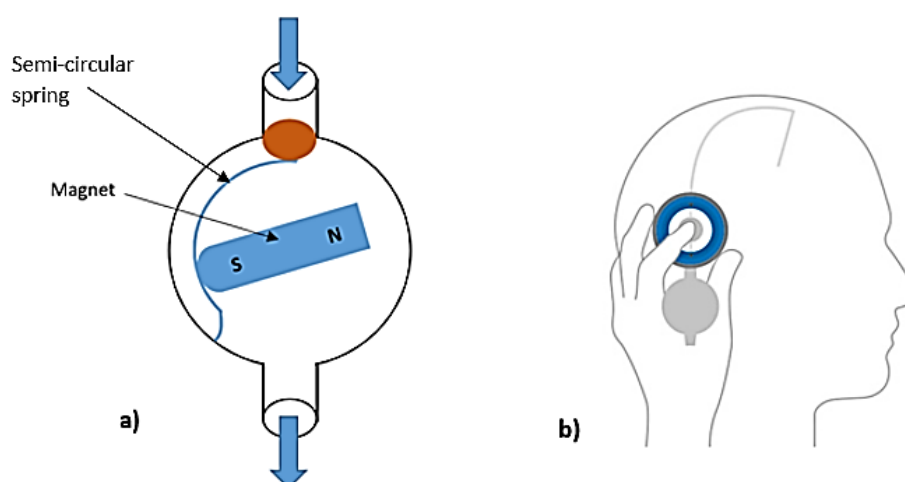


Figure 2.7: Programmable valves [56]. (a) adjustable valve where the opening pressure is controlled through a semi-circular spring. (b) External magnetic adjustment tool

2.2.2 Current Shunt Systems Failures and Issues

Shunt failures and issues are divided into two main categories. The first is fundamental issues related to the nature of the design of these shunts, as they represent inherent issues and flaws shared between all types of shunts currently in use. The second category is operational issues related to normal operational failures, which may differ from one shunt to another. The difference between the two categories can be summarised through the fact that all shunts have the fundamental issues discussed below, while operational issues can be associated with some shunts and not others.

a. Fundamental Issues

The first fundamental issue with current shunts is that even after the introduction of programmable valves and anti-siphon devices that helped with over-drainage, no current commercially available valve can definitely reduce the overall shunt failure [57,58]. Furthermore, there is no substantial difference between the early-developed fixed-pressure valves and the programmable valves in terms of revision rate [57]. Pickard et al. [59] further confirm this statement in the case of paediatric patients, but they also show a noticeable advantage for adjustable valves over fixed pressure valves for adult patients. More so, the lack of personalisation of the current shunting system tends to encourage the patient to become fully reliant on the shunt. Although the degree of shunt dependency can differ from one patient to another, it ultimately increases with time [10,11]. This can cause the patient's condition to worsen as the patient becomes less dependent on their body's normal CSF drainage pathways.

An extremely sensitive issue with current shunts is that regardless of the type of shunt malfunctions, shunting systems are not equipped to detect them as these malfunctions “cannot be detected before they manifest clinically” [12]. This can cause health risks to the patient and can sometimes even be life-threatening. Furthermore, the current shunt systems do not take

into consideration the changes in the dynamic behaviour of ICP, which vary not only from one patient to another but also for the same patient depending on age, health, and other elements [10]. Also, the effect of the hydrostatic pressure phenomenon is currently combated with the anti-siphon device mentioned earlier. However, due to the nature of their over-drainage prevention-focused design, there is a potential risk that they may cause under-drainage [13]. Lastly, the fact that current shunts do not recognize the rise in ICP due to normal events can cause unnecessary drainage (over-drainage). These ICP sudden peaks are caused by coughing or sneezing, where the drained CSF can take hours to be re-produced [7].

b. Operational Issues

Current statistics suggest that around 30% to 40% of shunts fail within the first year, 50% within the first two years, and 90% after five years [28,57,60]. According to the 2017 UK shunt report [59], there were around 3000 shunt operations in the UK each year by 2017, 1660 for paediatric patients and 1400 for adults. Around 66.5% of paediatric operations were for shunt revision as opposed to primary first-time installation, while 47% of the adult operations were for shunt revision. The main shunt failures can be summed as follows:

i. Under-drainage (obstruction)

Under-drainage is by far the most common cause of shunt malfunction since 35% to 45% of overall shunt complications result from shunt system blockage [23,59]. Proximal catheter obstruction accounts for around 50% to 60% of shunt failure due to blockage. Valve malfunction due to cells and debris obstruction is only responsible for 5% to 15.8% of shunt failure [57,59].

ii. Infection

The overall reported shunt infection rate varies from 3% to 15% [57,60], with 15% for children under six months and 5% for older children and adults [58]. However,

90% of infection cases occur within the first six months of shunt installation. The probability of infection decreases with time as it reaches 6% after two years [57]. The most recent report by Pickard et al. [59] shows a drop in infection rates since 2009, reporting an infection rate of 5.1% for children and 2.6% for adults. This is assumed to be a result of the increased usage of antibiotic-impregnated catheters since their introduction in 2001.

iii. Mechanical failures

Mechanical failures usually fall within three categories, starting with failures due to fractures, the majority of which occur in the distal catheter. They are responsible for 3% to 12% of shunt failures [57]. The second is failures due to disconnections, which occur when shunt components disconnect from each other due to connector failure. The third is failures due to the migrations of either the proximal catheter or the distal catheter from its initial position. They occur mainly in children as a result of their body development, causing the catheters to be displaced [57,60].

iv. Over-drainage

The main cause of over-drainage in both paediatric and adult patients is what is termed slit ventricles syndrome (SVS), which remains to be a poorly specified condition related to HC-shunted patients. A common theory is that SVS results from the ventricle collapse due to the repeated cycle of enlargement and decompression as a result of the shunt operation cycle. The syndrome usually appears between three and five years after shunt installation [61]. According to Pickard et al. [59], over-drainage is much less common to occur than under-drainage.

2.2.3 Normal Pressure Hydrocephalus (NPH)

Normal-pressure hydrocephalus (NPH) commonly occurs in adults over 60 years old. It is unique as it develops due to the enlargement of the ventricles in the brain (ventriculomegaly) without an increased ICP. As a result, the diagnosis is conducted by tracking associated symptoms instead of tracking ICP. These symptoms are urinary incontinence, cognitive disruption (dementia), and gait disorder. These three symptoms are often termed the Hakim-triad and usually develop slowly over time [62,63]. All three symptoms do not need to be present for clinical diagnosis [64,65], as only 48% of the cases exhibit all three symptoms. The pathogenesis of NPH is still not clear, so patient diagnosis and selection for shunting is difficult. This is more of an issue when it is combined with the fact that only 50% of NPH patients improve after shunting [66]. As the pathogenesis of NPH is still disagreed upon, multiple theories discussing biomechanical, metabolic, hereditary, inflammatory, and vascular factors have been considered and discussed. One study reviewed published knowledge regarding NPH to determine the current consensus regarding its cause [67]. The study reviewed published work between 2007 and 2017 and found that the most frequent theory links high blood pressure, cerebrovascular disease (such as strokes and AD), and poor venous compliance (which impairs CSF pulsation, flow, and absorption through the arachnoid granulations) to the causing of NPH [63,67]. Regardless, this pathogenesis theory is not a certainty, as it is stated that the studies reviewed tend to contradict each other.

The diagnostic process consists of tracking the Hakim-triad symptoms by having patients undergo a physical trial for gait assessment purposes, a mini-mental status examination (MMSE) to assess their cognitive status, and a CT or MRI scan to examine the size of their ventricles. The cognitive disruption consists of decreased volume of speech, slower response time, memory distortion, lack of attention and apathy, and decreased executive functions [64]. As a result, NPH can lead to dementia, which is treatable by addressing the NPH causing it.

The urinary incontinence symptom is a result of detrusor – smooth muscle found in the wall of the bladder – overactivity, which can also cause urinary urgency and frequency [62,63].

The gait disorder is the most common and earliest symptom to surface, as its presence is described as “obligatory” for NPH diagnosis [63]. It seems to be a result of the disturbance of the “phased activation of muscle groups”. This gait disorder is often described with short steps and step height, side-to-side shuffle with the patient bent forward, rotation and pivot difficulties, and an overall reduced speed and slowness of extremities [64,66]. As a result of the importance of gait for the diagnosis of NPH, a study was conducted by Song et al. [68] to identify and quantify patients' gait characteristics. The study considered a large number of factors – before and after drainage – such as velocity, step length, swing, timed course, number of steps to finish the course, and steps to turn 360°. The important outcome of this study was the finding that the 360° turn test proved much less useful when diagnosing NPH. If NPH is suspected after the patient undertakes the diagnostic process, lumbar drainage (LP) is carried out on the patient – usually over the course of three days – to remove between 40 and 50 ml of CSF (high volume LP). This helps in evaluating the patient's response to shunting, where a positive response to the drainage is usually a good indicator that long-term shunting is needed.

As mentioned, the current gait assessment procedure during diagnosis is qualitative. There are three methods to monitor and analyse gaits, starting with machine vision (MV), where optical analysis of motion is used. The second one is floor sensor (FS), where kinematic data are obtained from a sensor-equipped force platform. The third type utilises body-attached sensors, where motion data is collected directly [68,69]. The combination of optical analysis of motion and force platforms is termed gait analysis systems, which can be considered the gold standard for gait measurements [70,71]. However, the space and expenses required by these systems render them impractical as a standard diagnosis practice.

In terms of body-attached sensors, both gyroscopes and accelerometers can be used to obtain gait pattern-related data. A study by Tong and Granat [71] showed that an ankle-mounted gyroscope provided reasonable results compared with the gait analysis systems. One of the studies that objectively assessed patients' gaits used a "GAITRite Portable Walkway and Gait Analysis System", which is a treadmill that analyses and reports walking and gait patterns. The study shows that changes in gait after CSF drainage are highly significant and quantifiable and directly correspond with patients' responses to drainage [72]. Gafurov et al. [73] attempted to use a pair of ankle-attached 2-axis 2 g accelerometers for gait biometric verification. The sensor's sample rate was 16 per second, and the data obtained were deemed "promising". Bamberg et al. [74] carried out one of the most elaborate wireless sensing system studies. They integrated a 3-axis 2g accelerometer, a gyroscope, force-sensitive resistors, bend sensors, and electric field sensors in the bottom layer of a shoe. Bora et al. [75] used a combination of two biometric goniometers and two 3-axis accelerometers in order to measure the gait hip angle, as one of each was placed on both the upper thigh and the hip. Another study was conducted to quantify gait in patients with spinocerebellar ataxia type 6, which is a condition characterised by movement difficulties. It used an accelerometer-based wearable mounted in the lower back [76]. Other studies focused on developing protocols for step characteristics measurement (time and length), but those studies focused on waist and chest-located sensors [77,78].

It is noticed that the use of accelerometers is more frequent than that of gyroscopes. This is a result of the fact that accelerometers have more options when it comes to mounting location and not just joints. Furthermore, a single accelerometer provides data about the entire body's inertia status, which requires two or more gyroscopes to achieve. Lastly, the data obtained by the accelerometer can be translated into angular values, providing the same type of data a gyroscope does.

2.3 Current Research

Current research related to HC shunting falls under two categories. The first consists of research linked to the concept of active shunting. The second consists of research around altering and advancing the valve mechanism of the shunt, as it is the main component for both the classical shunt and the active shunt. Research around active shunting aims to address the fundamental issues with current shunts discussed above, while research around valve mechanism is more concerned with the operational issues of shunting.

2.3.1 The Active Shunt

In the broadest sense, an active shunt can be defined as “an implantable system – including hardware and algorithm – designed to control CSF drainage based on feedback from one or more measured conditions” [40]. The active shunt should autonomously respond to changes in ICP dynamics. It is a “reactive” and “proactive” system that manages and regulates CSF flow based on real-time ICP readings, patient feedback, and prepared schedules. It should also have fault detection and identification capabilities. It should act as a personalised hydrocephalus treatment system for the patient and should be goal-driven to gradually reduce shunt dependency. The shunt's internal part should be able to communicate with the external part to establish a treatment database and report the patient's condition to the physician [9,11].

The components of an active shunt system can be divided into hardware and algorithms [40]. The internal hardware of an active shunt can consist of sensors, a CSF control mechanism, a power source, a communication unit, and housing. In terms of sensors, ICP and CSF have very low values of around 10 mmHg and 0.3 ml/min, respectively. These low values are at the limit of what the existing sensor technology can measure [4,37,79]. Issues such as power draw, seclusion from moisture, and bio-compatibility remain [79]. There are two options for the CSF control mechanism required to manage and drain CSF, which are miniaturised pumps and on-

off valves. A valve or pump design that keeps power consumption to a minimum is necessary as it is an implanted part of the system. Also, the use of materials that resist fouling is highly favourable. An actuator is needed to generate physical movement to control the valve or pump. Essential criteria for this actuator include force output and MRI compatibility (from the magnets on the motor) [10,79]. A power supply is required as different components may operate on battery power, including sensors and actuators on the system. The selection of battery size affects the battery placement inside the body. Another important factor is the type of battery to be used and whether it is rechargeable from an outside source or a battery that requires replacement after a while, such as pacemaker batteries [79]. A communication unit is required for both the data transfer from the implantable shunt to any external database or external devices and the data transfer between different components of the implantable shunts [79]. This includes PCBs (printed circuit boards), ultra-low power microcontrollers (ULP), and wireless transceivers [10,24]. Lastly, housing is needed as the components used in an active shunt require isolation from moisture as they are electronic. In addition to protecting the electric components, the housing must be built from a bio-compatible material to reduce the chances of infections [79].

External hardware – such as smartphones and computers – may consist of any platform to access shunt data [10]. It must be noted that no shunt prototype or detailed design with the above components has been reported in the literature researched. These components describe what the active shunt “should” include. All of the literature surrounding the active shunt is either conceptual or focused on shunting algorithms and control. However, regarding the shunt components, the CSF valve mechanism – showcased in more detail in section 2.3.2 – is one of the main research focuses.

There is less literature shortage when it comes to the algorithm side of the active shunting concept. In general, systems are classified into opened-loop and closed-loop systems. The opened-loop system uses a programmed schedule to control the CSF valve without the need for any sensory feedback, while the closed-loop system uses real-time sensory feedback to control CSF flow [79].

In order for the active shunt to achieve the designated tasks mentioned earlier, the multi-agent approach is proposed for the shunt intelligent system [10,12]. Using the Prometheus methodology to develop this multi-agent system, seven agents – showcased in Figure 2.8 – were developed by Momani et al. [10]. They consist of the “decision-maker, adjustment handler, weaning manager, and the external communicator manager”, representing the external agents. The internal agents consist of the “valve manager, sensors manager, and the internal communicator”.

Later, Alkharabsheh et al. [12] proposed a similar system – showcased in Figure 2.9 – using the same Prometheus methodology. However, their system consisted of six agents, four of which are situated externally consisting of the “decision-maker, feedback manager, database manager, and the external communicator agent”. The remaining two are located internally and are the “ICP report manager and the internal communicator”. The mode of operation for both systems is similar as they should make decisions necessary for valve schedule optimisation based on sensory input. Based on the latest schedule, the systems should also control the valve open/close status and monitor the shunt's performance. Figures 2.8 and 2.9 show the proposed systems layout for Momani et al. [10] and Alkharabsheh et al. [12], respectively.

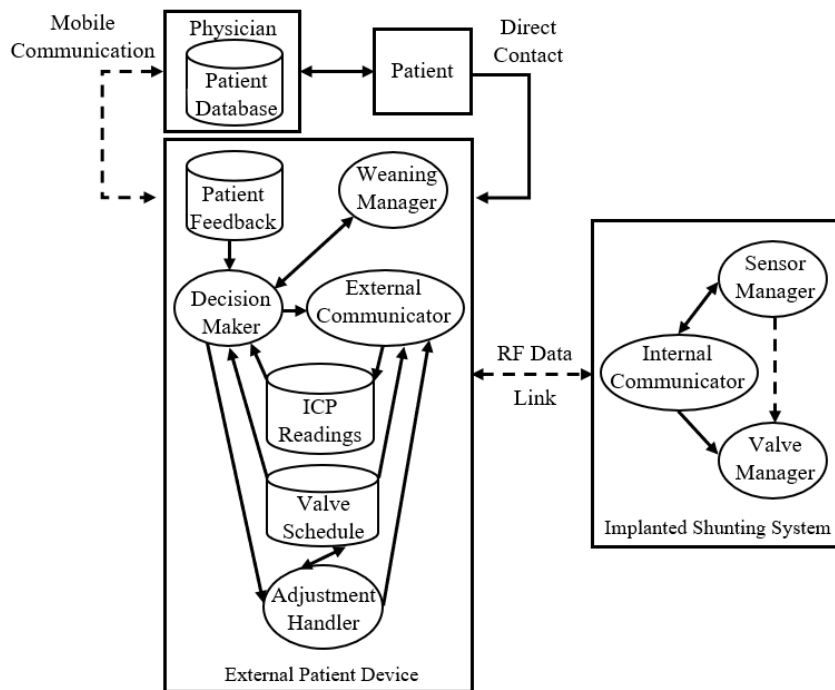


Figure 2.8: Momani et al. [10] proposed system layout

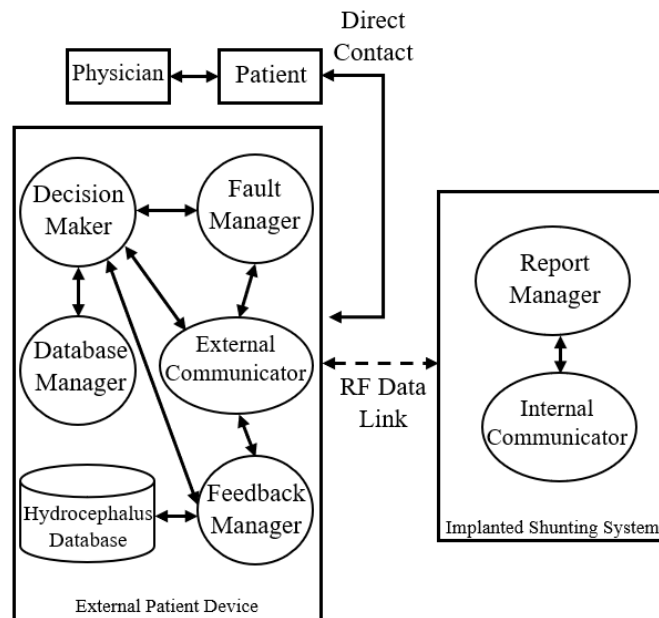


Figure 2.9: Alkharabsheh et al. [12] proposed system layout

Momani et al. [20] proposed a valve schedule structure based on a 24-hour scheme divided into 24 one-hour sub-schedules. The algorithm they developed calculates the optimum on-off period and intervals between these periods for each one-hour sub-schedule. They used three hydrocephalus patients' data since their algorithm required ICP historical readings to personalise the valve schedule for each patient. The algorithm successfully predicted a schedule that maintains the predicted ICP between the acceptable limits. It must be noted that the issue with this type of opened-loop algorithm is its lack of proactiveness and its dependency on historical data rather than real-time data. This type of system remains susceptible to the same fundamental issues mentioned earlier as they do not take into consideration the changing ICP dynamics of the patient, which may cause the historical data the system uses to result in inaccurate drainage. An argument can be made that despite their shortcomings, the currently used passive shunts are more accurate since they use real-time conditions to drain CSF.

Alkharabsheh et al. [21] proposed a fuzzy-logic-based system for fault diagnosis in shunting systems that relies on ICP and flow rate feedback to identify faults. The study was conducted on a schedule-based valve where numerical simulations using Simulink to produce ICP data were performed. The system had an excellent success rate in pointing out the faults in each simulation. They ran 48 trials for different types of faults, including partial valve blockage, full valve blockage, valve disconnection, ICP sensor dislocation, and flow-meter fault. The system was correct in identifying the faults in all trials except for the case of partial blockage and full valve blockage, as they tend to overlap with each other. This study can be considered a guideline when it comes to developing an active shunting fault detection algorithm. The study not only considers ICP and flow-meter sensory input but also the closed/opened status of the valve, which leads to accurate fault-type detection. Although the study was performed on a schedule-based valve, the sensory input it relies on aligns perfectly with a closed-loop valve.

Hence, there is no reason to assume that different results will be obtained for a closed-loop valve.

Another approach to managing active shunts was proposed by Elixmann et al. [22], who extracted craniospinal compliance-related features from the ICP pulse waveform and used them to adjust the target ICP. The appropriate ICP level differs from one patient to another and even differs for the same patient based on a number of elements, such as age and health conditions. The one goal of this algorithm is to decide the ideal ICP value that is suitable for the patient, as it is mainly related to craniospinal compliance. The authors achieved this by using long-term recordings obtained from several hydrocephalus patients, as those readings determined a relationship between the ICP waveform, wave amplitude, and craniospinal compliance. Their algorithm's experimental results show that it is successful in identifying ideal ICP values for different waveforms in real-time scenarios. However, due to the lack of understanding regarding the dynamics of hydrocephalus, the extent of the relationship between compliance, wave amplitude, and waveform is not yet fully confirmed. Furthermore, the authors stated that some factors – such as heartbeat – were not considered, which may or may not affect craniospinal compliance.

Another study was conducted by Narayanaswamy et al. [23], where they developed an algorithm for the precise detection of shunt blockage, identifying not only blockage but also its specific location. The algorithm manages that by analysing feedback from multiple pressure sensors. The minimum number of sensors required for the algorithm to function is four pressure sensors. The first is responsible for measuring ICP, the second measures pressure in the proximal catheter, and the third and fourth are located along the distal catheter. These four sensors allow the algorithm to monitor the proximal catheter, the valve, and the distal catheter for blockage. The more pressure sensors used, the more detailed the blockage location within

these three sites is obtained. The general idea of the algorithm is that when a partial or full flow blockage occurs, the liquid column before the blockage site causes an increase in the pressure. In contrast, the pressure downstream from the blockage will be low due to the limited flow, and by comparing pressure values at each sensor, the blockage site can be found [23]. The study provides a simple yet effective methodology for determining blockage location. The main issue is the required number of sensors for the algorithm to operate, as implementing this number of sensors in an implanted system can be a point of uncertainty. However, using multiple sensors can also be effective in detecting other types of faults, especially since this algorithm can easily be incorporated into general fault detection algorithms such as Alkharabsheh et al. [21].

Momani and Al-kharabsheh [24] proposed a wireless monitoring system to gather ICP data from implantable sensors. They proposed a system with both scheduled and closed-loop operation options. The ICP data is used to update or change the currently used valve schedule or used directly to control the valve – based on ICP reading – when the closed-loop system is activated, as seen in Figure 2.10. Their system allows external intervention to take place when necessary, allowing the physician to control the on-off valve period wirelessly. They also developed an emergency scenario with three emergency levels based on the rise in ICP level. Based on that emergency level, the shunt can either (i) continue working as normal as it sends ICP readings for further analysis in the case of low emergency, (ii) activate the closed-loop scenario in case of medium emergency, or (iii) open or close the valve based on the rise or drift of the ICP in case of high emergency.

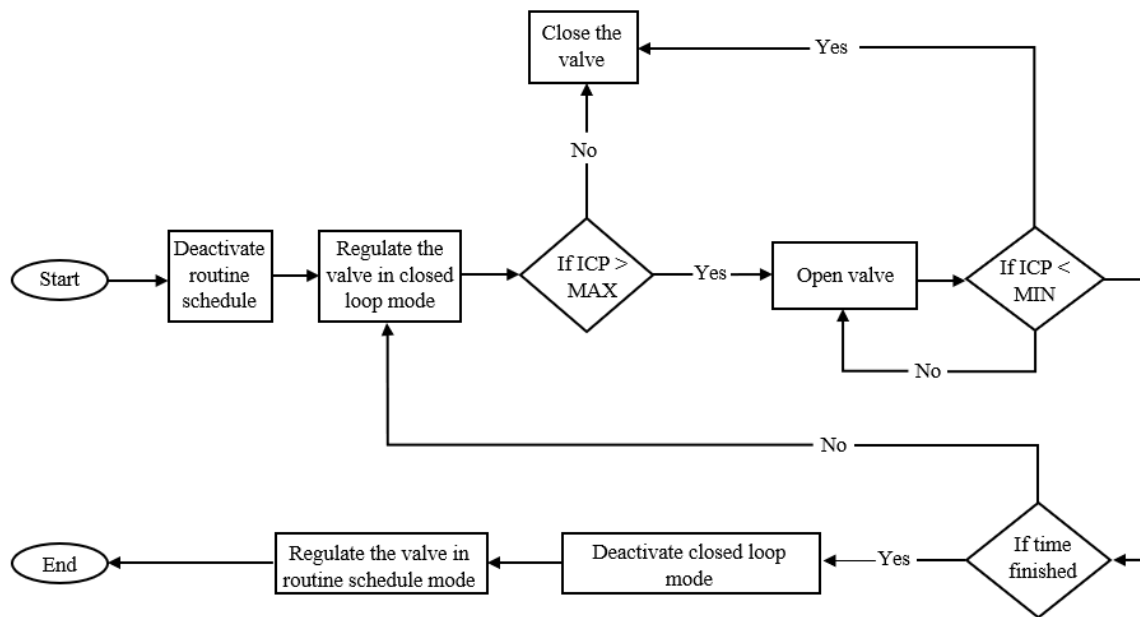


Figure 2.10: Momani and Alkharabsheh [24] closed-loop scenario

The closed-loop system is considered the ideal option when it comes to managing CSF. The combination of a closed and opened-loop system might prove to have some advantages, such as limiting power draw. However, it can be assumed that the opened-loop system will continuously cause the emergency function – due to the inherent lack of proactivity – to be activated, causing the closed-loop scenario to start. This means that the usability of the scheduled scenario during actual operation is in question. Furthermore, the study does not showcase how the closed-loop scenario can combat over-drainage resulting from hydrostatic pressure as it relies only on a single input, the ICP readings. The attractive point of this study is the introduction of a multi-level emergency function with multiple responses.

These studies are summarised in Table 2.1 below, highlighting the specific topic, methods, limitations, and other comments.

Table 2.1: Summary of current research regarding the topic of active shunting

Study	Specific topic	Method	Comments	Limitation
Momani et al. [10] (2008)	multi-agent active shunting system	Prometheus methodology	<ul style="list-style-type: none"> - Total of seven agents. - Provided a weaning manager to reduce shunt dependency. 	Discussion about implementation in real-life scenarios in terms of the hardware required is limited.
Alkharabsheh et al. [12] (2010)	multi-agent active shunting system	Prometheus methodology	Total of six agents.	Discussion about implementation in real-life scenarios in terms of the hardware required is limited.
Momani et al. [20] (2009)	Opened-loop drainage algorithm	Numerical modelling	<ul style="list-style-type: none"> - Introduced a 24-hour valve schedule. - Based solely on patients' historical data. - Lacks proactivity. 	The simulation was conducted on a normal ICP signal with no events taking place, such as patient movement.
Alkharabsheh et al. [21] (2013)	Fault detection algorithm	Numerical modelling	<ul style="list-style-type: none"> - Able to detect five faults. - Excellent success rate 	How the algorithm translates sudden ICP spikes and the effect of hydrostatic pressure on it was not discussed.
Elixmann et al. [22] (2014)	Ideal ICP recognition	Experimental	<ul style="list-style-type: none"> - Used ICP waveform and amplitude. - Successful in real-time scenarios. 	Other factors influencing the ICP wave were not considered.
Narayanaswamy et al. [23] (2015)	Blockage detection algorithm	Numerical modelling	<ul style="list-style-type: none"> - Single fault detection algorithm. - Require a minimum of four pressure sensors. 	The system is very sensitive toward body posture and requires constant calibration.
Momani and Alkharabsheh [24] (2017)	Drainage algorithm	Numerical modelling	<ul style="list-style-type: none"> - The default mode is the opened-loop drainage. - Closed-loop drainage is solely based on ICP and does not consider hydrostatic pressure. - Introduced a multi-level emergency protocol. 	Both the opened-loop drainage and closed-loop drainage do not consider ICP spiking events, which may cause unregulated drainage and an unwarranted emergency scenario.

2.3.2 Advances in The Valve Mechanism

The majority of the literature researched around shunt valves is focused on developing new designs of “passive” valves, as each study proposes a solution to one or several of the operational issues mentioned earlier. Chung et al. [25] developed a valve that utilises the pressure the user generates externally by pushing the housing to resolve the blockage issue. In the pushing stage – Figure 2.11a – the pressure acts on the fluid in the valve cavity and pushes it in both the brain and the abdominal direction. However, the system has a membrane check valve, allowing CSF to flow only in the abdominal direction. Once the user’s fingers are lifted – Figure 2.11b – the restoration of force generates suction from the brain, thus moving CSF into the shunt cavity. The check valve uses a membrane attached to an anchor to regulate flow, as the pressure on the membrane surface causes it to deflect in the flow direction. The deflection ratio combined with the width of the membrane channel controls the valve characteristics. The main purpose of this device is to clear any blockage that may occur in along the shunt – except in the proximal catheter – by inducing a flushing motion of CSF.

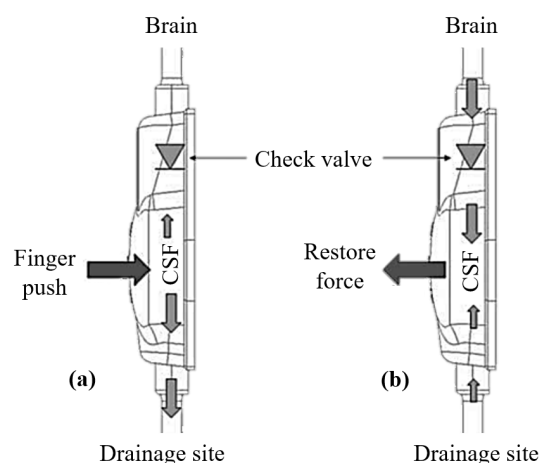


Figure 2.11: Chung et al. [25] shunt design. (a) Finger push creates pressure toward the inlet and outlet of the valve to clear the blockage. (b) Removal of fingers results in suction flow from the brain toward the valve

Johansson et al. [13] proposed an electromechanical system (MEMS) based HC shunt design that can limit the effects of hydrostatic pressure and remove the need for antiphon devices. Their design is solely focused on combating under-drainage that could result from using anti-siphon devices and over-drainage resulting from the hydrostatic pressure effect. Their valve uses a flexible bladder connected to a water-filled third catheter (pressure compensation catheter) – Figure 2.12a – that is parallel to the proximal catheter, causing hydrostatic pressure to affect both catheters simultaneously. A silicon membrane valve – Figure 2.12b – is designed to connect the proximal and pressure compensation catheter to cancel the hydrostatic pressure's effects on the proximal catheter. As the patient stands, the pressure on the inlet port (P_{in}) increases, causing the membrane to open, allowing flow from the inlet port to the outlet port. However, the pressure from the compensation port (P_c) is also applied on the membrane in the opposite direction, negative to the inlet pressure, thus balancing the inlet pressure and causing the flow to be regulated. The area of the valve boss – Figure 2.12b – is much smaller than the area of the membrane, which means that the effective area exposed the inlet pressure (P_{in}) and the compensation port pressure (P_c) is approximately the same.

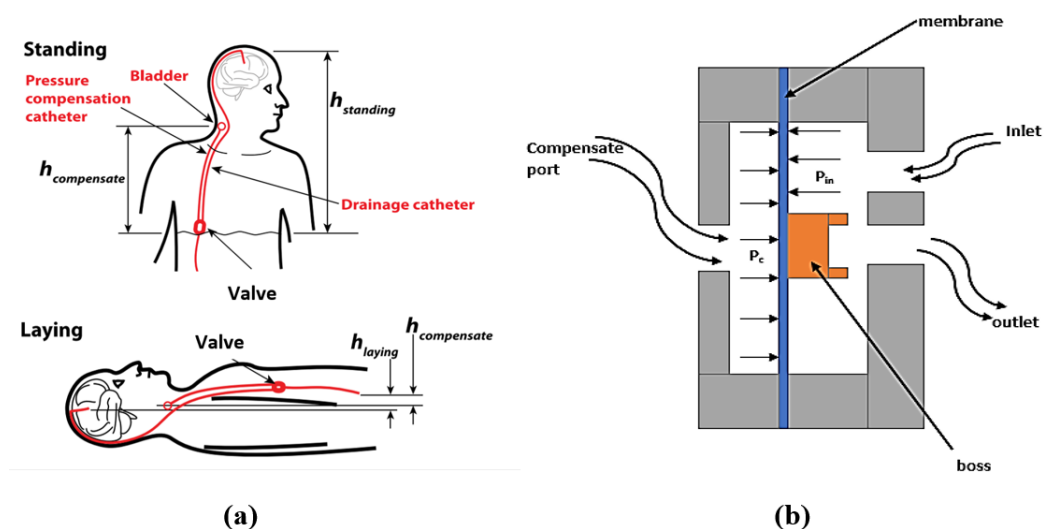


Figure 2.12: Johansson et al. [13] shunt. (a) Layout of the shunt. (b) The membrane valve

Chappel [26] proposed a valve design that is able to offer a continuous and constant CSF flow rate regardless of the ICP level on the valve inlet side. The valve is very similar to the currently used ball-in-cone valves. It has a hollow cylinder housing – Figure 2.13 – with a helically engraved piston, a spring, and two fluid openings. As the pressure reaches the OP – Figure 2.13a – of the valve, the piston slides back, permitting CSF to flow into the inlet chamber. However, flow from the inlet chamber to the valve outlet is limited as the fluid can only stream through the helical grooves on the piston surface. Hence, CSF flow remains constant regardless of the inlet pressure. When the pressure is less than the OP – Figure 2.13b – of the valve, the piston slides to the front, blocking the valve inlet. However, the two small fluid openings in the inlet chamber hold a certain volume of CSF, which means even when the inlet is blocked, CSF will remain streaming along the helical grooves.

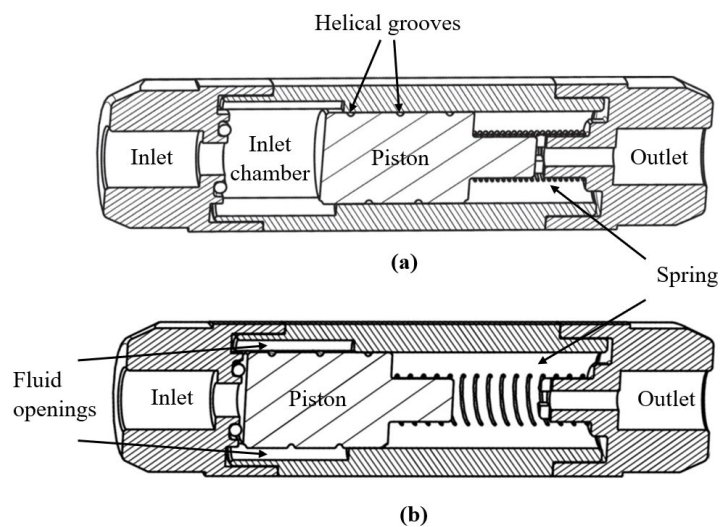


Figure 2.13: Chappel [26] cylindrical valve. (a) Opened Status with CSF flowing into the inlet chamber. (b) closed status with the CSF reserved in the fluid openings flowing into the outlet of the valve

Webster et al. [27] presented a concept to detect valve faults using the visibility of silicon through ultrasound. This was accomplished by designing a valve that utilises a snap-through buckling (STB) shell to control CSF flow. They used the ability of certain materials to buckle or deform under pressure elastically. Fault detection is established through ultrasound imaging of the valve shape as the valve has a certain shape when blocking flow and another shape when it buckles under pressure permitting CSF flow as seen in Figure 2.14. This signifies that the technique does not allow for specific fault or location detection but is used as general fault detection based on whether the valve is operational or not. The valve is designed in a way that when the pressure reaches a certain limit, the spherical STB silicon shell collapses inward exposing a hole – Figure 2.14b – at the centre of the shell that allows CSF to flow. When the pressure drops, the silicon shell rebounds to its original shape closing the hole in the centre. The characteristics of the valve are defined by the shell thickness, radius, and material hardness.

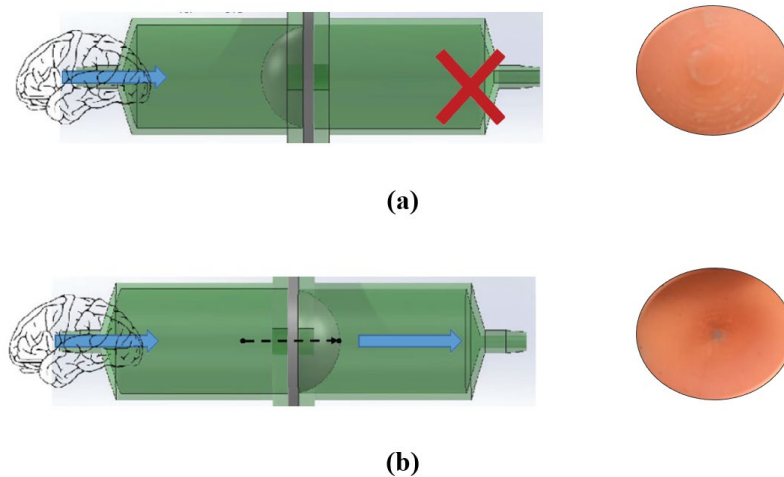


Figure 2.14: Webster et al. [27] shell valve. (a) Closed status of the valve with the shell in its original shape. (b) Opened status of the valve where the shell has buckled under pressure, exposing the hole in its centre and permitting CSF flow

It must be noted how these designs differ highly both in nature and on the issues they attempt to address. Chung et al. [25] offer a manual solution to one of the major faults in shunting, as their design is able to clear debris from the shunt valve and distal catheter. However, due to the fact that it uses a check valve between the shunt and the proximal catheter, the backward flushing flow removal does not occur in the proximal end of the shunt. This becomes an especially relevant issue when considering that 60 % of blockage [59] occurs within the proximal end. It must be noted that the study provided experimental validation of the valve functionality to handle CSF flow. Still, no tests were run to confirm the extent of its ability to remove a blockage. Johansson et al. [13] shunt design offers an alternative method to antisiphon devices to combat over-drainage from hydrostatic pressure. However, the exact advantages of this design over antisiphon valves are not clear since antisiphon devices deliver the same results with a smaller footprint as they are currently attached to the shunt valve. The authors also note that the membrane valve does not act as a check valve successfully, as it cannot stop reverse flow. Another aspect that needs to be pointed out is that the shunt valve must be implanted in the body's midsection, and whether that is convenient both surgically and for the patient remains to be investigated.

Regarding Chappel [26], the valve design nature is excellent in combating hydrostatic pressure effects and ICP spikes caused by coughing or sneezing events. The fact that the valve delivers constant CSF flow regardless of ICP status is both an advantage and a disadvantage. While the valve mitigates the effects of hydrostatic pressure and ICP spikes causing events, it does not allow for more drainage to occur when required due to an increase in ICP. Webster et al. [27] stated that specific dimensions of the shell valve might result in CSF leakage when the valve is in closed status. They also state that when the valve rebounds as it transitions from the opened to the closed status, some reverse flow of CSF tends to occur.

The natural CSF drainage process consists of it being absorbed from the brain to the sagittal sinus, which in turn carries CSF out of the cranium. This drainage process is controlled by what is termed arachnoid granulations (AGs), which are small protrusions growing from the arachnoid matter surface – Figure 2.15a – that act as a natural slit valve with specific pressure settings to control CSF flow out of the brain [80]. As HC can occur when these AGs are blocked, one of the most interesting current trends consists of designing miniature valves that are implanted on the arachnoid matter surface – Figure 2.15b – to replace these blocked AGs.

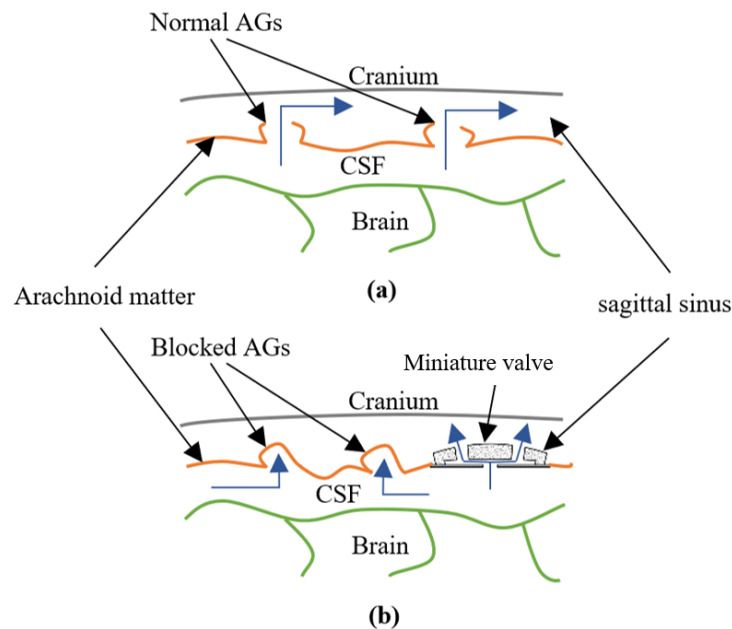


Figure 2.15: CSF drainage through the sagittal sinus. (a) Natural drainage through the arachnoid granulations (AGs). (b) Drainage through the miniature valve when the AGs are blocked

Oh et al. [28] produced one of the earliest studies regarding miniature valves using silicon-based polydimethylsiloxane (PDMS) and parylene in a simple 3-D dome petal shape shown in Figure 2.16a. They designed two valves, a cross-cut, and a slit-cut dome (single cut). The principle of the valve operation is based on the pressure over and under the dome so that when

the pressure difference reaches the designed opening pressure, CSF is permitted to flow. The dome's cut length, diameter, and height control the valve characteristics. Another similar valve that is also placed on the arachnoid mater to mimic the operation of AGs was presented by Schwerdt et al. [29], where they replaced the blocked AGs by using a passive hydrogel valve. The valve is composed of biocompatible hydrogel and silicon, as showcased in Figure 2.16b. While the silicon acts as the base of the valve, the hydrogel performs as a membrane that deflects to allow the flow of CSF when a specific pressure difference is reached. Another type of these valves was also proposed by Lee et al. [30], as they produced a 3-D printed hydrogel check valve shown in Figure 2.16c. The hydrogel has a slit-shaped channel to allow for uni-directional flow and tends to absorb fluids and get swollen as a result. The swelling increases the hydrogel's mass, causing the structure's two sides to be further pressed against each other. This, combined with the slit-shaped channel, defines the characteristics of the valve in terms of pressure settings. The valve acts under the same principles as the above miniature valves, relying on pressure difference to permit CSF flow. One of the latest studies was conducted by Lylyk et al. [32], as they proposed another miniature valve consisting of a 3 cm tube – Figure 2.16d – with a built-in slit valve to manage CSF flow. The main difference between this design and other miniature valves is the location of where it is implanted and the route used for CSF drainage. The tube is not implanted across the arachnoid mater (upper side of the brain) but rather through the internal jugular vein and deployed at the inferior petrosal sinus (IPS) (bottom side of the brain). The tube has a mascot catheter end to help stabilise it once it is deployed across the IPS.

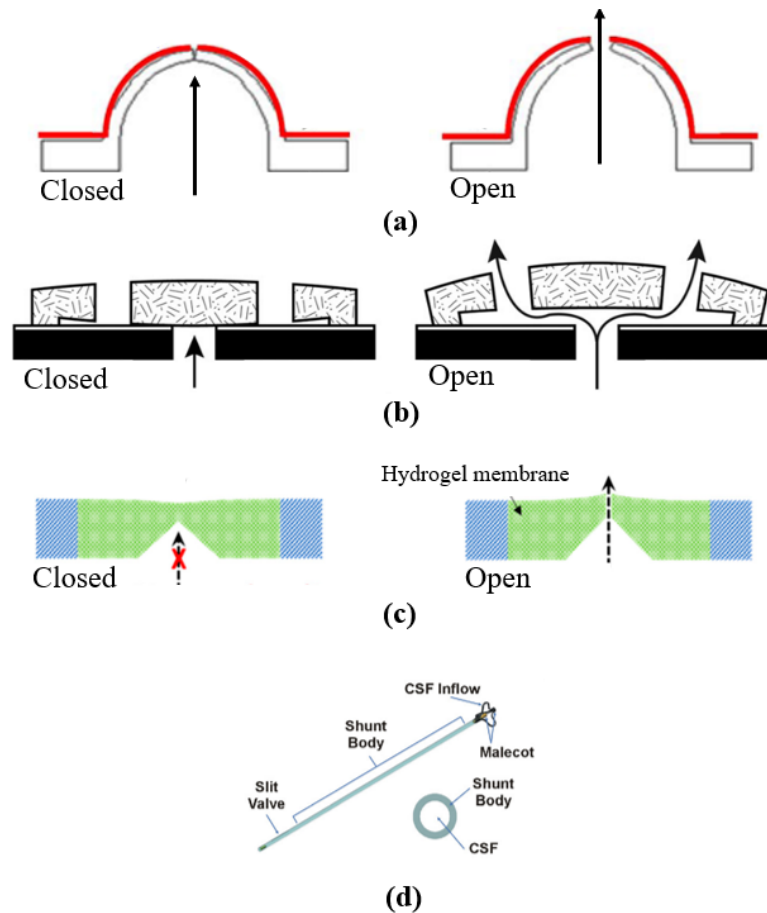


Figure 2.16: Passive miniature valves in current research. Arrows indicate CSF flow direction. (a) Oh et al. [28] 3-D dome PDMS-based valve. (b) Schwerdt et al. [29] hydrogel valve. (c) Lee et al. [30] hydrogel valve. (d) Lylyk et al. [32] inferior petrosal sinus (IPS) valve

These miniature valves present a promising new option to replace the current classical shunts as they eliminate some of the challenges these current devices face. Unlike current shunts that use proximal catheters tunnelled inside the brain, these valves greatly reduce the risk of infections as the valves are implanted outside the brain. Furthermore, the lack of catheters in these designs eliminates the potential for some mechanical failures, such as disconnections or catheter migration (catheter displacement). Also, because of the valves' nature and placement, they eliminate the issue of over-drainage due to hydrostatic pressure (siphoning effect). However, these designs have some drawbacks and uncertainties, such as a higher probability

of blockage and obstruction due to their microscopic size. The manufacturing process for the Oh et al. [28] valve can be considered complicated compared with current devices, as it includes SU-8 mould fabrication, PDMS and parylene coating on that mould, and laser machining the dome slits. Furthermore, they stated that the valve failed to prevent reverse flow due to its geometrical shape and the non-sticky nature of parylene. Also, Schwerdt et al. [29] note that further issues surrounding their valve include the susceptibility of the hydrogel to absorb CSF, which alters its deflection properties. Also, due to its size and the fabrication process, the reproducibility and reliability of the valve are points of consideration. The hydrogel's tendency to absorb fluids was incorporated into Lee et al. [30] design, which managed to eliminate it as an issue and use it as a feature to prevent reverse flow, as proven by their experimental study [31]. The main issue with this valve is its reproducibility, as 140 valves were manufactured, but only 27% of them met the required specifications [30]. This is a result of the attempt to correlate the hydrogel swelling with the valve pressure specification and the valve's ability to not permit reverse flow.

The most note-worthy issue with these types of valves is the fact that since they are implanted on the arachnoid matter – or the inferior petrosal sinus (IPS) in the case of Lylyk et al. [32] valve – they can only be used to manage communicative HC where CSF is able to exit the ventricular system as opposed to non-communicative HC where CSF is trapped in that system. This is the main reason why the proximal catheter is always implanted inside the ventricular system in the current shunting systems.

A summary of these studies is showcased in Table 2.2 below, where the study focus, valve nature, specifications, and other comments are highlighted.

Table 2.2: Summary of current research on valve mechanism

Study	Focus of study	Specifications	Comments	Limitations
Chung et al. [25] (2003)	Blockage removal	- Elastic housing. - Membrane valve.	silicon check - It is the same as the classical shunts pathway. - Flexible housing is used to induce a flushing motion.	The potential effects of the unregulated flow on both the proximal and distal ends as a result of flushing are not discussed.
Johansson et al. [13] (2014)	Combating the siphoning effect	- Compensation Catheter and bladder. - Membrane valved	- The valve is located in the midsection of the body.	The feasibility of multiple catheter implantation in addition to a pressure-sensitive valve in the body's midsection needs to be confirmed.
Chappel [26] (2016)	Continuous constant CSF flow	- Threaded Piston. - Spring setup.	- Same as the current classical shunts. - Can combat over-drainage from hydrostatic pressure and ICP spikes causing events.	The valve's susceptibility to cause under-drainage due to its operation nature is not discussed.
Webster et al. [27] (2018)	Fault detection	- Silicon-based STB shell.	- Same as the classical shunts pathway. - Valve status is visible through ultrasound.	The device relies on elastic deformation, but no discussion about the device's elastic limits is provided.
Oh et al. [28] (2011)	Miniature brain Implant	- PDMS and parylene deflection membrane. - PDMS-base. - 3-D dome shape.	- Implanted on the arachnoid mater. - Reverse flow issues. - Resolve a number of operational issues.	The exact method of implanting the valve on the arachnoid mater requires discussion.
Schwerdt et al. [29] (2014)	Miniature brain Implant	- Hydrogel deflection membrane. - Silicon base.	- Implanted on the arachnoid mater. - Reproducibility and reliability issues.	Implementation methods on the arachnoid matter require discussion.
Lee et al. [30] & [31] (2020) & (2022)	Miniature brain Implant	- Hydrogel deflection membrane. - Silicon base.	- Implanted on the arachnoid mater. - Resolves a number of operational issues.	Implementation methods on the arachnoid matter require discussion.
Lylyk et al. [32] (2022)	Miniature brain Implant	- Macro tube. - Slit valve based.	- Implanted on the inferior petrosal sinus (IPS). - Resolves a number of operational issues.	Implementation through the IPS is complicated due to nearby veins and arteries.

All of the designs mentioned above are passive single fixed pressure point valves that act as fixed differential pressure valves with only one pressure setting, as they do not offer the option to change the valve opening pressure. Based on the literature, it is noted that research is shifting focus on using membrane valves that are directly implanted around the brain tissues as opposed to traditional shunting techniques. This is understandable as these valves offer the opportunity to eliminate several major inconveniences with the current shunting system. However, they also have several issues, ranging from reproducibility to blockage issues. Although these new designs attempt to eliminate one or several operational issues that surround current shunts, they remain exposed to the same fundamental issues ranging from lack of proactivity to lack of fault detection features.

None of the researched literature attempted to design an electromechanical valve that can be compatible with the active shunt concept, as current options cannot change the opening pressure automatically (electromechanical valves). There is an extreme necessity for such a valve right now as the scientific community's focus is shifting – in addition to miniature valves – toward an active shunt system that is controlled by algorithms. Further innovation cannot take place without having a viable prototype that can test current theories and concepts related to active shunting. Nevertheless, there are multiple patented designs of CSF management valves that are targeted to be used on active shunts. Miethke [35] describes an electromechanical valve – Figure 2.17 – that is adjusted using an automated actuating system guided by an electronic system to close and open the valve. At the same time, a pump-based active system was also proposed by Bertrand et al. [81] to control the flow of CSF. Another patent registered to Ludin and Mauge [36] describes a mechanical valve, a pressure sensor, and an actuator that can be controlled using an algorithm. These patents remain in the conception stage as no prototype or detailed design is available in the literature reviewed. Components are

described generally in these patents as the exact methods of actuation and sensor operation are not detailed.

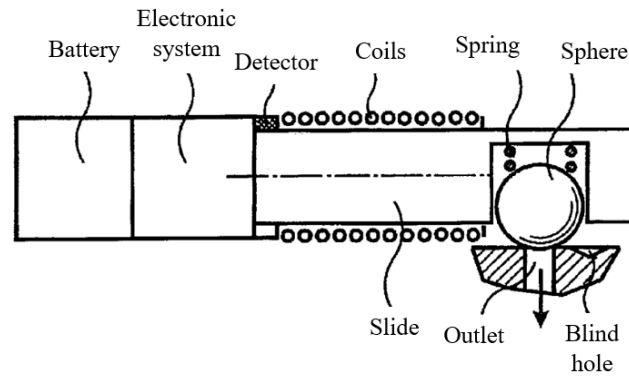


Figure 2.17: Miethke [35] patented valve design

2.4 Conclusions

It can be seen that the literature surrounding CSF shunting is not extensive, as most of the literature is focused on the clinical progress of the disease. When it comes to studies regarding the advancement of shunts, some studies provided new designs that follow the same current shunt layout in an attempt to address certain issues with the current system. However, the classical shunt layout is being deserted as there is a trend of using miniature valves that can be implanted near the brain as they can eliminate several of the operational issues facing current shunts.

Although the notion of active shunting is not a new concept, attention to research and innovation around the topic has been lacking. This is made clear through the fact that the biggest leap in the field was the introduction of the currently used adjustable shunt, which was developed in the 1980s. Most of the research regarding active shunting is on the conceptual level and is focused on algorithms. This is mainly a result of the small market of HC shunts

compared with other neurosurgical devices [33]. This can be clearly seen in the case of ICP sensors, as great attention has been given to them. This is because ICP monitoring is necessary for head trauma, intracranial haemorrhage, subarachnoid haemorrhage from ruptured brain aneurysms, and intracranial tumours and is not only of importance for hydrocephalus patients. Another factor to the lack of research around the topic of active shunting could be the actuating method, as it is traditionally achieved using magnetic manners and the implantability, miniaturising, tolerance, precision, and the effects of such method – magnetic fields – on patients is a point of question [34]. The most recent actuating method is using piezoelectric elements, which is a better fit for this type of operation. The main problem with piezo motors is their high voltage demand. However, this is no longer an issue as a result of the introduction of ultrasonic piezo elements. Some of the few teams currently addressing active shunting are Ellis Meng and Tuan Hoang from the University of Southern California. They created a prototype pressure and flow sensor incorporated with the shunt for malfunctions detection [82]. This further asserts that the gap in research is the development of a valve that can be electronically controlled, which is one of the main contributions of this study. The proposed valve is intended for use in an active shunt that can address the fundamental issues with current systems.

Chapter 3

ACTIVE SHUNT CONCEPT

3.1 Introduction

Any device introduced to the human body through medical or surgical means and designed to remain there after the procedure is considered an implantable device [83]. The first implantable medical device was a pacemaker developed in 1958. Currently, 5-6% of the developed world population has a medical implant helping with a specific bodily function [84]. The methodology followed through the conceptualisation process of the shunting system is based on three factors. First are the demands and requirements of the patients, which are the main factors that affect the nature of the implanted system. The second factor is the medical staff and physicians' preferences, requirements, and feedback. Lastly, the feasibility of the implant is examined from an engineering perspective. It is important to note that the active shunting system concept proposed in this chapter is drafted from a hardware perspective as opposed to the currently available ones based on algorithms and software.

In regard to patients' demands, the active shunting system must be able to address all the fundamental issues mentioned earlier in section 2.2.2. Hence, the system must offer personalised treatment, be able to detect ICP spikes due to events, detect faults within the system, and combat over-drainage resulting from the siphoning effect. This requires controllable drainage, data handling, and communication. This chapter is where system

components that are needed to achieve these requirements are identified. The system layout and how these components link to each other are also discussed.

3.2 Main System Components

The components required for the system to operate rely on the failures that the system must address, as each component must be goal-driven to address one or more specific fundamental issues of the current passive shunts. A list of these failures and the proposed solutions to approach them is showcased in Table 3.1. These solutions are translated into components that the active shunting system can utilise to negate the showcased failures.

Table 3.1: Solutions to passive shunting failures and required components

Fundamental issue	Solution	Required Components
Increased shunt reliance	Drainage must be based on a real-time weaning algorithm and sensory input.	- Drainage algorithm. - Control unit. - ICP sensor
Lack of malfunction detection	Real-time ICP abnormalities analysis is required.	- Fault detection algorithm. - Control unit. - ICP sensor.
Vulnerability to Changes in ICP dynamics	Drainage control must be based on real-time ICP data.	- Controllable valve. - ICP sensor
Over-drainage due to the siphoning effect	Monitoring patient movements and adjusting drainage accordingly.	- Controllable valve. - Body position sensor.
No ICP spikes recognition	Recognition of ICP spikes causing events.	- Body position sensor.

As shown in Table 3.1, the system consists of multiple components that are divided into hardware and software. In terms of the hardware side, the components include a pressure-sensing unit that is necessary to track the ICP level as it is the main sensory output. It also includes a body position sensing unit that is required to combat the effects of hydrostatic pressure (siphoning effect). The body position sensor also assists with identifying ICP spikes due to coughing or sneezing to prevent over-drainage. A control unit is required to provide the communication tools by which different components are able to communicate with each other. It is also the platform within which the algorithms – both drainage control and fault detection algorithms – managing the shunting process are installed. A controllable valve is required to drain CSF out of the brain, as its OP must be controllable electronically in order to achieve the solutions listed in Table 3.1. Lastly, a power source is needed as all of the above components require power to operate. These components are shown in Figure 3.1.

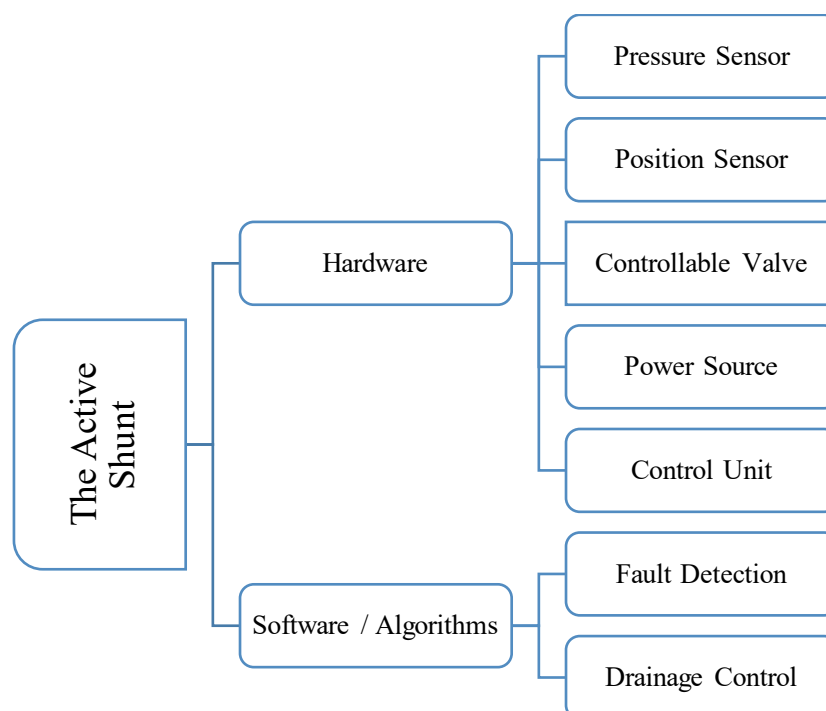


Figure 3.1: Active shunt components

The next sub-sections attempt to discuss in detail the current options for all of these hardware components, whether these options are commercially available or currently being researched. This is carried out in order to also identify the component that is most critical to the development of an active shunt, where establishing progress in terms of this component is most necessary.

3.2.1 Pressure Sensing Unit

ICP monitoring is of extreme importance for hydrocephalus patients as diagnosis, patient status, and condition progress rely on ICP levels. Furthermore, ICP is the main input when it comes to the active shunt system, as drainage decisions are made based on it. In general, ICP monitoring methods can be categorised into non-invasive and invasive methods. Non-invasive measurements are of low risk as they do not require the insertion of a device into the patient's body. Some of these non-invasive techniques to estimate ICP include the use of magnetic resonance imaging (MRI) by measuring transcranial blood and CSF volume flow rate, the use of transcranial doppler ultrasonography (TCD) in conducting measurements of the ophthalmic artery, and the use of near-infrared spectroscopy (NIRS) by measuring tissue oxygenation [85–88]. The other widely used method is invasively gathering ICP readings through micro-pressure sensors. These sensors are divided into two main categories based on their working principles, consisting of fibre-optic and piezoelectric (piezo) sensors. Fibre-optic sensors use the change in the intensity of the light reflected from a built-in mirror as a result of pressure and translate that change into pressure readings [89,90]. Drift proved to be a major issue with this type of sensor as it can exhibit a zero-drift greater than 3 mmHg, resulting in an overestimation of ICP by (9-30) mmHg [91]. The piezoelectric sensors utilise a silicon membrane that is infused with piezo-resistors-based transducers, where pressure readings are obtained based on the deflection of the silicon membrane [85,92,93]. These sensors are much more popular than the fibre-optic

ones as they are used in most commercial ICP sensors, such as Codman ICP micro-sensors, Raumedic Neuro sensors, and Sophysa Pressio 2 sensors. The sensor proved robust and reliable and produced minimal zero drift [93].

Pressure monitoring can be achieved by placing the sensor – showcased in Figure 3.2 – in different locations, such as the parenchyma, subarachnoid space, epidural, and ventricles. In the case of the ventricles sensing packages, both ICP monitoring and CSF drainage are achievable using the same catheter. This is an important distinction between ventricles ICP monitoring and other locations, as drainage is only possible from the ventricles.

The most recent ICP sensing system to be developed is the “Telemetric” ICP sensors like the Miethke Sensor Reservoir and the Raumedic Neurovent-P-tel sensors. They utilise the piezo-resistive method to measure pressure but differ in how they receive power and deliver ICP readings as they are wireless devices [94,95]. The appeal of such a system is its lack of external wires and the level of mobility it can offer. However, although some tests and clinical studies regarding these devices' accuracy and zero drift have been carried out [94,95], they remain a new and unproven technology with limited data on their functionality on a broad ICP range.

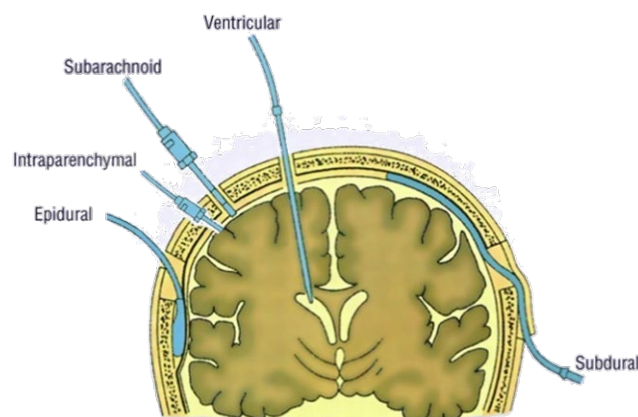


Figure 3.2: Different locations for sensor implantation for ICP monitoring [96]

It is important to note that the gold standard (most accurate) method by which ICP is measured and monitored is external ventricular drainage (EVD), where a catheter is placed in the ventricular compartment through a burr hole for both drainage and pressure measurement through an external pressure sensor. The greatest shortcoming of the non-invasive techniques mentioned above is that none of them is accurate enough to be used critically or as a main ICP monitoring system [97]. Furthermore, under the scope of the active shunt concept, such systems are not practical as they lack mobility and require complicated devices. Telemetric devices offer excellent mobility and are very suitable for on-demand ICP measurement. Still, they do not provide drainage – except for the Miethke Sensor Reservoir – which could prove inconvenient for continuous ICP monitoring.

The logical choice is the ventricular catheter tip implanted piezo micro pressure sensor where both CSF drainage and ICP monitoring can be achieved. The piezo micro pressure sensor closely follows the gold standard measurement of EVD and can provide both ICP monitoring and CSF drainage simultaneously. They are in good agreement with the concept of the active shunt.

3.2.2 Body Position Sensing Unit

As mentioned earlier, hydrostatic pressure is one of the issues that face HC shunting in general as it causes over-drainage to occur when the patient changes their body position from supine to standing. This showcases the importance of tracking the patient's position for controlled drainage, which can be achieved by incorporating an accelerometer or a gyroscope into the active shunt system. The sensor is also necessary for identifying coughing and sneezing events that cause over-drainage as a result of the sudden spikes in ICP.

Gyroscopes are devices that can detect changes in angular rotation velocity, and they consist of micro-electromechanical (MEMS) and optical gyroscopes. Optical gyroscopes measure

rotation in a single given axis, while the MEMS ones can support up to 3-axis feedback and are perfect for miniaturization [98–100]. Although the optical gyroscopes are very accurate, they are complex and expensive to manufacture. MEMS gyroscopes are robust, can be manufactured to the required performance and accuracy, and can provide measurements for up to three planes. As a result, they are currently in control of the market [101].

The second option is using accelerometers, which are sensors that can detect changes in linear velocity for one or more axes by measuring the displacement of a proof mass attached to a spring system. The main types of accelerometers include capacitive, piezoelectric, and piezoresistive accelerometers. The capacitive accelerometers have low power consumption, low noise, and fast response to motion, while the piezoelectric ones are not suited for constant operation [102,103]. The Piezoresistive accelerometers are good for constant operation, such as measuring gravity [104].

The gyroscope seems to be the most appropriate device to use at first, as combating hydrostatic pressure is linked to gravity and the angle of the patient's body position. However, a 3-axis accelerometer can also detect orientation using acceleration data. Furthermore, some studies showcased that the accelerometer output is more appropriate for the detection of sneezing and coughing events [105,106], as these events cause ICP spikes and result in over-drainage. Thus, it can be concluded that the more appropriate sensor to use is a 3-axis piezoresistive accelerometer due to its output, constant operation ability, accuracy, and miniaturisation. This can replace the currently used antisiphon devices built to combat over-drainage in classical shunts.

3.2.3 Controllable Valve

The controllable valve status is the output resulting from the decision-making process in a controlled closed-loop system. From a hardware point of view, the controllable valve

characteristics, mechanism, and design determine the requirements of the other components. The control unit layout and the implant power requirements (the battery) depend highly on the valve mechanism and its operating voltage. The controllable valve consists of two components, which are the CSF flow diversion mechanism and the actuation mechanism. More details on the valve mechanism and design are discussed later in chapters four and five.

3.2.4 Power Source

Batteries are used in implanted biomedical devices ranging from pacemakers and implanted cardiac defibrillators to neurostimulators and drug delivery systems. The battery for the active shunt is necessary to provide power to the different components of the system. It must be highly reliable with a stable and safe constant output level. Also, it must provide power over a prolonged period of time to keep surgical interference to a minimum. Furthermore, the battery energy-to-density ratio must be high to enable miniaturization so it can be suitable for an implant. Table 3.2 presents multiple types of batteries currently used in biomedical implanted systems.

Table 3.2: Different types of implanted batteries

Battery type	Cell potential (volt)	comments
Lithium/Iodine battery Li/I ₂	2.8	<ul style="list-style-type: none"> - widely used for pacemakers. - High energy-to-density ratio. - Safe and reliable.
Lithium/Manganese Dioxide Battery Li/MnO ₂	3	<ul style="list-style-type: none"> - High cell potential. - High energy-to-density ratio. - Stable output characteristics.
Lithium/ Carbon Monofluoride battery Li/CF _x	3	<ul style="list-style-type: none"> - High cell potential. - Very high energy-to-density ratio. - Lower capacity. - It can maintain charge better in standby mode (low self-charge).
Lithium/ Carbon Monofluoride-silver vanadium oxide battery Li/CF _x - SVO	3.2	<ul style="list-style-type: none"> - It has the same properties as the Li/CF_x batteries in addition to improved energy-to-density ratio and higher cell potential.
Carbonaceous/Lithium cobalt oxide battery C/LiCoO ₂	3.9	<ul style="list-style-type: none"> - Highest cell potential. - Capable of delivering high current levels.

Information obtained from [107,108]

The power needs of the accelerometer, ICP pressure sensor, and electromechanical valve influence the power requirement for the active shunt. Pressure and acceleration piezoresistive sensors tend to operate at a 2.8 – 4 V range. The electromechanical valve specifications – discussed in chapters four and five – require a 3.5 V supply input. This leads to selecting the C/LiCoO₂ rechargeable battery as it has the cell potential required for these components to operate. The C/LiCoO₂ has a carbonaceous anode and a lithium cobalt oxide cathode. Materials such as manganese, nickel, and cobalt-based oxides can be used for the cathode electrodes. However, lithium cobalt is widely used as it has a higher gravimetric capacity of 155 mAh/g. This cell type was developed for specific use in implanted biomedical devices [107].

3.2.5 Control Unit

The control unit is the platform for the hardware needed to operate the different components of the active shunt. The most important piece of hardware on the control unit is the microcontroller (or processor), as it is the brain of the operation and the platform for the algorithms used for CSF drainage and fault detection. The hardware can include up to two voltage regulators to ensure accurate performance of both the pressure sensor and the accelerometer since they require specific voltage input. Analogue-to-digital signal converters are also required as both the pressure and the acceleration sensor outputs are analogue and need to be converted before they are supplied to the microcontroller. On the other hand, a digital-to-analogue converter is also required to convert the digital signal from the microcontroller into an analogue signal to control the actuation mechanism of the electromechanical valve.

Furthermore, another extremely important piece of hardware is the bluetooth transceiver that is needed for the implanted system to share sensory data and system status with external monitoring platforms. It is also how the valve operating pressure can be changed after implantation and during operation. These components are grouped and connected together through a printed circuit board (PCB), which must be a high-density board that allows for the packing of many connections in a small area due to size restrictions.

3.2.6 Algorithm

The algorithm used to control the shunt is divided into the drainage control algorithm and the fault detection algorithm. The drainage algorithm controls the valve opening pressure by using the ICP pressure sensor and accelerometer feedback. It controls drainage levels when the hydrostatic pressure is in effect and when it is not. It also detects events of coughing and sneezing – based on accelerometer readings – to prevent over-drainage due to ICP spikes. On the other hand, the fault detection algorithm detects issues with the valve mechanism and the

system in general, as it is able to detect blockage and other issues within the shunt system using sensory feedback. This, combined with patient feedback, can assist in detecting faults and their types. The algorithm offers the possibility of personalising drainage requirements for each patient individually. As reviewed in section 2.3.1 and shown by Momani et al. [10] and Alkharabsheh et al. [12], fuzzy logic algorithms can be used to establish control over the components of such a system. This includes a weaning scenario where patients are gradually pushed to use the normal CSF drainage pathways instead of the shunt system. This is of extreme importance as it can potentially transfer the active shunting system into a treatment option instead of a management system.

3.3 System Layout

The hardware components are identified in the previous section and are showcased in Figure 3.3. The pressure sensor is tip-mounted and installed on the proximal catheter in the cranial cavity inside the brain. The electromechanical valve remains in the same position as the current mechanical shunt, which is under the skin and just behind the ear. The control unit, accelerometer, and battery are grouped together in the same package, making the system more compact. There are two options when it comes to the implant location of this package. The first one is the chest cavity since it provides plenty of space for the package, while the second option is to implant it below the valve near the head of the patient. It is important to note that the performance of the bluetooth transceiver across the body needs to be considered. This is because of the dielectric properties of muscle, fat, and skin. Human tissues show an increase in relative permittivity as frequencies decrease. However, studies show that communication is feasible with active implants with a transmission loss of 20 to 60 dB at frequencies between 100 MHz and 1 GHz [109–111]. Both the chest area and the location behind the ear are low-fat areas, making them appropriate for a stable bluetooth connection.

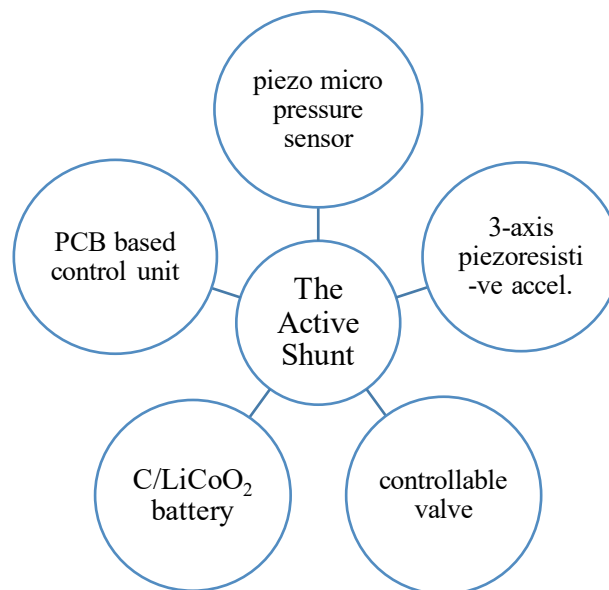


Figure 3.3: Implanted hardware components of the active shunt

However, locating the control unit package behind the ear introduces an opportunity to charge the system battery using conductive coupling – similar to the Neurovent-P-tel sensor and Miethke Sensor reservoir – since only skin stands between the battery and the charging mechanism. This is even more appropriate as the selected C/LiCoO₂ battery is rechargeable. However, this location can constrain the size of the control unit package as it is required to be as small as possible since it shares this location with the controllable valve. Furthermore, there is minimum tissue volume in that area, ensuring that bluetooth stability is at a maximum. The deciding factor is that this option ensures that both the controllable valve and the control unit are implanted in the same location, improving compactness and reducing the number of surgical locations needed. Thus, for these reasons, it can be concluded that the second option is considered the more appropriate layout for this system.

The control unit connects to a mobile phone using bluetooth for data storage and patient feedback. The data collected by the sensors are stored locally on the mobile phone. It is sent through the Internet to a secure hospital database, where it is made available to the physician. The pressure sensor and valve are implanted and connected to the control unit using cables. The physician is able to set the needed opening pressure for the valve remotely. Figure 3.4 shows how the data is handled in the proposed system.

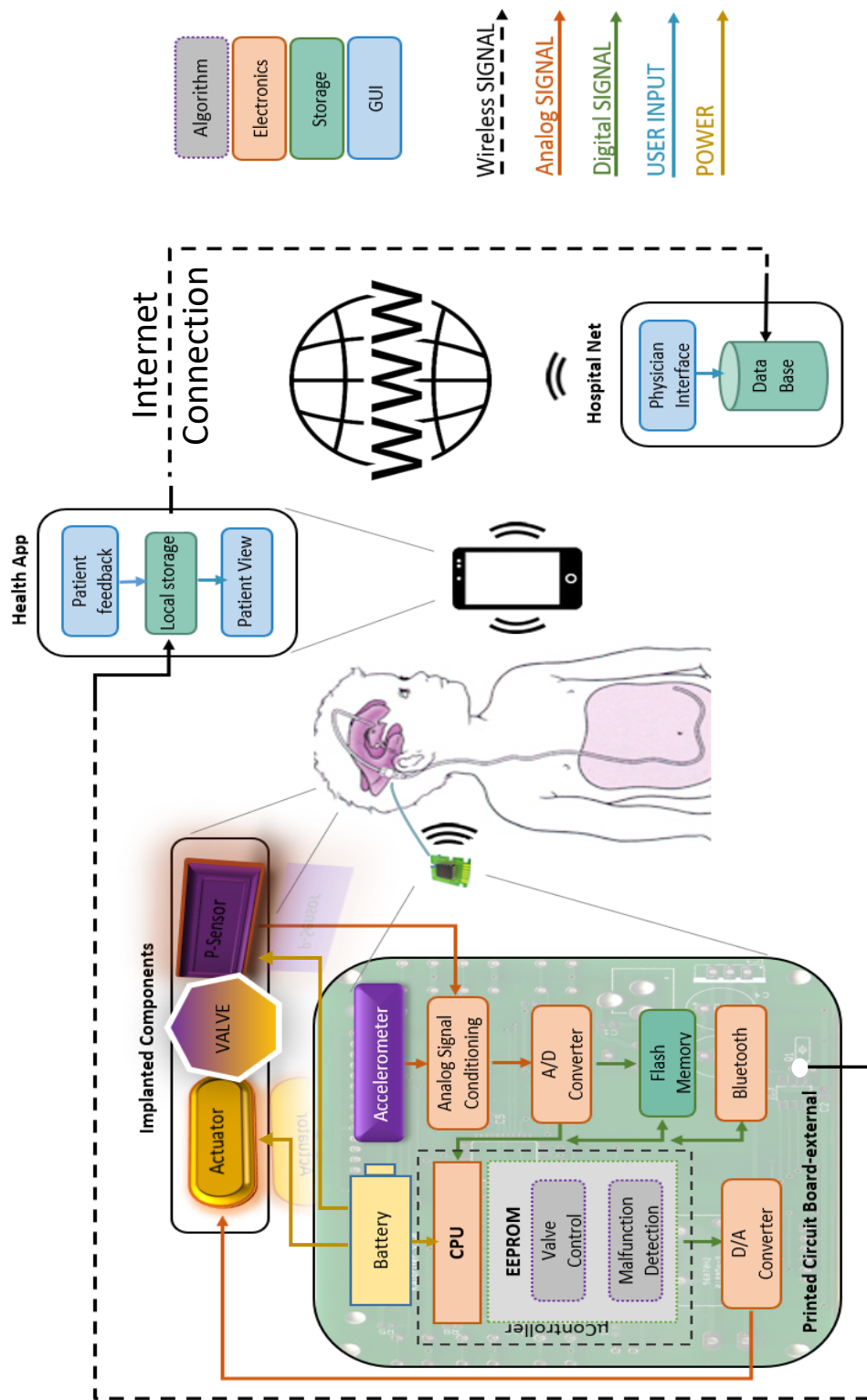


Figure 3.4: Data flow and components of the active shunt. It includes four major components. The printed circuit board, the implanted valve, the smart device, and the database

3.4 Conclusion

The active shunting system can actively combat a number of the shortcomings, failures, and issues that face the currently used mechanical shunts. It combats over-drainage resulting from hydrostatic pressure and from events that cause ICP spikes, such as coughing and sneezing. The system offers a personalised method of managing the HC disease, and it also provides the extremely needed feature of shunt fault detection as current shunt systems failure statistics are very high. It combines sensory input and patient feedback to detect fault types.

The system consists of multiple components, including a piezoresistive type acceleration sensor that detects the patient's position and a piezoresistive pressure sensor that is mounted on the tip of the proximal catheter to measure ICP levels. This system also includes a control unit that acts as a communication module for the different components of the system. It is also the platform where drainage and fault detection algorithms are installed. The system is powered by a lithium-based rechargeable battery using conductive coupling.

The system can change the patient's experience regarding the management of their HC condition. Patients with implanted shunts visit their physician often to adjust their shunt's opening pressure, check for possible shunt faults, and carry out necessary revisions. This restricts the patient's ability to travel as they ensure they have access to their physician at all times. Furthermore, one of the biggest issues surrounding the diagnosis and treatment of hydrocephalus is that the condition remains poorly understood. The constant monitoring of patients can generate massive data that can help fill the gaps concerning the hydrocephalus condition.

Chapter 4

VALVE MECHANISM

4.1 Introduction

The conceptualisation process of the electromechanical valve layout, components, and operation method is explained in this chapter. The valve must be compatible with the active shunting system discussed in chapter three. Hence, the main requirement of the valve is that it should have the feature of being actively controlled. The methodology used to achieve this includes conducting an ICP dynamic modelling process to further understand the difference between passive and automated valves and their effects on ICP and CSF. Based on the results of the dynamic model, different factors are put in place to assist with the selection process of the valve mechanism components. These factors are necessary as there are different operational restrictions associated with this implanted system. This chapter aims to study the conditions under which the electromechanical valve is to operate, which is the first step of the design process. Based on these conditions, an appropriate design concept is proposed.

Numerous valve layouts and components are discussed, and the most appropriate valve design for the drainage operation is selected. This is achieved by reviewing different types of actuation mechanisms and fluid diversion methods, where the concept design layout is chosen based on the selection factors put in place.

4.2 ICP Dynamics

A better understanding of how standard and fully automated (controlled) closed-loop valves manage ICP is necessary to provide an appropriate design layout of the valve. Elevated ICP is a complicated and not fully understood phenomenon that occurs due to brain injury, brain tumours, and hydrocephalus. Several CSF flow models exist, such as brain tissue displacement, anatomical structure, and stress-strain distribution in the tissue [112]. However, the interest here is solely on the hydrodynamics of CSF flow as it is needed to assess the operation of different valves. The main method to improve the treatment of elevated ICP used to be animal models [113]. However, many ICP-generating models have been formulated since. Some of these models make use of electrical circuit principles, while others utilise control theory. Although many theories were brought forward before the 1970s, Anthony Marmarou's theory was the first to contain all components (CSF production, absorption, circulation, and storage) within the theory structure [112,114,115]. He expressed his theory in the form of an electrical circuit model to showcase CSF circulation, where pressure represented the circuit voltage.

4.2.1 Mathematical Model

The current widely used assumption is that the space in the skull can be addressed as a closed cavity. The volume inside consists of the blood, tissue, and CSF volume. From this assumption, the so-called “Monro-Kellie doctrine” equations below are derived [7]:

$$\begin{aligned} \text{Total Volume } (V_{total}) = & \text{CSF Volume } (V_{CSF}) + \text{Blood Volume } (V_{blood}) + \\ & \text{Tissue Volume } (V_{tissue}) \end{aligned} \quad \text{eq 4.1}$$

$$V_{CSF}(t) = \int (\dot{V}_{produced}(t) - \dot{V}_{resorbed}(t) - \dot{V}_{drained}(t)) dt \quad \text{eq 4.2}$$

Where V_{CSF} is CSF volume (cm^3), $\dot{V}_{produced}$ is the CSF volume flow rate being produced by the choroid plexuses (cm^3/s), $\dot{V}_{resorbed}$ is the CSF volume being absorbed in the arachnoid granulations by the sagittal sinus (cm^3/s), and $\dot{V}_{drained}$ is the CSF volume being diverted by the valve (cm^3/s). Where \int refers to antiderivatives and not integrals. CSF production is related to arterial blood pressure and intracranial pressure as follows [7,116]:

$$\dot{V}_{produced}(t) = \beta_{production} \cdot (ABP(t) - ICP(t)) \quad \text{eq 4.3}$$

Where ABP is the arterial blood pressure (mmHg), ICP is the intracranial pressure (mmHg), and $\beta_{production}$ is a constant representing the CSF formation resistance ($\text{cm}^3/\text{mmHg.s}$). Several models exist for the ABP as it can be represented as a variation with a frequency and amplitude [117] or represented as a function of arterial radius and body inclination [118,119]. However, the model used represents ABP as a wave [120] as follows:

$$ABP(t) = 17.5 \sin\left(2\pi t - \frac{\pi}{2}\right) - 12.5 \sin(4\pi t) + 16000 \quad \text{eq 4.4}$$

Note that this equation gives ABP in Pa, so it must be multiplied by the factor of 0.007500617 to get the value in mmHg. Next is the volume absorbed by the Sagittal Sinus, which is represented as follows [7,116]:

$$\dot{V}_{resorbed}(t) = \begin{cases} 0 & , ICP < UL_R \\ \beta_{resorption} \cdot (ICP(t) - VBP(t)) & , else \end{cases} \quad \text{eq 4.5}$$

UL_R represents the upper limit that when the ICP reaches, the absorption starts (mmHg). VBP is the venous blood pressure (mmHg) and $\beta_{resorption}$ is a constant representing the absorption resistance ($\text{cm}^3/\text{mmHg.s}$). It must be mentioned that reverse flow through the arachnoid granulations is impossible [114]. VBP is taken as a constant (≈ 4 mmHg) in some models

[7,116]. However, the model used takes into consideration the body inclination effect on VBP as follows [118,119]:

$$VBP = P_m - \Delta P_{inclined} \quad \text{eq 4.6}$$

$$P_{inclined} = \frac{L \cdot \sin(\Psi)}{13.595} \quad \text{eq 4.7}$$

Where P_m is the mean level of VBP (≈ 4 mmHg), $\Delta P_{inclined}$ is the change in pressure as a result of position (mmHg), L is the distance between the heart and the head (mm), and Ψ is the inclination angle measured from horizontal in degrees. The 13.959 is a conversion factor from mmH₂O to mmHg. $V_{drained}$ is introduced for patients with hydrocephalus. In the case of standard mechanical valves, the following equations are used:

$$\dot{V}_{drained}(t) = \begin{cases} 0 & , P_{valve} < OP \\ \eta_{d.v} \cdot (P_{valve}(t) - OP) & , P_{valve} \geq OP \end{cases} \quad \text{eq 4.8}$$

$$P_{valve}(t) = ICP(t) - P_{distal} + P_{hydrostatic}(t) \quad \text{eq 4.9}$$

$$P_{hydrostatic}(t) = \rho g h \cdot \sin(\Psi(t)) \quad \text{eq 4.10}$$

P_{distal} is the pressure at the distal end (drainage site) (mmHg). $ICP - P_{distal}$ represents the differential pressure (DP), P_{valve} is the pressure acting on the gate of the valve (mmHg), and $P_{hydrostatic}$ is the hydrostatic pressure (mmHg). The valve only opens if the value of P_{valve} reached the designed opening pressure (OP) of the valve. $\eta_{d.v}$ is the differential pressure valve flow permissivity ($\text{cm}^3/\text{mmHg}\cdot\text{s}$), which is a constant representing the standard valve flow capacity or resistance. ρ is CSF density (kg/m^3), g is the gravity (m/s^2), and h is the distance

between the drainage site and the cranial cavity (mm). The equation is multiplied by the inclination angle Ψ to obtain the real height of the column of liquid. The equation must also be multiplied by the factor 0.007500617 to get the value in mmHg. As seen from eq 4.9, the pressure controlling the opening and closing of the valve is not the ICP but rather the pressure difference at the valve gate. In the case of an automated valve (closed-loop valves), another set of equations is adopted from eq 4.8 as follows:

$$\dot{V}_{drained}(t) = \begin{cases} 0 & , ICP < LL \\ \eta_{a.v} * (ICP(t) - UL) & , ICP > UL \\ \dot{V}_{drained}(t - 1) & , otherwise \end{cases} \quad \text{eq 4.11}$$

Where UL and LL are the upper and lower limits of ICP (mmHg), and $\eta_{a.v}$ is a constant representing the closed-loop automated valve resistance ($\text{cm}^3/\text{mmHg}\cdot\text{s}$). Note that the actual ICP values are used for the pressure sensor-based closed-loop valve. The $\dot{V}_{drained}(t - 1)$ term indicates that when $LL < ICP < UL$, the last status of the valve is repeated. The second term of eq 4.1 is the blood volume, which is equal to the sum of the venous blood volume V_{venous} (cm^3) and the arterial blood volume $V_{arterial}$ (cm^3) as follows [115,120]:

$$\dot{V}_{blood} = V_{arterial}(t) + V_{venous}(t) \quad \text{eq 4.12}$$

$$\dot{V}_{blood} = \alpha_{arterial} \left(\frac{d(ABP(t) - ICP(t))}{dt} \right) + \alpha_{venous} \left(\frac{d(VBP(t) - ICP(t))}{dt} \right) \quad \text{eq 4.13}$$

Where \dot{V}_{blood} is the blood volume flow rate (cm^3/s), while $\alpha_{arterial}$ and α_{venous} are the compliance for the intracranial arterial and venous compartments (cm^3/mmHg), respectively. The first and second terms of eq 4.13 represent $V_{arterial}$ and V_{venous} , respectively. The last term in eq 4.1 is the tissue volume, which is represented by [115]:

$$\dot{V}_{tissue} = -\alpha_{tissue} \frac{d(ICP(t))}{dt} \quad \text{eq 4.14}$$

Where α_{tissue} is the compliance of the tissues (cm^3/mmHg). Finally, a model is needed to link the ICP with the total volume in eq 4.1. Some models assume a linear relationship between the two parameters, but that linearity is only feasible for values not far from the optimal range [117]. The model used links ICP values and total volume by using an exponential relation as follows [7,116]:

$$ICP(t) = P_0 + K_{elastic} e^{\phi V_{total}} \quad \text{eq 4.15}$$

Where P_0 is the reference pressure (mmHg), $K_{elastic}$ represents the modulus of elasticity of the venous compartment (mmHg), and ϕ is a variable that relates to the exponential relation between ICP and volume (cm^3). These sets of equations are used to produce an ICP signal to simulate ICP readings from a patient with the hydrocephalus condition. The effect of having both a normal classical shunt valve and an automated valve on drainage is to be analysed as this can assist with selecting the electromechanical valve mechanism.

4.2.2 Dynamic Simulation Setup

Usually, the process of modelling ICP consists of recreating already available patient ICP data. This is carried out as the modelling process usually attempts to predict the patient's ICP level based on the existing data. It is achieved by adjusting the different parameters in a trial-and-error manner until the mathematical model output matches the existing ICP history data. However, in this case, the interest is only in developing an ICP signal in order to understand the impact of different shunts on it. Thus, these parameters are not modelled after any historical data. Simulink is used for this dynamic simulation, where the overall simulation block is shown in Figure 4.1, while the remaining simulation blocks are presented in Appendix-1.

The simulation was carried out for a period of 15 seconds. This low time period is a result of simulating arterial blood pressure (ABP) at a fine time step of 0.001 s. This is carried out to ensure that the ABP profile is as smooth as possible. The parameters chosen for the modelling of ICP are shown in Table 4.1. These parameters were chosen based on a trial-and-error to simulate the ICP signal in a patient with a hydrocephalus condition. As the ICP level for a healthy individual is between 5 and 15 mmHg [1], the parameters were selected to reflect a rapid increase of ICP beyond that level to simulate severe hydrocephalus. The passive valve is then set to drain CSF when ICP exceeds 15 mmHg, while the automated valve is set to keep ICP between 14.5 and 15.5 mmHg.

Table 4.1: Parameters used for mathematical modelling of CSF

Parameter	Value	Parameter	Value
$\beta_{production}$	$4.1894 \times 10^{-4} \text{ cm}^3/\text{mmHg}\cdot\text{s}$	$\eta_{a.v}$	$1 \text{ cm}^3/\text{mmHg}\cdot\text{s}$
$\beta_{resorption}$	$104.167 \times 10^{-5} \text{ cm}^3/\text{mmHg}\cdot\text{s}$	OP	5 mmHg
UL_R	40 mmHg	P_{distal}	6 mmHg
P_m	$\approx 4 \text{ mmHg}$	ρ	997 kg/m ³
L	100 mm	g	9.81 m/s ²
h	100 mm	α_{venous}	0.46 cm ³ /mmHg
$\eta_{d.v}$	0.02 cm ³ /mmHg·s	α_{tissue}	0.3 cm ³ /mmHg
UL	15.5 mmHg	P_0	7.5 mmHg
LL	14.5 mmHg	$K_{elastic}$	0.26 mmHg
$\alpha_{arterial}$	0.15 cm ³ /mmHg	ϕ	0.26 cm ³

P_m was modelled as a random number between 3-5 mmHg to showcase the irregularity of ICP

UL_R is set at a high value to simulate hydrocephalus conditions, as CSF is not absorbed using normal pathways

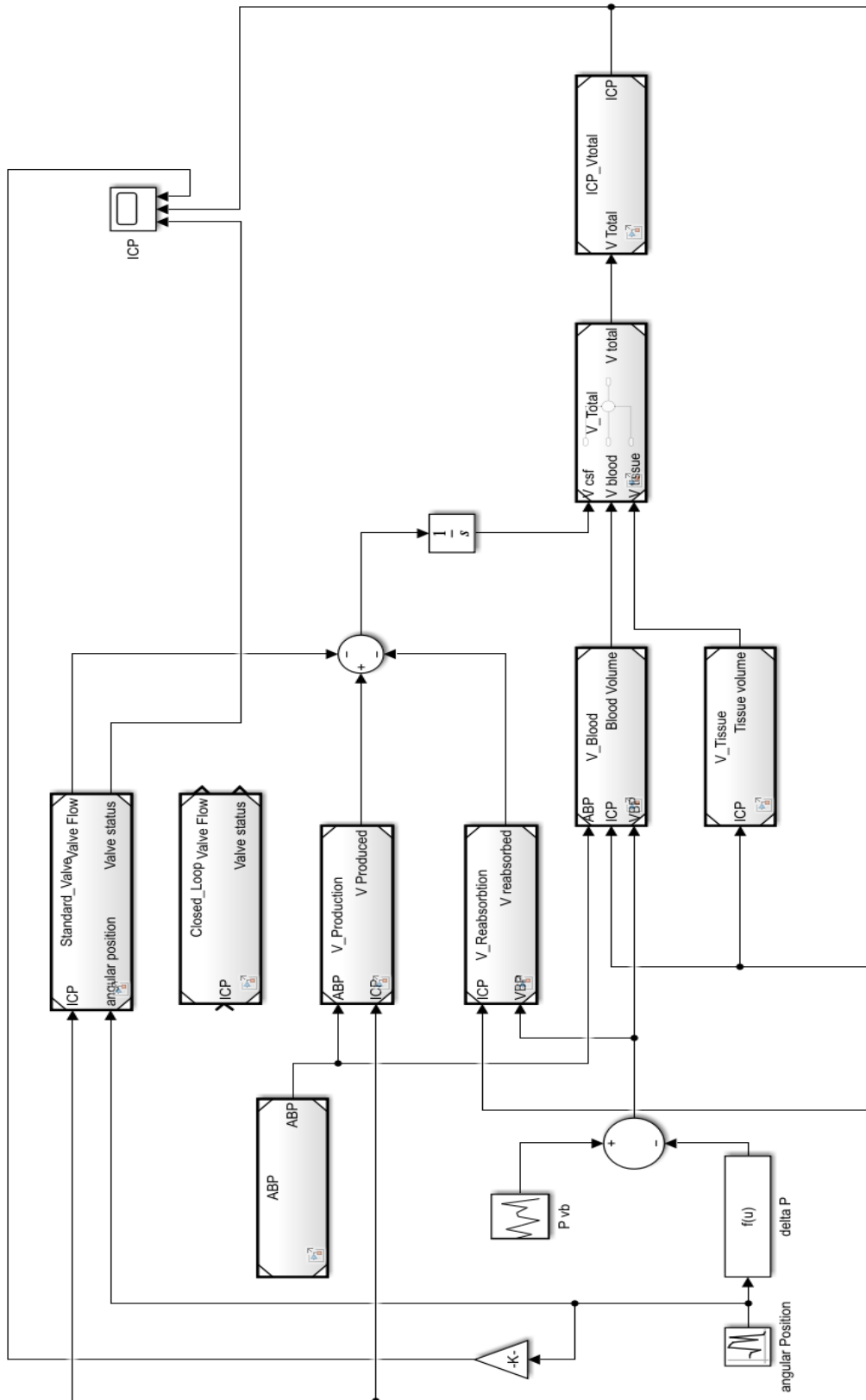


Figure 4.1: Simulink simulation block. The block generates ICP levels and simulates its response to both standard and automated shunt valves

4.2.3 Dynamic Simulation Results

The model considered the effect of hydrostatic pressure and the changes in ICP levels due to changes in body inclinations. Figure 4.2b presents the ABP wave, which is very smooth, ensuring that appropriate parameters and an appropriate time scale are used. A close look into the generated signal in Figure 4.2a shows the constant natural irregularity and instability of ICP. Figure 4.2c shows how a normal mechanical shunt handles ICP where the valve was set to keep ICP below 15 mmHg. It can be seen that the shunt is keeping the ICP much below the wanted level. This is a result of the hydrostatic pressure and the sudden fluctuations in ICP due to changes in head inclination. On the other hand, the automated shunt in Figure 4.2d was set up to keep ICP between a *LL* of 14.5 and *UL* of 15.5 mmHg. While the controllable shunt is managing to keep pressure within those limits, it is not keeping ICP as smooth as the standard valve. This is the result of the continuous operation of the standard valve compared to the automated valves. The classical valve goes through 132 open/close cycles with the current simulation setup, while the automated valve goes through only 41 cycles. This demonstrates that the classical valve is about three times (320%) more active than the automated one. This can be improved by using smaller *LL* and *UL* limits. However, this leads to increased valve operation levels which can be problematic in a system that runs on a limited power source. It must be pointed out that in a closed-loop system, the ICP signal must be processed first and filtered before it is used to make a drainage decision. However, this simulation focuses on the real impact of ICP levels on the valve status, which is why no signal processing was implemented.

To summarise, the standard valve has a 320% more active operation pattern than the automated valve. However, hydrostatic pressure and other events that affect the ICP level do not affect the automated valve. These results show that a merge between the standard valve's active response and the automated valve's controllability is the most advantageous option.

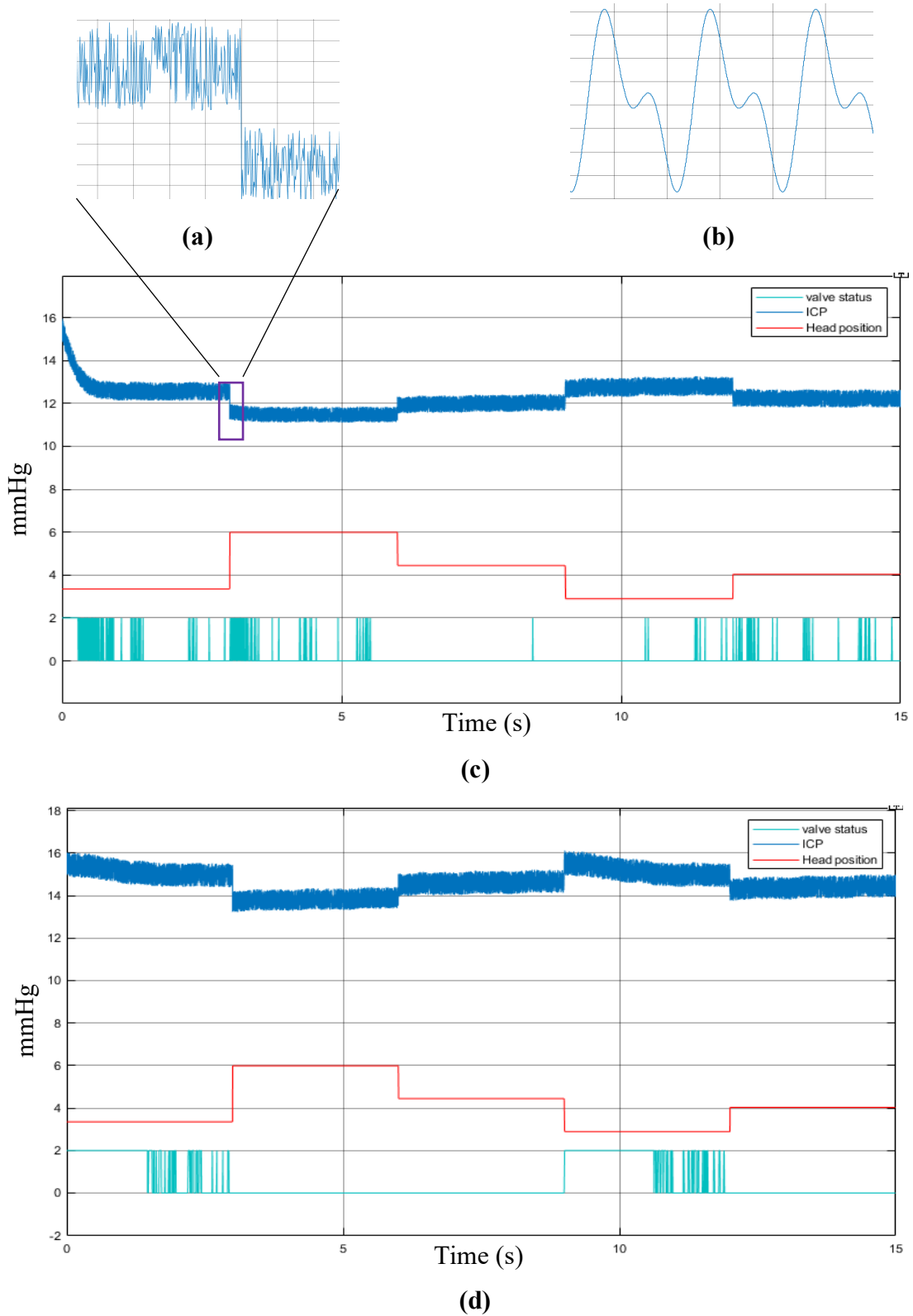


Figure 4.2: ICP shunting simulation results. (a) Zoomed-in version of the overall generated ICP signal. (b) The generated ABP signal at a time step of 0.001s. (c) Classical mechanical shunt ICP management. (d) Fully automated shunt ICP management

4.3 Valve Concept

Based on the dynamic simulation, it is clear that a hybrid valve with both the controllability of an automated valve and the passive continuous operation of a normal mechanical valve is needed. The electromechanical valve consists of two main components, which are the CSF flow diversion mechanism and the power delivery mechanism (actuation). The mechanism selection of those two components depends on the factors below:

- 1- **Size and compactness:** This is simply a space issue, as the valve needs to be small since it is implanted under the skin in the area above the ear. This is more of an issue since both the valve and the control unit – as mentioned in chapter three – must share this space. The valve also needs to be designed in a way that all components can be contained in a single housing.
- 2- **Component's suitability:** This relates to the materials' bio-compatibility since most materials can cause infections when implanted in the body. Materials such as silicon, titanium, and magnesium must be used to reduce the chances of these infections. Suitability also relates to materials that can cause magnetic interference with MRI machines, such as magnetic elements.
- 3- **Power consumption:** as the valve must be a long-term implanted management system, it is essential to keep power draw at a minimum. This is mainly a concern regarding the actuator to be used to operate the valve.

These three factors are the main guidelines to follow during the conceptualisation process of the layout and design of the hybrid valve. In addition, the valve must possess the hybrid operation feature, where it has both the constant activeness of a passive valve and the controllability of an automated one.

4.3.1 Valve Components

The first component of the hybrid valve is the fluid diversion mechanism, which represents the replacement for the current ball-in-cone valve used in programmable and fixed passive valves. The two main options considered for this mechanism are the membrane and classic methods. The membrane method utilises silicon membranes – also known as pneumatic – or elastomers to obstruct and control the flow. They are ideal for controlling flow in small channels. They are usually used as passive fixed valves where the membrane elasticity and preloaded pressure define the characteristics of the system [121]. Due to the nature of the silicon membranes, they can only be actuated through directly harnessing magnetic energy or harnessing stress from piezoelectric materials. The use of magnetic energy for this purpose is not a viable option as it can cause magnetic interference with MRI machines. Also, directly harnessing stress from piezoelectric materials requires a voltage of about 60 V [121,122], which is considered high for an implanted system. A new actuation method for silicon membranes that is being researched is the use of electrostatic energy by means of dielectric charging. However, it is also considered a non-viable option as it also requires a high voltage of 60 to 200 V [123].

The second option for the fluid diversion mechanism is the use of classical methods such as ball valves, gate valves, needle valves, and butterfly valves. Each one of these valves has different features, such as operation torque, self-locking abilities, rapid operation abilities, manufacturability, and their general stand on the three selection factors mentioned above. Friction is considered both an advantage as it provides locking and a disadvantage as it increases the operational torque, thus increasing the required power.

The second component of the hybrid valve is the actuation method, which depends on the type of fluid diversion mechanism used. The two main options considered are motorised magnetic actuation and motorised piezoelectric actuation. The piezoelectric effect refers to the ability of

certain materials to generate an electric charge when they are subjected to mechanical stresses. The most important feature of this effect is that it is reversible, meaning those materials can generate mechanical stress when electricity is applied. The two piezoelectric motor types that operate utilising this phenomenon are the ultrasonic motor and the walker motor. The ultrasonic motor operates by electrically inducing ultrasonic vibration in the piezoelectric component (stator) that is attached and preloaded against a rotor. The friction between the stator and the rotor, combined with the excitation of the stator, delivers physical movement to the rotor [122,124,125]. The walker piezoelectric motor operates by harnessing the piezoelectric phenomena directly. This is achieved by using two types of stacks that are polarised differently. The first stack produces vertical elongation when electrically charged, while the second stack produces horizontal elongation when charged. By arranging stacks in a specific way, actuator movement can be achieved.

The second actuation option is the use of basic magnetic motors such as stepper motors. However, the piezoelectric motors have a much more accurate step definition than the magnetic motors. Features of each motor type include power requirement, MRI compatibility, reliability, safety, and self-locking features. A more detailed description of these different options for valve actuation is presented in Table 4.2 below.

Table 4.2: Options available for shunt valve actuation

Actuator	advantages	disadvantages	notes
Stepper motor	<ul style="list-style-type: none"> - Can be designed to keep voltage requirements to a minimum. - Very reliable with a long life span. - Simple wiring procedures. - Overload safe as it cannot be damaged. 	<ul style="list-style-type: none"> - Can be magnetically interfered with. - Only self-locking in the energized state. - Extended operation can produce heat. - Requires a motor driver to control (H-bridge). - Components (coils, stator, rotor) affect the size of the motor. - Requires a position-sensing device. 	<ul style="list-style-type: none"> - The motor can withstand a certain level of torque without being energized (holding torque). This depends on the design of the motor (mainly size). - The H-bridge is required as the same wire in a stepper motor is required to change polarity during operation.
Piezoelectric Ultrasonic motors	<ul style="list-style-type: none"> - Very high step definition. - Self-locking in the off-state. - Due to the self-locking off state, a position sensor is not required. - Low voltage requirement. - Extremely compact. - No magnetic interference. 	<p>Depending on the design, it might require a board to be mounted on.</p>	<p>Depending on the design and the orientation of the system, the number of piezo elements can be kept to the bare minimum (possibly down to two elements).</p>
Piezoelectric Walker actuator	<ul style="list-style-type: none"> - Very high step definition - Self-locking in the off-state. - Due to the self-locking off state, a position sensor is not required. - No magnetic interference. - High holding torque. 	<ul style="list-style-type: none"> - High voltage requirement. - Requires extra components compared with the ultrasonic motor (springs). 	<p>Only appropriate for linear actuation.</p>

From Table 4.2, it is clear that a piezoelectric motor system is more appropriate to use. The fact is that having a stepper motor implanted with all of its components is not a feasible option. More importantly, the stepper motor's magnetic nature could cause magnetic interference with MRI machines or other magnetic devices. Hence, the stepper motor fails to adhere to the compactness and component suitability factors put in place for this conceptualisation process. Piezoelectric motors are small in design and have minimal moving parts. The walker actuator has a higher voltage requirement than the ultrasonic system, posing a challenge to implanted batteries' capabilities. Both piezoelectric motors have the extremely important advantage of being self-locking in the off position, which is necessary to keep the power draw at a minimum.

4.3.2 Valve Layout

The valve layout that was found to possess the utmost advantages based on the available options is shown in Figure 4.3 below, as it utilises an ultrasonic element to move a stator that is linked to a spring. The ball and spring system acts as a conventional mechanical valve requiring no external power to actively manage ICP. The opening pressure of the valve is altered by controlling the stator, which acts upon the spring length. This causes a variation in the spring tension and stiffness, changing the level of force required to push the spring. This causes the valve opening pressure to change. The valve is the core part of the active shunting system and is where all decisions made by the system are translated into output. As the physician decides on the appropriate pressure setting based on the requirement of the patient, this is translated to the valve as a specific number of voltage cycles required to have the ultrasonic motor move the spring to a length that corresponds with the selected pressure setting. As the patient changes position from supine to standing, the accelerometer senses the change. Then, a new higher pressure setting that takes into consideration hydrostatic pressure and corresponds with the original pressure setting is applied. The exact same process is reversed

when the patient switches from a standing position to a supine one. When events of coughing and sneezing are detected through sudden ICP spikes and the accelerometer feedback, the valve can briefly shut drainage by locking the spring into its minimum length. This allows for no CSF drainage regardless of pressure to prevent any unnecessary drainage.

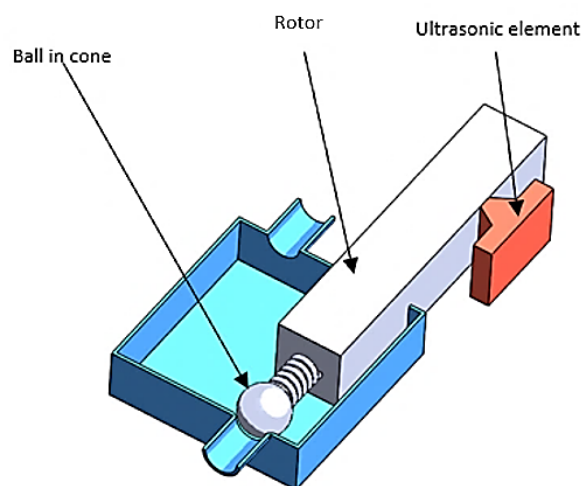


Figure 4.3: Proposed electromechanical valve design layout. It consists of an ultrasonic element supplying movement to the preloaded stator that controls the ball in the cone mechanism

This combination makes use of the advantages of both passive and fully automated valves. An important feature of this system design and layout is that it can continue to function safely and smoothly in case the valve's electronics fail. Thus, in case such failure occurs, the system starts behaving as a mechanical fixed valve with an opening pressure set by the last working point of the ultrasonic element. Most importantly, the proposed layout meets all three selection factors that were put in place earlier. The main issue of the design is that it does not address the blockage issue, as it requires a flushing motion. This can only be achieved – in a controllable method – by using a miniature pump. However, the size and power limitations do not allow for such a component to be part of the design. This, coupled with the fact that the majority of

blockage occurs – as mentioned in section 2.2.2 – in the proximal catheter, where a flushing motion cannot be induced as it can interfere with the brain hydrodynamics, proves that the addition of a miniature pump is disadvantageous. The pump addition adds extra moving parts, such as rotors and gearing components. The current design has only one moving part – the rotor – since the ultrasonic element provides motion while it is stationary. The valve is also feasible from an engineering perspective since its manufacturing processes do not require a significant change in the manufacturing process of the current shunts. The major difference is the ultrasonic element, which is produced through precision machining. It must be mentioned that one of the earliest promising design concepts – Figure 4.4 – involved the use of an ultrasonic motor combined with a butterfly gate. The mechanism is smaller than the currently proposed valve and provides a possibility for throttling the drainage process. This means that the earlier concept could have provided an alternative to opened/closed valves and instead used a valved opening percentage, which could have provided continuous CSF flow. However, no exact advantages were identified for such a feature. In addition, this valve requires a steady supply of power as it needs to be very active during operation, which is the main reason it was discarded.

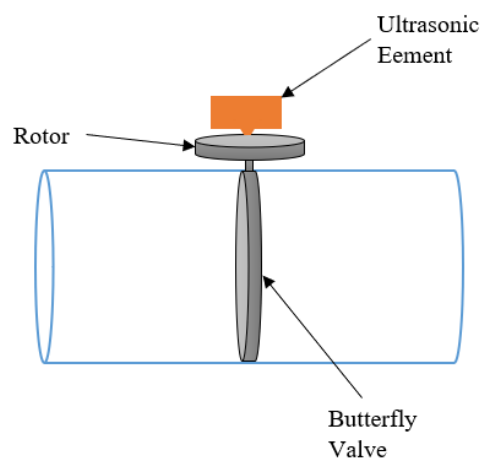


Figure 4.4: Butterfly and ultrasonic element valve concept. The butterfly valve can open partially, allowing for a controllable throttling of CSF flow

4.4 Conclusion

The design of the valve shunt must be compatible with the active shunt discussed in chapter three. In order to achieve this, the effects of different valve types on ICP must be understood. This is achieved by using a mathematical model that considers CSF production, absorption, circulation, and storage. Based on this model, a dynamic simulation was conducted where an ICP signal was generated. The focus was to observe how the ICP signal is impacted by the use of both a fully automated shunt valve and a classical passive mechanical valve. Results showed that while automated valves can combat hydrostatic pressure, passive valves can be up to 3 times more operationally active than automated valves, resulting in a smoother pressure profile output.

Based on those results, it was determined that a hybrid valve system is more appropriate for harnessing the advantages of both valves. This is required in order to achieve both the constant rapid operation of a passive valve and the controllability of an automated one. This hybrid valve components, layouts, and design were selected based on three factors. They are size and compactness, components suitability, and power consumption. The layout of the proposed valve consists of a ball in a cone spring system controlled by an ultrasonic motor, as shown in Figure 4.3. This adds an extremely important safety feature to the valve mechanism as it can simply operate as a normal passive valve in case of failure with the electronics side of the components. Furthermore, it can be seen that this layout covers all the selection factors mentioned. This design is considered feasible from an engineering perspective as it consists of a single moving part.

Chapter 5

ELECTROMECHANICAL VALVE DESIGN

5.1 Introduction

This chapter presents a detailed design of the electromechanical hybrid valve layout showcased in the previous chapter. The valve consists of a fluid compartment, a passive spring in a cone structure, and an ultrasonic motor controlling a beam (rotor) that is attached to the spring. The ultrasonic motor controls the length of the spring, thus changing its stiffness, which in turn changes the opening pressure of the valve.

The methodology followed is divided into three sections, starting with a computational fluid dynamic (CFD) analysis to confirm the fluid compartment's flow properties. The second section is the design of the compression spring system using finite element analysis (FEA) techniques, where the spring design depends on the results of the CFD analysis. The last section is the design of the ultrasonic motor/element, which also utilises FEA design techniques and relies on the results of both the CFD analysis and the spring design results. The design process for all three sections relies highly on computer simulation. The end result is a detailed design and dimensioning of the electromechanical valve in question. This includes the three components mentioned and their different operating conditions.

5.2 Computational Fluid Dynamics (CFD) Analysis

Several numerical methods and techniques are used to approach CFD modelling. These methods are used to approximate a solution of the flow describing equations. These equations are termed “Navier-Stokes” equations and are used to describe the motion and behaviour of viscous fluids. Newton’s second law is employed in these equations and is applied to fluid behaviour. It considers the sum of viscous terms, fluid stress, and a pressure term [127]. The simulation aims to find an appropriate valve geometry that results in adequate flow properties for CSF drainage.

$$\frac{\partial \rho}{\partial t} + \frac{\partial \rho \bar{u}_i}{\partial x_i} = 0 \quad \text{eq 5.1}$$

$$\frac{\partial \rho \bar{u}_i}{\partial t} + \frac{\partial \rho \bar{u}_i \bar{u}_j}{\partial x_j} = - \frac{\partial P}{\partial x_i} + \frac{\partial (\mu \frac{\partial \bar{u}_i}{\partial x_j})}{\partial x_j} + S_{M_i} \quad \text{eq 5.2}$$

Equations 5.1 and 5.2 are known as the “Continuity” and the “Momentum” equations, respectively. Where μ is the dynamic viscosity (Pa.s), ρ is the fluid density (Kg/m³), P is fluid pressure (Pa), u is the velocity vector (m/s), and S_{M_i} is a term that represent external effects (sources).

Three discretisation methods – the techniques by which the “Navier-Stokes” differential equation can be approached as a set of algebraic equations – are used. This includes the finite volume method (FV), the finite element method (FE), and the finite difference method (FD). While the finite difference method is only used on simple geometries, the finite volume and element methods are similar in principle. However, as most CFD modelling packages use the finite volume method, it is used for this simulation. The FV method operates by portioning the flow domain into a number of cells and then integrating the governing differential equation over those cells [128].

5.2.1 CFD Model Setup

CSF can be considered alkaline and is about 99% water, making its properties extremely similar to water. Hence, water properties showcased in Table 5.1 below are used.

Table 5.1: CSF properties used for the simulation [129]

Parameter	Value	Unit
Density (ρ)	994.03	Kg/m ³
Specific gravity (SG)	0.998	–
Dynamic viscosity (μ)	7.9 E-04	N.s/m ²

The specific gravity – also termed relative density – is the density ratio between the fluid in question and water at 4 °C. Dynamic viscosity represents the force required to move a fluid from a standstill point on a horizontal plane, overcoming internal friction between the fluid layers [129]. First, Reynold’s number is calculated from:

$$Re = \frac{\rho V D}{\mu} \quad \text{eq 5.3}$$

Where V is the fluid velocity (mm/s) and D is the pipe diameter (mm). Normal CSF volume production in hydrocephalus patients is usually around 2000 ml/day [130]. The model used has a 1 mm pipe inside diameter for the inlet and outlet, as that is the average inside diameter of proximal and distal catheters [44].

Velocity can be calculated using $V = Q/A$. Where Q is the flow rate (ml/s), and A is the cross-sectional area (mm²). The resulting Reynold's number is 36.7, which clearly indicates a laminar flow. However, it is not low enough for the flow to be considered a creeping flow, as it usually occurs at $Re > 1$. The valve is to be designed for 11 pressure points ranging from 10 to 20 mmHg with 1 mmHg intervals. It is extremely important to take into consideration the effects of hydrostatic pressure. As a result, simulations are run for those 11 points under both normal conditions and those where the hydrostatic pressure is in effect.

The simulation uses pressure at the inlet of the valve. However, as the range specified above is the pressure at the cranial cavity, pressure losses due to friction in the proximal catheter need to be taken into consideration. Friction on the distal end is not considered as outlet pressure is taken as is at the drainage site. This is achieved using the following equations [131]:

$$P_{friction} = \frac{128 \mu L Q}{\pi D^4} \quad \text{eq 5.4}$$

$$P_h = \rho g h \sin(\Psi) \quad \text{eq 5.5}$$

$$P_{inlet} = ICP - P_{friction} \quad \text{eq 5.6}$$

$$P_{h-inlet} = ICP - P_{friction} + P_h \quad \text{eq 5.7}$$

Where $P_{friction}$ is pressure loss due to friction (Pa), P_h is the hydrostatic pressure (Pa), P_{inlet} is the pressure at the valve inlet (Pa), and $P_{h-inlet}$ is the pressure at the valve inlet in the standing position (Pa). L is the proximal catheter length, which is taken at 180 mm [44], g is gravity acceleration (m/s²), h is the column of fluid elevation (mm), and Ψ is the angle of that column. Those parameters are shown in Figure 5.1.

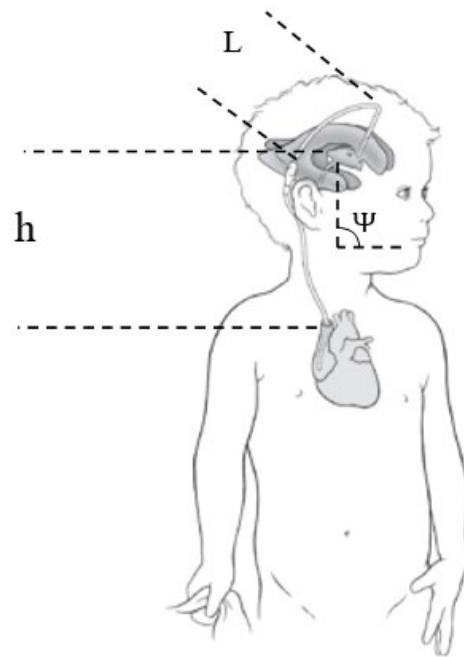


Figure 5.1: Parameters used for pressure calculation [132]

The chosen drainage site for this shunt is the heart. This location is selected to minimise the hydrostatic pressure effects as the distance between the heart and the brain is significantly less than that between the abdomen and the brain, thus resulting in a shorter fluid column. The length between the brain and the heart (h) is approximated to be 300 mm.

The hydrostatic pressure is at its highest at the upright position, which is why Ψ is taken as 90 degrees. This results in a P_h of 2.9 KPa and a $P_{friction}$ of 135 Pa. The design pressure points are shown in Table 5.2 below, as the range selected is between 10 and 20 mmHg with 1 mmHg intervals.

Table 5.2: Electromechanical valve pressure points

ICP (mmHg)	P_{inlet} (E+3Pa)	$P_{h-inlet}$ (E+3Pa)	P_{outlet} (mmHg)/(Pa)
20	2.5	5.4	
19	2.4	5.3	
18	2.2	5.1	
17	2.1	5.0	
16	2	4.9	
15	1.8	4.7	6/800 ¹
14	1.7	4.6	
13	1.6	4.5	
12	1.4	4.3	
11	1.3	4.2	
10	1.2	4.1	

¹ P_{outlet} is shown both in mmHg and in Pa units (6/800).

The total pressure design points are 22 when considering pressure points for normal and hydrostatic pressure conditions. The modelling package used to conduct the flow simulation is STAR-CCM+, a fluid modelling software. It is used to discretise and integrate the governing flow equation into the cells (the mesh) to which the flow domain is sectioned. Further details on the methodology of the flow simulation are shown in Appendix-2. The software presents a solution in the form of contours containing output from each one of the cells. The model boundary conditions and dimensions are shown in Figure 5.2a&b. The dimensions specified are in line – in terms of inlet and outlet diameters – with current catheters available on the market. All walls – including the ball – are set to no-slip boundary conditions or zero velocity gradient. A total of 22 simulations are carried out where the inlet boundary condition – which

is inlet pressure – is taken from Table 5.2. The outlet boundary pressure is the distal pressure. The distal catheter drains the CSF into the heart's right atrium, where the pressure is around 2 to 6 mmHg (800 Pa) [133,134]. Minimum attention was given to refining the wall area mesh as the flow is laminar. However, as seen in Figure 5.2c, a fine mesh was used near the ball area due to the small gap in that area. After conducting a mesh independence study, the ideal number of cells to be used was determined to be 176,000. The mesh independence study is further discussed in section 7.2. The mesh around the ball is made clear in Figure 5.2d, while the symmetry BC used to reduce computation time is shown in Figure 5.2a.

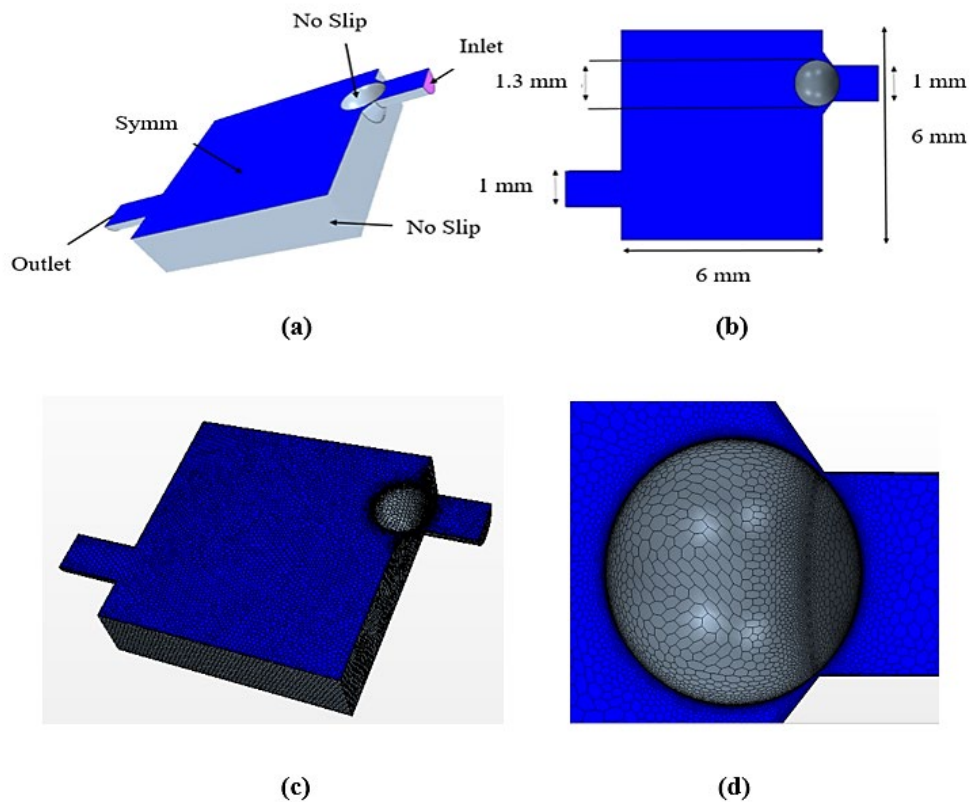


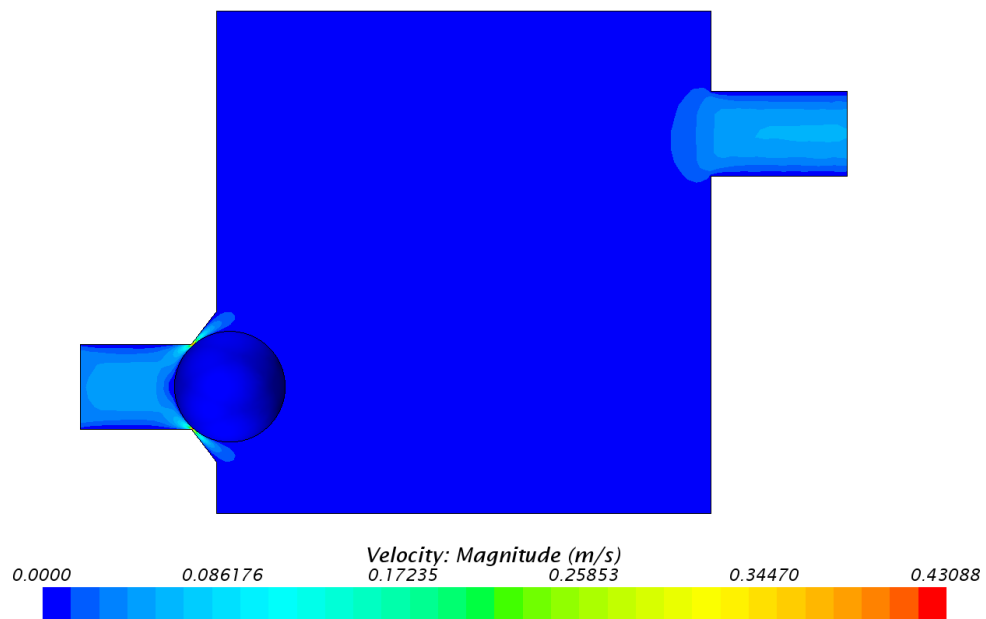
Figure 5.2: Fluid compartment CFD model. (a) Model boundary conditions. (b) Model dimensions. (c) Model mesh. (d) Mesh around the ball. The no-slip boundary condition indicates zero velocity relative to the boundary. Since only half the model is used, a symmetry boundary condition is used to mirror that half

5.2.2 CFD Results

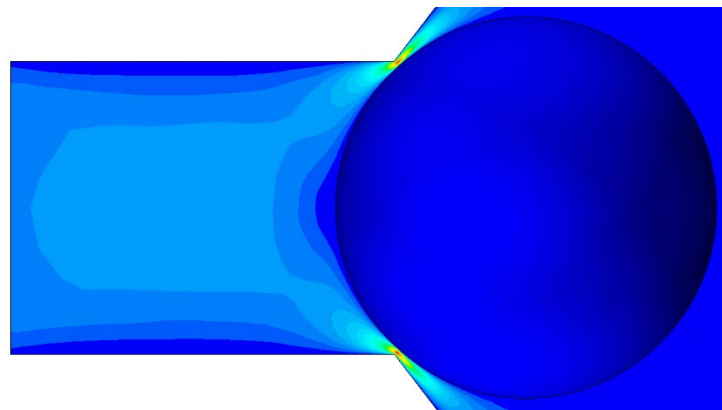
Figures 5.3 and 5.4 show the overall velocity profile – and a zoomed-in section around the ball – in the fluid compartment for the supine 10 mmHg and the standing 20 mmHg pressure points, respectively. High-velocity values are concentrated in the area between the ball and the valve wall on the inlet side due to the small area in that section. Force on the ball as a result of both fluid pressure and shear force on the ball is extracted for each simulation.

These force values are necessary for designing the spring system that controls the ball. The valve offers outflow drainage between 42 and 300 mL/h for the pressure range specified. In terms of forces on the ball, it ranges between 1.5 and 6 E-4 N for pressure points under supine conditions without hydrostatic pressure effects and between 1.08 and 1.47 E-3 N for pressure points at the standing position where hydrostatic pressure is in effect. The details for force and outflow values for each individual pressure point are shown in Table 5.3. These details are used for the spring design in the next section.

As the flow is purely laminar, the results from different simulations are expected to be almost perfectly linear, as the only changing factor is inlet pressure. This is noticed in Table 5.3 as the difference in the force on the ball and outflow values between each pressure point is almost constant. This is ideal as this linearity can assist if smaller pressure intervals are to be implemented, as it can be set up without the need for further simulations. The results for the additional pressure points simulations are showcased in Appendix-3.

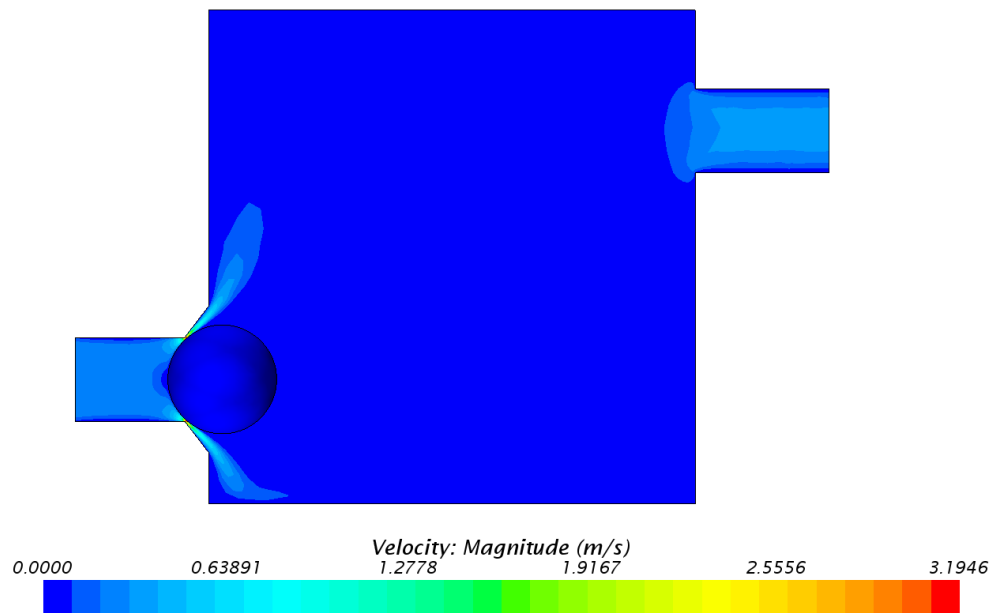


(a)

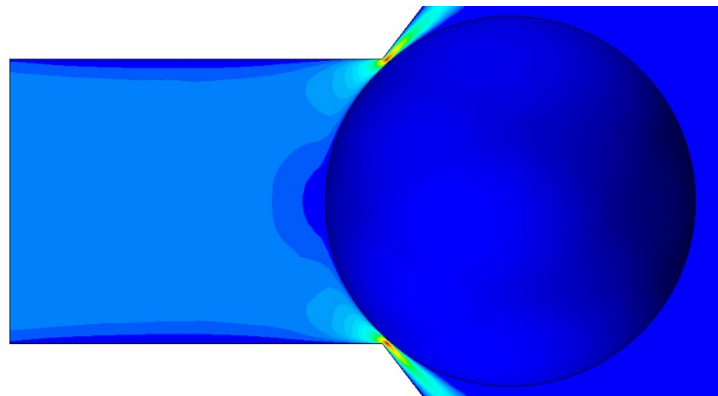


(b)

Figure 5.3: CFD simulation results at 10 mmHg in the supine position. This is considered the minimum pressure point. (a) Velocity profile. (b) Velocity profile around the ball



(a)



(b)

Figure 5.4: CFD simulation results at 20 mmHg in the standing position. This is considered the maximum pressure point. (a) Velocity profile. (b) Velocity profile around the ball

Table 5.3: Force and flow results for ICP pressure points

ICP	Force on the ball (E-4 N)	Outflow (mL/hour)	Force on the ball (E-3 N)	Outflow (mL/hour)
20	6	147	1.48	300
19	5.58	138	1.44	293
18	5.15	129	1.4	287
17	4.72	119	1.36	281
16	4.29	109	1.32	275
15	3.84	99.2	1.28	269
14	3.40	88.7	1.24	263
13	2.94	77.7	1.20	257
12	2.48	66.3	1.16	250
11	2.00	54.3	1.12	244
10	1.52	42	1.08	241

Supine positions are results without the hydrostatic pressure effect, while standing positions are for when the hydrostatic pressure is in effect.

5.3 Spring Design

The steps for designing the spring are to produce an initial design based on chosen design formulas [135–139]. This is achieved based on the results of force generated on the ball from the fluid simulations in section 5.2. This initial design is used as a first iteration where a model is constructed based on those formulas' results. An FEA analysis of the model is conducted to verify the initial design.

5.3.1 Initial Design

The initial design step utilizes known design formulas [135–139] as a starting point for the spring design process. These equations are based on the spring system mathematical model showcased in Appendix-4. First, the spring rate K (N/m) required must be determined as shown below.

$$K = \frac{F_{max} - F_{min}}{L_{min} - L_{max}} \quad \text{eq 5.8}$$

Where F_{max} is the maximum force (N) the spring provides at the minimum spring operating length L_{min} (mm), and F_{min} is the minimum exerted force (N) at the maximum operating length L_{max} (mm). From those parameters, the spring free length or total length is deducted as:

$$L_f = L_{max} + \frac{F_{min}}{K} \quad \text{eq 5.9}$$

Where L_f is the free length (mm). An initial Mean Diameter and wire diameter are then specified. These values are optimised based on the maximum shear stress the spring can withstand and the value of the spring index C , which is given as:

$$C = \frac{D}{d} \quad \text{eq 5.10}$$

Where D is the mean spring diameter (mm), and d is the spring wire diameter (mm). Usually, C is kept between 4 and 15 as springs with C values less than 4 are difficult to manufacture, and springs with C values more than 12 might be prone to buckling (horizontal displacement of the spring middle coils). However, as the application requires fine control of low-magnitude forces, the spring wire diameter needed is quite small, resulting in a larger C value. A separate check for spring stability is performed after the spring dimensions are confirmed. As the spring operates in a cyclic loading condition, stress due to fatigue must be modelled as [139]:

$$\tau_{max} = \frac{8 D K_w F_{max}}{\pi d^3} \quad \text{eq 5.11}$$

Where τ_{max} is the maximum shear stress resulting from operating conditions (Pa). As shear stress is the continuous and dominant stress against the spring, it is used as an indication of the spring's tendency to creep over time due to constant loading under the max shear stress. Creeping can cause spring set – the shortening of the spring's free length – which is directly proportionate to the spring material yield strength. Thus, Materials with higher yield strength than this value must be chosen. K_w is the Wahl factor and is given by:

$$K_w = \frac{4C - 1}{4C - 4} \quad \text{eq 5.12}$$

The next step is to determine the number of active coils (N_a). Based on the types of ends used on the two sides of the spring, the active number of coils might not be equal to the total number of coils. By using the open-ended type, the total number of coils is the same as the number of active coils, as opposed to having another type of end with inactive coils. Active coils can be found through [138]:

$$N_a = \frac{G d}{8 K C^3} \quad \text{eq 5.13}$$

Where G is the modulus of rigidity (Pa), which is a main design factor since a material with low rigidity is required to ensure that the size of the wire diameter is appropriate. From eq 5.13, a lower G value is proportionate to a lower number of coils, which means a larger wire diameter can be used without an extreme increase in the number of coils. The maximum loading condition for the spring needs to be defined, which is achieved using the next set of equations:

$$L_L = d \cdot N_T \quad \text{eq 5.14}$$

$$F_L = K \cdot (L_f - L_L) \quad \text{eq 5.15}$$

$$\tau_L = \frac{F_L \tau_{max}}{F_{min}} \quad \text{eq 5.16}$$

The equations above are used to determine the locking length, locking force, and locking stress. They are given as L_L (mm), F_L (N), and τ_L (Pa), respectively. These are the parameters necessary for the spring to achieve locking conditions where the coils are in full contact with each other. N_T is the spring total number of coils, including any inactive coils. The buckling possibility depends on two factors, which are δ/L_f and L_f/D seen in Figure 5.5, where δ is the deflection which is equal to $L_f - L_{min}$.

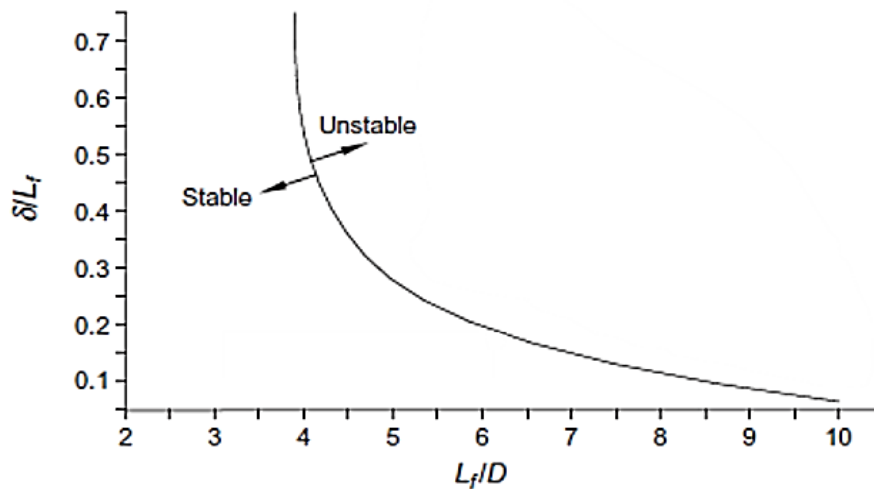


Figure 5.5: Buckling relation to spring ends [136]

Another factor to be aware of is the spring ball, as its weight can interfere with the force the spring is designed to manage. A small mass ball must be used to keep that weight to a minimum to ensure that its effect can be neglected.

$$F_b = m_b \cdot g \quad \text{eq 5.17}$$

$$m_b = \rho \cdot \text{sphere volume} \quad \text{eq 5.18}$$

$$F_b = \frac{\rho_b \pi D_b^3}{6} 9.81 \quad \text{eq 5.19}$$

Eq 5.19 represents the force of the ball due to its mass and gravity, where F_b is the force resulting from the mass of the ball (N), ρ_b is the density of the ball's material (Kg/m^3), and D_b is its diameter (mm). The equation takes the weight of the ball at the standing position where gravity is at its maximum.

It is necessary to make sure that the spring does not reach resonance due to cyclic operation. A phenomenon called spring surge occurs when the spring is excited to the point of its natural frequency. It causes an uneven distribution of displacement across the coils. It must be made certain that the cyclic operation of the spring does not exceed its natural frequency. When the load is fast enough, the first coil is pushed against the second before the rest of the coils respond to the displacement. This disturbance propagates to the rest of the coils, causing the remaining coils to also be in contact. After it reaches the last coil, the disturbance is reflected, where it propagates again in the opposite direction. It only stops when the motion gets damped. The following equations are for the spring natural frequency [136]:

$$f_n = 0.5 * \sqrt{\frac{K}{m}} \quad \text{eq 5.20}$$

$$m_s = \rho_s * V = \frac{\rho_s N_T \pi^2 d^2 D}{4} \quad \text{eq 5.21}$$

Where f_n is the natural frequency of the spring (Hz), m is the spring's mass (Kg), ρ_s is the spring density (Kg/m³), and V is the spring volume (m³). Table 5.4 shows the parameters used in these calculations, which are obtained from the fluid simulation results and the materials used for the design.

Table 5.4: Design parameters for the spring design process.

Parameter	Value	Parameter	Value
F_{max}	1.47 microN	G	17 GPa
F_{min}	0.15 microN	ρ_s	1810 Kg/m ³
L_{max}	4 mm	Yield strength	145 MPa
L_{min}	2 mm	Spring ends	Plain (open)
Spring material	Magnesium AZ91E-T6	Ball material	Magnesium
Elastic modulus	44.8 GPa	ρ_b	1700 Kg/m ³
Poisson's Ratio	0.35	D_b	0.0013 m

F_{max} , F_{min} , and D_b are obtained from the CFD analysis results. Magnesium is used for both spring and ball material as it is biomedically safe, has low density (weight), and has one of the lowest modulus of rigidity available in any metal. This makes it a good match for a spring of this small size, as it is sensitive to low forces and results in a reasonable number of spring coils. The rest of the parameters are selected on a trial-and-error basis as multiple parameters were tested. The values above provided the best results in both the initial design step and the FEA simulation verification step.

The process of determining the right dimension of the spring is carried out by selecting an initial wire diameter d and mean diameter D and then optimising these values based on the resulting stress, coil number, and stability. Calculations for different materials with different properties and multiple spring dimensions are conducted – some of these are shown in Appendix-5 – before settling on the parameters in Table 5.4, as they are the most reasonable design parameters. Table 5.5 shows the calculated dimensions and resulting spring properties.

Table 5.5: Calculated spring parameters and properties

Parameter	Value	Parameter	Value	Parameter	Value
K	0.66 N/m	τ_{max}	32 MPa	δ	2.23 mm
L_f	4.2 mm	N_a	7.12	δ/L_f	0.52
D	1.8 mm	N_T	7.12	L_f/D	2.3
d	0.06 mm	L_L	0.42 mm	F_b	1.917E-05 N
C	30	F_L	2.5E-3 N	m_s	2.06E-07 Kg
K_w	1.04	τ_L	546 MPa	f_n	898 Hz

The effect of the magnesium ball attached to the spring on the spring is neglected. This is carried out due to the low force resulting from it (F_b) on the spring. Its force is only 1.7% of the force resulting from the smallest operating pressure (10 mmHg) on the standing position. As the spring is linear, its spring rate must be constant at any given load.

F_{max} is taken at the highest operating pressure of 20 mmHg on the standing position when the hydrostatic pressure is in effect, while F_{min} is taken at the lowest operating pressure of 10 mmHg in the supine position. The operating length of the spring $L_{max} - L_{min}$ is 2 mm. The spring length for the pressure points on the standing position ranges from 2.6 mm at 10 mmHg to 2 mm at 20 mmHg. The range for the supine position is from 4 mm at 10 mmHg to 3.3 mm at 20 mmHg. Forces resulting on the spring from all the pressure points were checked as the resulting spring rate ranged between 0.64 – 0.66 N/m. As the designed spring rate is 0.66 N/m, the difference is considered minor. Thus, the values in Table 5.5 are taken as the initial dimensions for the spring model. Table 5.6 shows each individual pressure point and its respective spring length.

Table 5.6: ICP pressure points and their relative spring length

ICP	Spring length (mm)	Spring length (mm)
20	3.33	2
19	3.39	2.05
18	3.45	2.11
17	3.52	2.17
16	3.58	2.23
15	3.65	2.29
14	3.72	2.35
13	3.79	2.41
12	3.86	2.47
11	3.93	2.53
10	4	2.6

5.3.2 Finite Element Analysis (FEA)

The finite element method (FEM) is a numerical technique used to solve the partial differential equations (PDEs) used to describe a physical phenomenon. For most problems, a discretization of these PDEs into numerical equations is required. The solution of these numerical equations is considered an approximation to the real solution of the PDEs [140]. This is carried out by discretizing the model domain into discrete elements (mesh). A general governing equation is calculated for each element based on the element type. The general equation form for structural analysis is:

$$\overline{[\delta]} = [K]^{-1} \overline{[F]} \quad \text{eq 5.22}$$

Where $[K]$ is the global stiffness matrix, $\overline{[\delta]}$ is the nodal displacement vector, and $\overline{[F]}$ is the nodal forces vector. This equation is the governing equation that describes the structural status of the spring during simulation.

The dimensions of the model were taken from the results in Table 5.5. Two models are built, the first for maximum displacement at the maximum pressure of 20 mmHg in the standing position, while the second for minimum displacement at 10 mmHg in the supine position. The boundary conditions used consist of fixing the end surface of one side of the spring and applying displacement on the other end surface. There are two ways to conduct the structural simulation. The first is by applying a force to one end of the spring to compare the resulting displacement with the previous hand calculations. The second is applying displacement on one end of the spring to compare the resulting forces with previous calculations. The second approach is used as it can generate reaction forces that are necessary for the validation process discussed in section 7.2.

To simulate maximum loading conditions at 20 mmHg in the standing position, a displacement equal to free length minus the spring length corresponding with this pressure point is applied. Hence, a displacement of 2.22 mm is applied. The same is carried out for the minimum loading condition at 10 mmHg in the supine position, where a displacement of 0.22 mm is applied. This represents loading at L_{min} of 2 mm and L_{max} of 4 mm.

A total of 167,000 elements are used in the simulation as this number of elements proved sufficient to reach a mesh independence status, as to be discussed in section 7.2. The simulation software used is ABAQUS, which is a Finite Element Analysis (FEA) software that models, analyses, and visualises mechanical systems. Abaqus C3D8R elements are used as they are solid linear elements, making them appropriate for a linear 3D analysis of this nature. Figure 5.6 showcases boundary conditions and meshing quality used. The material properties used are those of Magnesium AZ91E-T6 in Table 5.4 above.

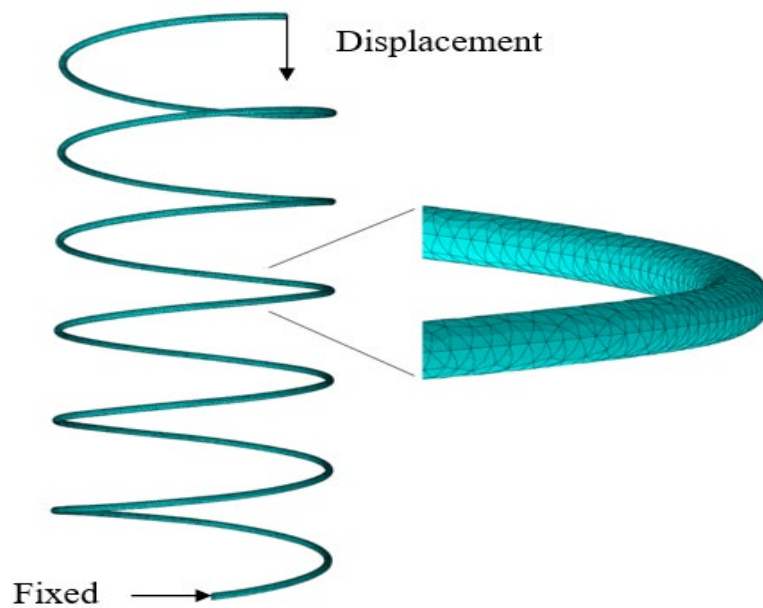
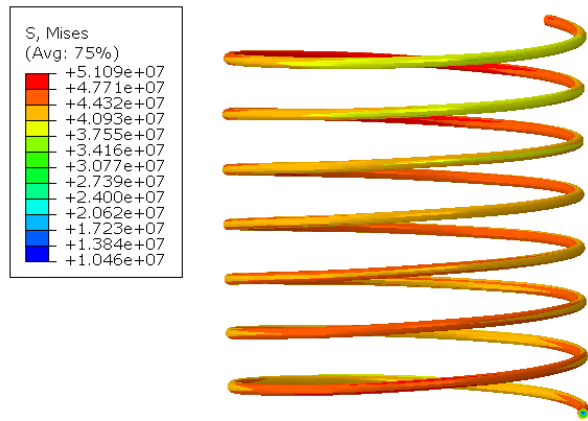


Figure 5.6: Spring FEA model

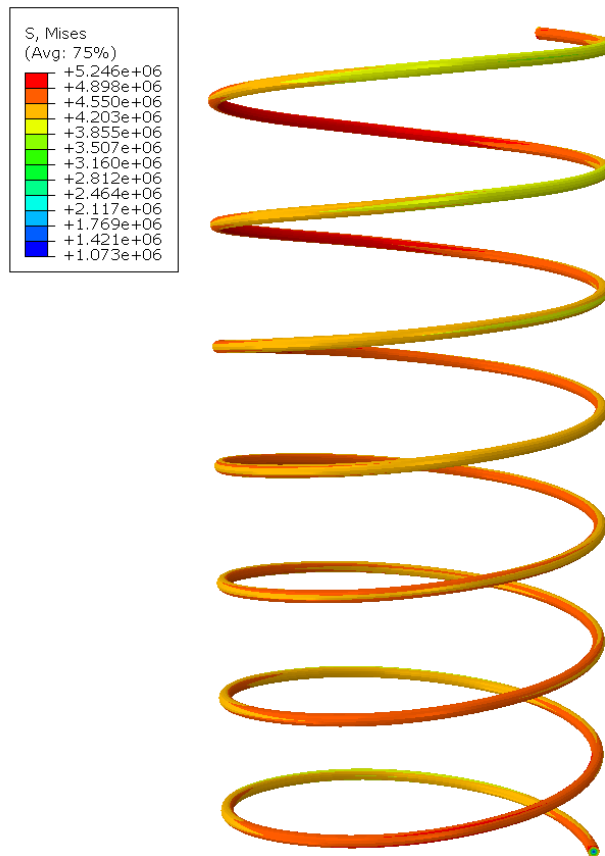
The simulation results are showcased below, where Figure 5.7 illustrates the von-mises stress resulting on the spring at both maximum and minimum loading conditions. At maximum loading conditions of 2.22 mm displacement, the maximum stress is around 51 MPa, as seen in Figure 5.7a. Compared to AZ91E-T6 tensile stress of 275 MPa, the loading is clearly well below the material limits.

Von-mises stress results are a theoretical measure of stress and are used for yield failure measurement in ductile materials. It usually measures more than the real and directly measurable principal stress. This can be seen clearly by comparing Figure 5.7a to Figure 5.8. The maximum measurable principal stress at max loading conditions is 32.5 MPa, which is equal to the calculated τ_{max} of 32 MPa in the previous section. This further ensures that the design parameters of the spring are correct. Additional simulation results are available in Appendix-6.

To summarize, the max von-mises stress that occurs at max loading conditions of 2.22 mm displacement – which correlates to a pressure of 20 mmHg in the standing position – is 51 MPa, which is below the tensile strength of AZ91E-T6 deeming the design safe from a structural aspect. The max principal stress resulting at the max loading condition is 32 MPa, which is equal to the earlier calculated τ_{max} . This indicates that the spring design and parameters are accurate and that the spring will operate as designed.



(a)



(b)

Figure 5.7: Spring von-mises stress results. (a) Maximum loading condition of 20 mmHg at the standing position at a spring length of 2 mm. (b) Minimum loading condition of 10 mmHg at the supine position at a spring length of 4 mm

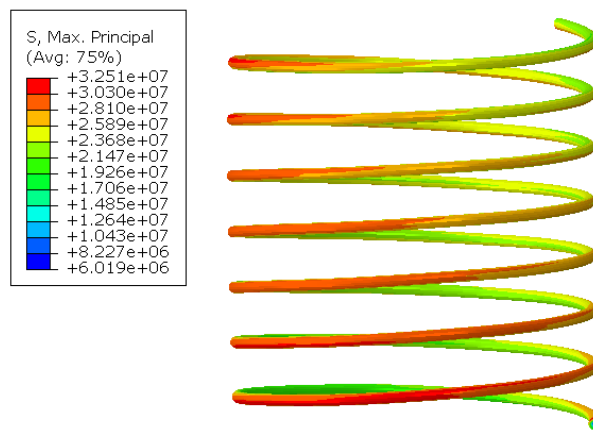


Figure 5.8: Spring maximum principal stresses at max loading condition. It corresponds to 2.22 mm at 20 mmHg at the standing position

5.4 Ultrasonic Motor Design

The operation of the ultrasonic motor depends on mechanical resonance. The ultrasonic element – the rotor – is excited using a high-frequency current. As the element is excited to undergo resonance, the resulting deformation is harvested through friction to induce displacement to the stator. This type of ultrasonic actuator is a single-mode bidirectional motor as it operates under one resonance mode and can be excited to run in both directions. Figure 5.9 presents the model of the motor where it is asymmetrically excited by applying a voltage through one of its electrodes. This results in deformation that gives motion – utilising tip and stator friction – in one direction. The design process for these motors is carried out through an FEA analysis of the piezoelectric element. First, a modal analysis is conducted to visualise different modes of element excitation and which one of these modes is to be used. This is considered the vibration frequency extraction step. The other step is to simulate the partial excitement of the element by applying a low voltage at the previously extracted frequency.

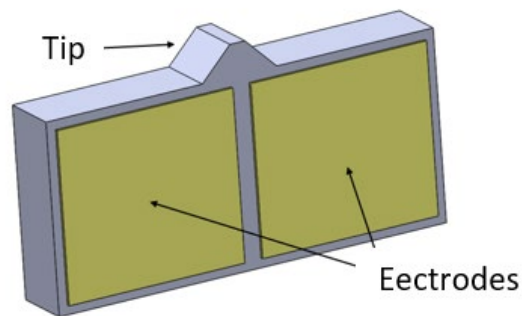


Figure 5.9: Piezoceramic element model. The two electrodes are used for the voltage input. Voltage is applied to each one separately to get a different movement direction. On the other side of the piezoceramic element, a single electrode covering the entire surface is used for ground voltage

5.4.1 Piezoelectric Materials

When an electric field is applied to a solid material, dynamic change – position rearrangement of nuclei and electrons – occurs to its molecules in order to adapt to the applied electric field. As a result, pairs of opposite but equally electrically charged molecules (dipoles) are formed. The process of dipole formation – or alignment of existing permanent or induced atomic or molecular dipoles – under the influence of an external electric field with field strength (E) is called polarisation [141].

Piezoelectric materials are dielectric materials – non-metallic – that can exhibit polarisation. These materials can characteristically generate an electric charge when mechanical stress is applied to them in a specific direction. This occurs in certain ceramics and single-crystal materials [125]. At normal conditions, each molecule's positive and negative charges coincide at the centre of the molecule, resulting in a neutral charge – as illustrated in Figure 5.10a – in the piezoelectric material. However, as external stress is applied, deformation to the structure

of the molecules occurs. As seen in Figure 5.10b, this causes the separation of the positive and negative charge, resulting in a molecular level polarization and causing fixed charges to appear. As a result, an electric field that transforms mechanical energy into electrical energy is generated, as seen in Figure 5.10c. This process is termed the direct piezoelectric effect [142]. The produced electric polarisation by a single crystal is linearly proportionate to the applied mechanical stress, as shown below:

$$\vec{P}_i = d_{ij} \cdot \vec{\sigma}_j \tag{eq 5.23}$$

Where σ is the applied stress (Pa), d is the piezoelectric coefficient (C/N), and P is the electric charge (C). These components are vectors as they depend on specified orientation or direction. Hence i & j represent the different planes.

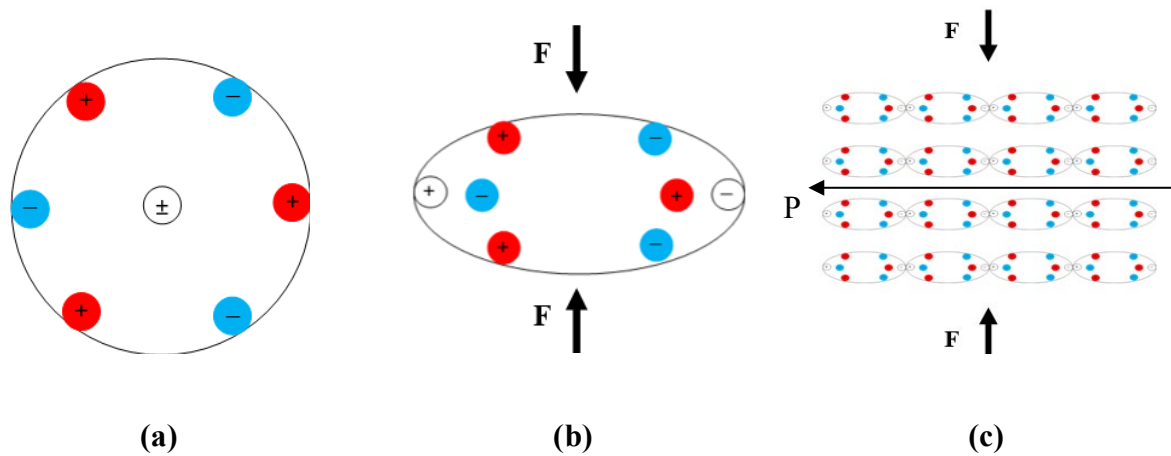


Figure 5.10: Piezoelectric phenomenon on a molecular level. (a) The initial structure of the molecule. (b) Molecule structure after applying stress. (c) Polarised material due to stress

The most important feature of the piezoelectric effect is that it is reversible. Hence, mechanical deformation or distortion can result from applying an electric charge to the piezoelectric material. The applied electric field is also linearly proportionate to the strain, as showcased below by [143]:

$$\vec{\epsilon}_j = \vec{d}_{ij} \cdot \vec{E}_i \quad \text{eq 5.24}$$

Where E is the applied electric field (V/m), and ϵ is the resulting strain. Materials that exhibit piezoelectricity include crystalline materials such as Lithium Tantalate (LiTaO_3) and Quartz. However, the most commonly used piezoelectric material is Lead Zirconate Titanate (PbZrTiO_3) – a ceramic – which is also known as PZT.

5.4.2 Modal Analysis

Acoustic waves spread as compression waves in solid bodies. In bodies where one dimension is larger than the other two, such as beams, these waves are observed in the larger dimension. This indicates that the oscillation of the particles occurs in that same direction. In bodies that are small enough, this can result in creating standing waves, which are two waves with the same amplitude and frequency moving in opposite directions. Also, two-dimensional standing waves are observed in bodies with two dimensions of the same order, such as metal sheets.

These wave types are termed E (k,l), where E refers to “extensional” as these modes cause planar extension. k and l are the numbers of half wavelengths in the X- and Y-direction, respectively [144,145]. For a piezoceramic plate with a length L in the X-direction, height H of $0.5 L$ in the Y-direction, and polarisation in the thickness t in the Z-direction, two E (3,1) modes consisting of 2-D standing waves are observed. The one in the X-direction has 3 half

wavelengths ($L=3\lambda_x/2$), and the one in the Y-direction has one-half wavelength ($H=\lambda_y/2$). The mode shape can be described as [146]:

$$U_x(x, y, t) = -A \sin\left(\frac{3\pi}{L}x\right) \cdot \left(\cos\left(\frac{\pi}{H}y\right) - 1\right) \cdot \sin(\omega t) \quad \text{eq 5.25}$$

$$U_y(x, y, t) = B \left(1 \pm C \cos\left(\frac{3\pi}{L}x\right)\right) \cdot \sin\left(\frac{\pi}{H}y\right) \cdot \sin(\omega t) \quad \text{eq 5.26}$$

Where U_x and U_y are displacements in the X and Y directions (m), A and B are geometrical functions, and C is the wave speed as it differs for different materials (m/s). These two equations represent the deformation that occurs on a 2-D sheet based on the X and Y location on the sheet and time (t).

A modal analysis is conducted to obtain the resonance frequency of the piezo element in Figure 5.11. A total of three models are built, and their dimensions are $20 \times 9 \times 2$ mm, $13 \times 6 \times 2$ mm, and $7 \times 3 \times 1$ mm. These values are chosen as dimensions closer to $L \times H (0.5L) \times t$ format tend to have a higher chance of creating E (k,l) waves. The plate is kept small due to size restrictions as this is an implanted system.

The first 100 modes of resonance are set to be extracted. The total number of elements used is around 140,000 elements per model. As seen in Figure 5.11, this is considered a high-density mesh that is more than sufficient for the geometry at hand. The piezoceramic material used is PZT-5H, as it has a better piezoelectric coefficient (strain matrix) and dielectric property (permittivity) compared to other piezoceramics such as PZT-5A and PZT-5J. Its only shortcoming is that it does not perform well in high temperatures and is influenced by temperature changes. This is of no consequence under the current operating conditions for which the device is intended. PZT-5H properties are shown in Table 5.7.

Table 5.7: PZT-5H properties

Density (Kg/m ³)	7500								
Electrical Permittivity (orthotropic) (F/m)	d11	d22	d33						
	1.51E-08	1.51E-08	1.30E-08						
Piezoelectric strain matrix (m/V)	d113	d223	d311	d322	d333				
	7.41E-10	7.41E-10	-2.74E-10	-2.74E-10	5.93E-10				
Elasticity (constants) (N/m ²)	E1	E2	E3	Nu12	Nu13	Nu23	G12	G13	G23
	6.06E+10	6.06E+10	4.83E+10	0.289	0.512	0.512	2.35E+10	2.3E+10	2.3E+10

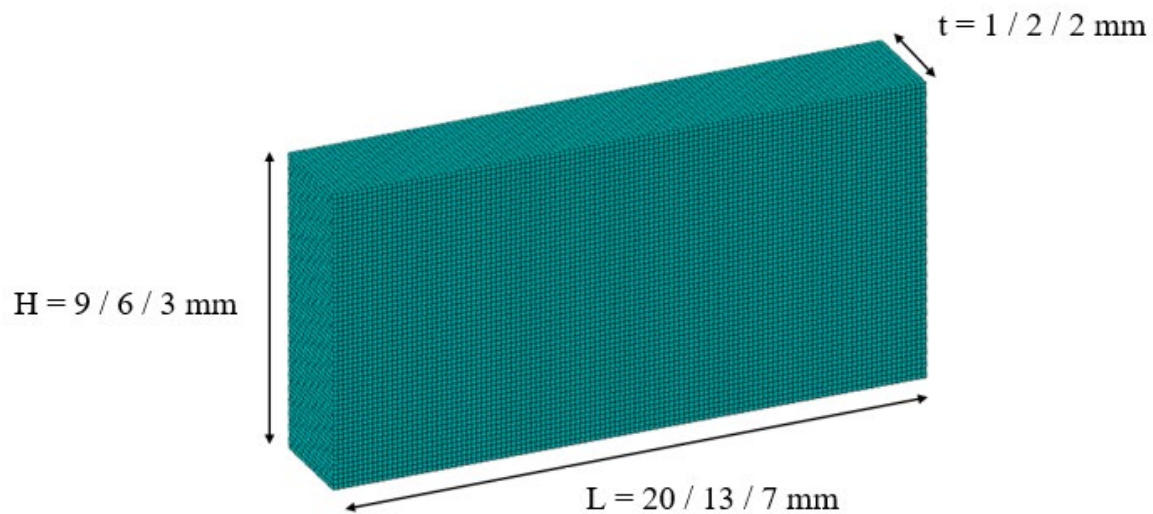
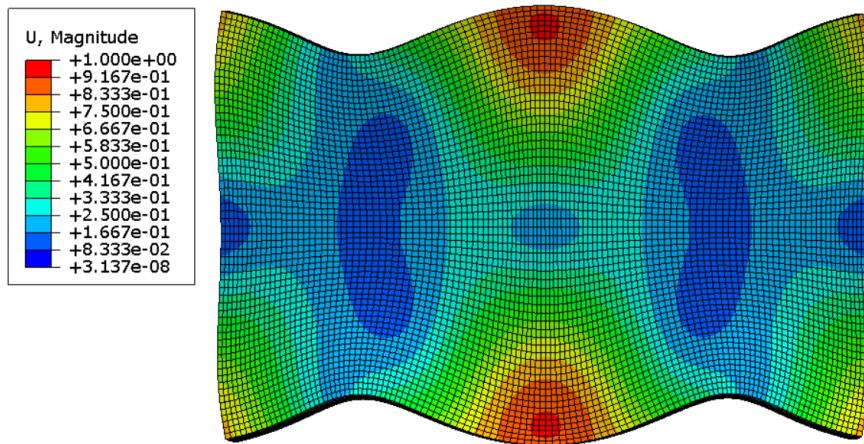


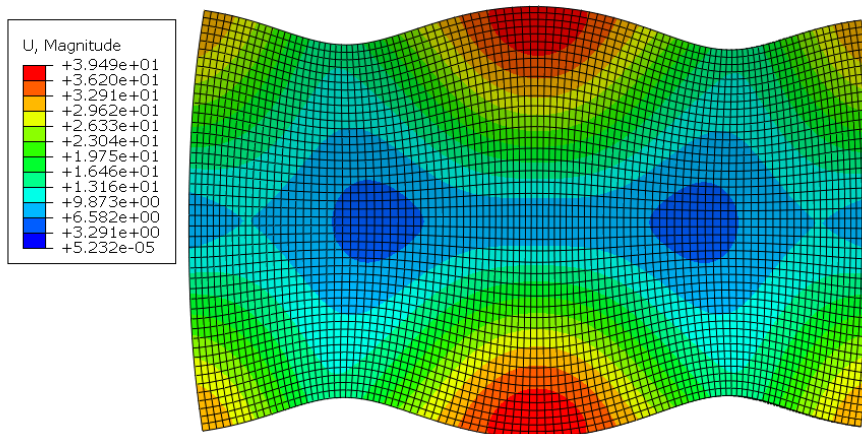
Figure 5.11: Piezoceramic frequency analysis model

For the $13 \times 6 \times 2$ mm piezoelectric sheet, the E (3,1) mode occurs at 294.8 kHz. The $20 \times 9 \times 2$ sheet model exhibits an E (3,1) mode at 178 kHz. Figure 5.12 shows the deformation associated with those resonance frequencies. The figure showcases the symmetry in deformation in both the X- and Y-axis. This can only be achieved by two pairs of standing waves that are equal in frequency but opposite in direction on each of the two axes. No E (3,1) mode is identified for the results of the $7 \times 3 \times 1$ mm. Up to 200 resonance modes – some of which are available in Appendix-7 – are extracted for this sheet size. This is expected since as the plate gets smaller in size, higher frequencies are required to activate the E (3,1) resonance modes until they reach a size where those waves cannot be created anymore. This points out that there are size constraints when it comes to generating E (3,1) modes. Thus, no results for the $7 \times 3 \times 1$ model are presented. As this is a frequency analysis, the displacement values shown in the figures are not real.

Due to its smaller size, the $13 \times 6 \times 2$ mm model is selected to actuate the valve. This size is expected to result in a step definition – which is the resulting displacement per voltage cycle – that is much higher than required. Furthermore, as the sheet's size increases, the E (3,1) resonance mode value decreases. This indicates that larger sheets are easier to control as they demand a lower frequency voltage supply to activate their E (3,1) mode. However, in this case, the difference between the two E (3,1) frequencies is not of a great magnitude. Hence, this difference does not outweigh the benefits of using a smaller piezoelectric element.



(a)



(b)

Figure 5.12: Piezoceramic sheet E (3,1) resonance mode results. (a) The $13 \times 6 \times 2$ mm piezoceramic sheet E (3,1) mode at a resonance frequency of 294.8 kHz. (b) The $20 \times 9 \times 2$ mm piezoceramic sheet E (3,1) mode at a resonance frequency of 178 kHz

5.4.3 Dynamic Analysis

After confirming the E (3,1) mode frequency, the next step is to simulate the piezoelectric element's operation through partial excitation. As shown above in Figure 5.9, two electrodes supply voltage to the piezoelectric element. A high-frequency current must be simulated through the piezo element to visualise the resulting reaction.

A tip that is to be in contact with the stator – shown in Figure 5.13 – is added at the top midpoint of the model. It is made of aluminium oxide, a material with a high friction coefficient to ensure good frictional contact. A sine wave voltage of 3.5 V is set as a boundary condition on half of the model face on the front side. The sine wave frequency is the E (3,1) mode extracted earlier, which is 294.8 kHz. The back side voltage is set to ground across the entire face. The total number of elements used is 60,000, which is also considered sufficient due to the simple geometry of the sheet. The properties used for PZT-5H and aluminium oxide are in Table 5.7 and Table 5.8, respectively. The time period on the dynamic simulation is $1.7E-5$ s as this is enough time for five voltage cycles ($5/f$) at 294.8 kHz.

Table 5.8: Aluminium oxide properties

Parameter	Value
Density (Kg/m ³)	3400
Young's Modulus (GPa)	320
Poisson's Ratio	0.23

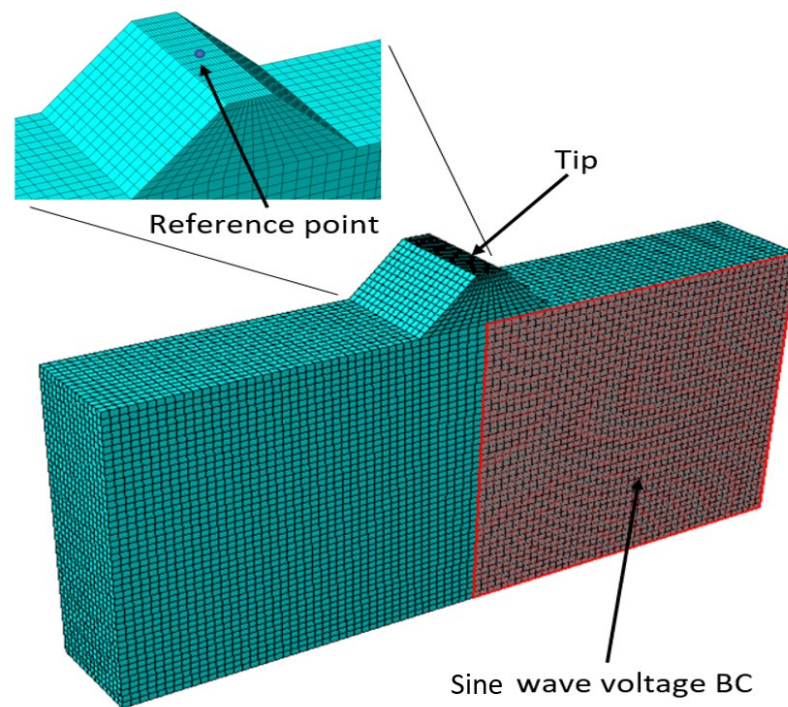


Figure 5.13: Piezo element partial excitation model. A sine wave voltage of 294.8 kHz is used as a boundary condition

The dynamic simulation was carried out for a period of $1.7E-5$ s, where the results of the sine wave voltage effects on the tip are shown in Figure 5.14. As the tip is thrust away from the piezo element, it also gains X-axis displacement. The tip goes through one cycle of movement per voltage cycle, where the changes in tip position during that cycle are classified into four positions. Stator movement is achieved through this cycle. First, the tip gains both Y-axis displacement and X-axis displacement. The Y-displacement causes the tip to clamp on the stator, while the X-displacement causes the tip to drag the stator along with it as a result of friction. Next, negative Y-displacement and X-displacement are gained. This causes the tip to unclamp and return to its initial position, thus completing a full cycle (step). Displacement data is retrieved from the reference point shown in Figure 5.13. The accurate method of measuring

the step size is through an experimental setup. However, data retrieved from the reference point can indicate the step size. Figure 5.15 demonstrates X and Y displacement on the tip. The dragging process occurs when the tip is on the positive side of both the X and Y axes. This indicates that the step size is around 4 nm. Since the simulation used a 294.8 kHz voltage input, the one-cycle time period – using $t = 1/f$ – is 3.4 μs . Using $v = \text{displacement} / t$, the velocity of the motor can be estimated to be around 1 mm/s. This means that the motor can go from one end of the pressure points range to the other – 2 mm distance – in 2 seconds. The overall properties of the ultrasonic motor design can be viewed in Table 5.9. The number of cycles required for the motor to set the spring at each individual pressure point is shown in Table 5.10.

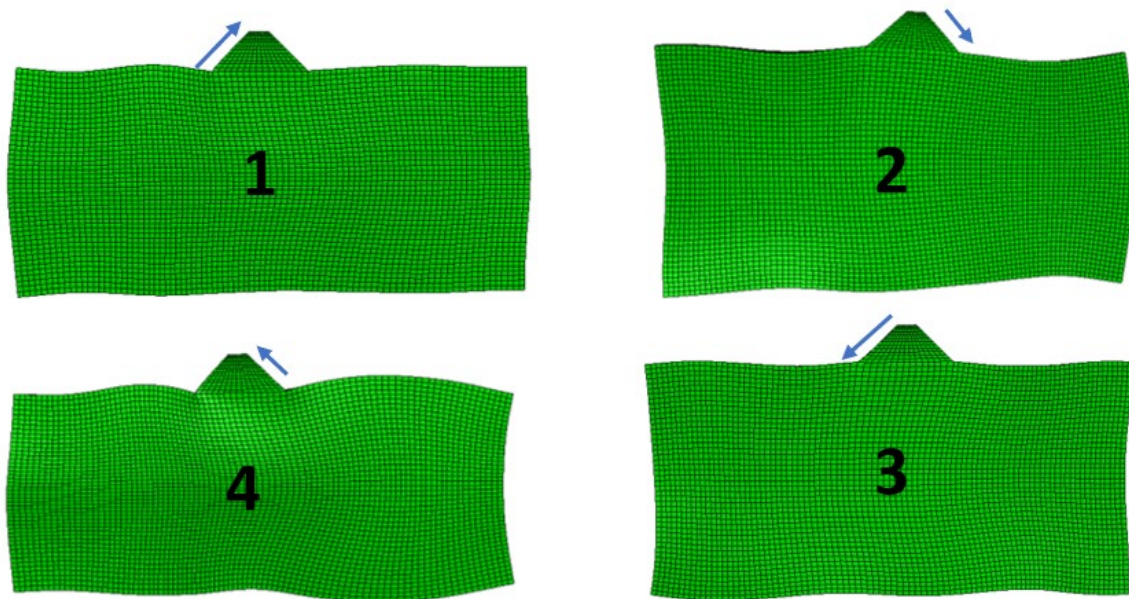


Figure 5.14: Ultrasonic motor one-cycle step. Arrows sizes indicate the direction and level of displacement

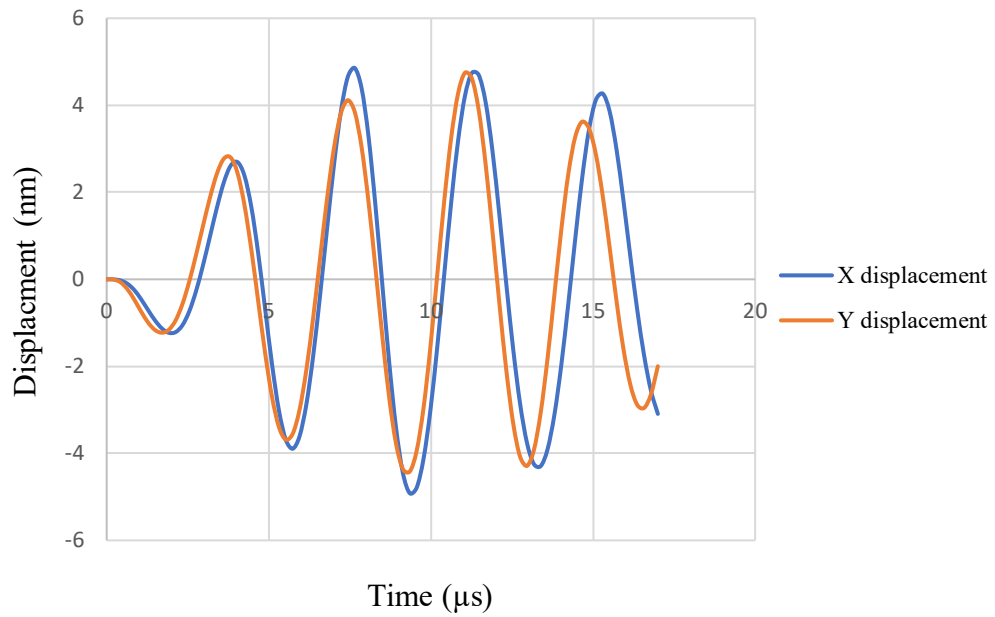


Figure 5.15: Ultrasonic element tip displacement. This is the X and Y displacement for the entire $1.7 \text{ E-}5 \text{ s}$

Table 5.9: Ultrasonic motor parameters

Parameter	Value	Parameter	Value
Material	PZT-5H / Aluminium Oxide tip	Voltage input	3.5 V at 294.8 KHz
Step definition	4 nm per voltage cycle	Velocity	1 mm/sec

Table 5.10: Required voltage cycles for the setup of each pressure point

ICP	Spring Length (mm)	Required voltage cycles	Spring Length (mm)	Required voltage cycles
20	3.33	4.22E+04	2	5.00E+05
19	3.39	3.83E+04	2.05	4.86E+05
18	3.45	3.42E+04	2.11	4.72E+05
17	3.52	3.02E+04	2.17	4.57E+05
16	3.58	2.61E+04	2.23	4.42E+05
15	3.65	2.19E+04	2.29	4.27E+05
14	3.72	1.77E+04	2.35	4.12E+05
13	3.79	1.34E+04	2.41	3.97E+05
12	3.86	9.02E+03	2.47	3.82E+05
11	3.93	4.56E+03	2.53	3.67E+05
10	4	initial position	2.6	3.51E+05

The lowest pressure point with the max length of spring is set as the default starting point (zero point) for these values. The number of cycles changes for a different zero point and also when the device is alternating between different pressure points.

5.5 Conclusion

The design concept of the electromechanical valve is derived in chapter four based on a number of factors. The concept consists of three components, which are the fluid compartment, the spring and ball system, and the piezoelectric ultrasonic motor. This chapter is concerned with these three components' detailed and in-depth design and sizing.

The first step was to conduct a computational fluid dynamics (CFD) analysis to understand the types of forces and flow under which the system is going to operate. Several models were simulated as the system is designed to handle flow at multiple pressure points. The results showed that at the maximum pressure point of 20 mmHg in the standing position, the maximum flow expected from the system is 300 mL/h. The flow resulting from the minimum pressure

point of 10 mmHg in the supine position is 42 mL/h. The dimension of the fluid compartment is shown in Figure 5.2b.

The second step was the design of the spring and ball mechanism that controls the system's open/close status. Some of the design parameters – mainly the forces the system operates under – were obtained from the previous CFD simulation. An initial design and sizing for the spring are derived using general design equations first. This was considered a starting point for the Finite element simulation as the model is built based on this initial design. The FEA simulation results confirmed the spring's parameters and dimensions. The resulting spring dimensions and properties are shown in Table 5.5. The spring has a free length of 4.22 mm, a wire diameter of 0.06 mm, and a mean diameter of 1.8 mm.

The last step was designing the piezoelectric motor that controls the spring length and tension. The ultrasonic motor system was selected in the previous chapter. The design process depends mainly on Finite Element Analysis (FEA). A modal analysis is carried out on three sizes of a PZT-5H sheet model. Two of the models proved to exhibit an E (3,1) resonance mode, while one sheet did not. This is assumed to be a result of the small size of the sheet. The $13 \times 6 \times 2$ mm model was selected as it is smaller in size, and its E (3,1) mode is not much higher than the other larger size sheet. The extracted E (3,1) mode for this sheet has a value of 294.8 KHz. Next, a dynamic analysis was conducted where a high-frequency voltage was applied to the model of the selected sheet. The resulting deformation showed how the model deforms in a way that generates displacement through friction, which is shown in Figure 5.17. The resulting ultrasonic motor has a step definition of 4 nm, a velocity of 1 mm/s, and can cover the entire range of pressure points in 2 seconds.

This detailed design process makes the presented layout the first in-depth concept and layout of an electromechanical valve that is active shunt compatible. The main point that is left

unaddressed is the issue of preloading the piezo motor, as this can only be measured experimentally. However, it is expected that minimum preloading is required as the motor works under minute forces. Hence, the preloading force effects on the piezo motor displacement are expected to be kept at a minimum.

Chapter 6

NPH GAIT ANALYSIS

6.1 Introduction

As mentioned in section 2.2.3, normal-pressure hydrocephalus (NPH) is unique as it develops due to the enlargement of the ventricles in the brain without an increased ICP. The main symptom of NPH is gait disorder, which physicians currently assess visually during the diagnosis process. The fact is that the diagnostic procedure of NPH is not always accurate and that both the gait assessment and the use of imaging to evaluate the size of the ventricles are fairly visual and do not rely on quantifiable data. Thus, this process is considered qualitative and subjective. The condition is not associated with elevated ICP, meaning that an active shunt pressure sensor is not an appropriate tool to monitor the patient's condition.

Using gait analysis systems can provide accurate patient gait monitoring data as momentum or angular patterns can be generated. However, their costs and space requirements are high as they use a combination of optical analysis of motion and force platforms [70,71]. Hence, they are impractical as a standard diagnosis practice. This is of special importance when considering that this process needs to be incorporated under the concept of active shunting. This points out that device mobility and the ability of the patient to conduct this process off-site and without the supervision of a physician is crucial. The patient must be able to produce data regularly for continuous monitoring of their condition. Hence, it is decided that a sensor-based wearable is the optimal device for this application.

This chapter proposes a wearable sensor to monitor the gait of NPH patients as it can indicate any further development in their condition. The wearable sensor is to be used for both diagnosis and monitoring purposes. The methodology followed consists of designing and manufacturing an accelerometer-based wearable printed circuit board (PCB) unit. In addition to the selection of necessary components, PCB design is also carried out. The PCB is coded through the use of a microcontroller to gather gait readings and transfer them via bluetooth to the designated computer for data collection and processing. The final version of the PCB utilises a small-size microcontroller, a 3-axis accelerometer, a 3.7 V battery, and a bluetooth module.

6.2 Wearable Device Design

The wearable device proposed is an accelerometer-based sensor as opposed to a gyroscope. This is a result of the fact that acceleration level output can be more useful than tilt measurements. Furthermore, using an accelerometer gives more freedom in selecting the location where the device is attached, as gyroscopes can only provide usable reading when attached to a joint. Regarding the location of the wearable, three locations are used for wearable sensors, which are the lower back, the chest, and the ankle [69]. However, for the purpose of using a wearable for NPH diagnosis, gait analysis and comparison are very important. The ankle is the point that can supply the most relevant data as it is the main point of motion, making it ideal as a sensor location. Shuffling severity, step size, and speed comparison can all be deduced from the output acceleration levels.

6.2.1 Device Components

The proposed device is an ankle-attached accelerometer-based PCB. The components of this PCB are a microcontroller that is coded based on the device function, a bluetooth module so data can be streamed to a nearby computer, an accelerometer that collects relevant data, and a battery that supplies power to all system components.

a. Attiny85 Microcontroller

The Attiny85 – Figure 6.1 – is an 8-bit AVR microcontroller that has an 8 KB programmable flash memory (EEPROM) and a RAM space of around 512 bytes. It has an operating voltage range from 1.5 to 5.5 V and a total of 8 pins with six programmable I/O lines [147]. As the microcontroller is to be operated under a frequency of 10 MHz, the minimum power requirement is between 2.7 and 5.5 V. The module has a 10-bit ADC logic converter to enable it to interface with sensors. The version used is the through-hole mount (THM), as this makes it simpler to disassemble the microcontroller from the PCB and reprogram it for calibration purposes.

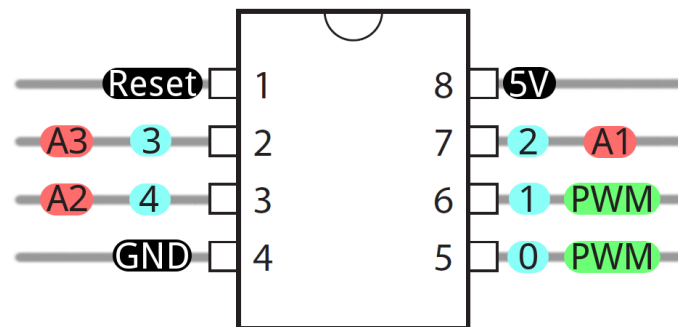


Figure 6.1: Attiny 85 microcontroller [147]

b. HC-05 Bluetooth Module

The HC-05 module – Figure 6.2 – is a fully qualified bluetooth V2.0 serial port protocol (SPP) module. In addition, the module supports enhanced data rate (EDR), increasing the data transfer bit rate to 3 Mbit/s with a 2.4 GHz radio transceiver and baseband. The module package size is a small 12.7×27 mm with a range of 10 meters and an operating voltage of 1.8 to 3.6 V. It also has a UART interface with a programmable baud rate ranging from 9600 to 460800 [148].

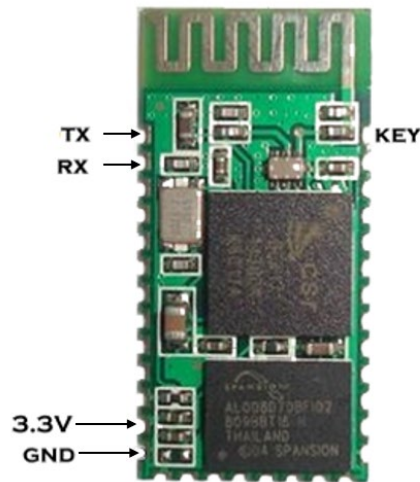


Figure 6.2: HC-05 bluetooth module [148]

c. ADXL335 Accelerometer

The ADXL335 – Figure 6.3 – is a low-power and small packaged ($4\text{mm} \times 4\text{mm} \times 1.45\text{mm}$) $\pm 3.7\text{ g}$ – using earth gravity acceleration of 9.81 m/s^2 as a reference point – 3-axis accelerometer with signal-conditioned voltage outputs. It can measure both acceleration of gravity changes due to static tilt and acceleration resulting from dynamic motion. This makes the sensor appropriate for use in tilt sensing, motion, vibration, and shock applications. The sensor output voltage changes based on the fluctuation of acceleration it undergoes. This change is then converted to g readings based on the sensor sensitivity. The sensor can operate at frequencies ranging from 0.5 Hz to 1600 Hz for both the X and Y-axis output and 0.5 Hz to 550 Hz for the Z-axis output. The 1600 Hz and 550 Hz are the maximum frequencies the sensor can output – for their respective axes – and are achievable by simply not using any external filters [149].

These frequencies can be set by linking each output with a capacitor. The accelerometer properties are shown in Table 6.1.

Table 6.1: ADXL335 accelerometer specifications

Property	Value
Range	± 3.7 g
Nonlinearity	$\pm 0.3\%$
Cross-axis sensitivity	$\pm 1\%$
Sensitivity at X, Y, and Z	≈ 300 mV/g
0 g Voltage at X, Y	≈ 1.5 V 1.6 used due to acc. offset
0 g Voltage at Z	≈ 1.5 V 1.64 used due to acc. offset
Current	350 μ A

It is important to note that the sensor has an operating voltage range of 1.8 V to 3.6 V. However, the sensor sensitivity is highly affected by the input voltage as the sensor output is ratio-metric. The values in this table are for voltage input of 3 V. Specifications were obtained from [149].

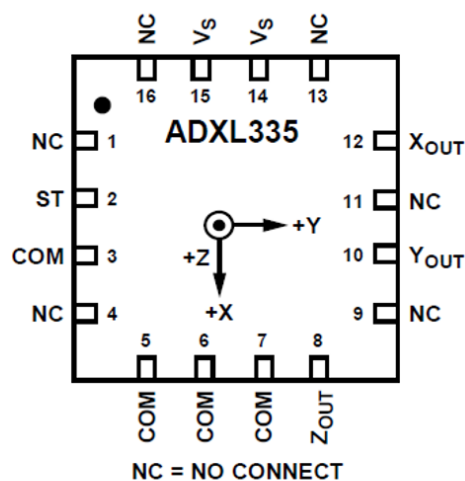


Figure 6.3: ADXL335 accelerometer layout [149]

d. Battery

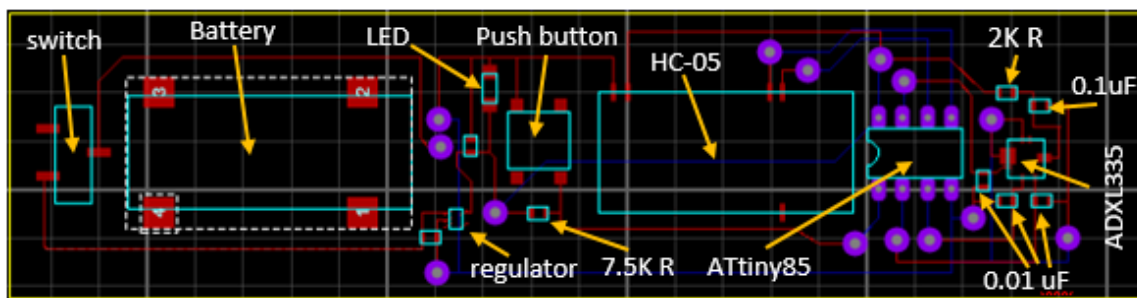
The battery used has a voltage of 3.7 V, a capacity of 150 mA, and a package size of 30mm × 12mm × 4.9mm. Although the battery has a fairly small capacity, its size is perfect for keeping the PCB small and compact. It must be noted that when the battery is fully charged, its output is increased to 4 V.

6.2.2 Circuit Description

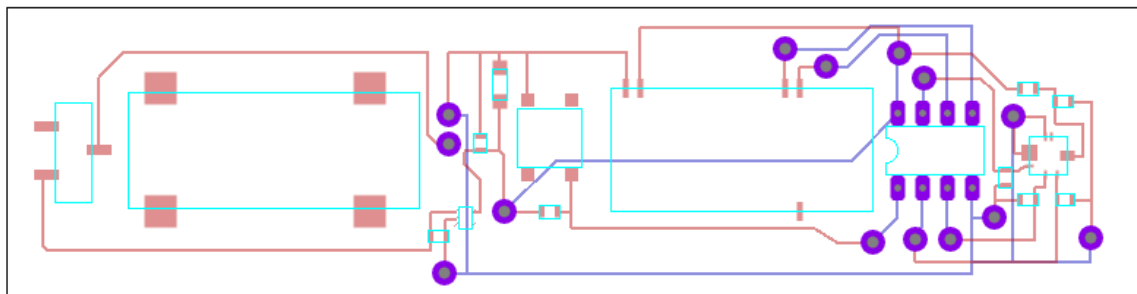
An RC passive low pass filtering is implemented for the accelerometer output in order to avoid the aliasing effect. This effect refers to signals being indistinguishable from each other when sampled. The RC low pass filtering offers a start and an endpoint for each signal when sampled from a continuous output. Since the ADXL335 accelerometer has a built-in 32 KΩ on all three outputs, it requires only a capacitor for each output to implement this filter. The capacitors are also necessary for controlling the output frequency. The equation below is used to determine the capacitance required for a specific frequency output [150].

$$F_c = \frac{1}{2\pi R C(X, Y, Z)} \quad \text{eq 6.1}$$

Where F_c is the cut-off frequency (Hz), R is the circuit resistance (32 KΩ), and C is the capacitance (F) that is required on each of the accelerometer X Y Z outputs. The max sampling rate in the studies reviewed was 100 Hz. As this device is an ankle attachment, a high sampling is required to reflect acceleration changes during each step accurately. Thus, a 500 Hz bandwidth with a 100 Hz sampling rate is chosen, which from eq 6.1 requires a 0.01 μF capacitor.



(a)



(b)

Figure 6.4: NPH gait device circuit layout. (a) Components placement within the printed circuit board (PCB). (b) Itching layout that connects different components to each other, where the red line showcases top-side connections and the blue line showcases backside connections. The accelerometer was mounted at the end of the PCB so it could be closer to the ankle, which is the main point of motion when the device is strapped to the leg

PROTEUS software is a package used to create electronic designs and schematics, which is used to create the circuit layout showcased in Figure 6.4. A $2\text{ K}\Omega$ resistor is connected with the input on the accelerometer chip to pull the voltage from 3.7 V to 3 V as it is more suited for calibrating the sensor output. A $0.1\text{ }\mu\text{F}$ capacitor is also used on the input side to make sure a stable charge is supplied. The accelerometer X, Y, and Z outputs are connected to A3, A2,

and A1 input pins on the microcontroller showcased in Figure 6.1, respectively. This is how the voltage values are supplied from the accelerometer to the microcontroller. These voltage values are then translated into acceleration values. Since each accelerometer output goes through a 0.01 μF capacitor, a 500 Hz bandwidth is achieved. The equation below shows the relation between the resistance and voltage drop.

$$R = \frac{(V_s - V_d)}{I} \quad \text{eq 6.2}$$

Where R is the resistor resistance (Ω), V_s is the supply voltage (V), V_d is the voltage drop (V), and I is the current (amp). A 3.7 V voltage regulator is added to the circuit as well due to the issue that when the battery is fully charged, its voltage increases to 4 V. This does not pose an issue to the electrical components but can interfere with accelerometer output as it is calibrated for an input of 3.7 V. Output pins 5 and 6 on the microcontroller – Figure 6.1 – are connected to the Rx/Tx pins on the HC-05 module showcased in Figure 6.2. Other components used consist of a slide switch, LED light, push-button, and a 7.5 K Ω pull-up resistor for the reset pin of the microcontroller.

6.3 Wearable Device Assembly

The first step before assembling the device is ensuring that the design, selected components, and circuit layout are suitable and appropriate for controlling the accelerometer. This is achieved through a prototype version – showcased in Figure 6.5 – of the device, where a through-hole-mounted (THM) versions of the components listed in section 6.2.1 are used. The components were mounted on a prototyping breadboard, and necessary connections between different components were established using soldering lines throughout the breadboard.

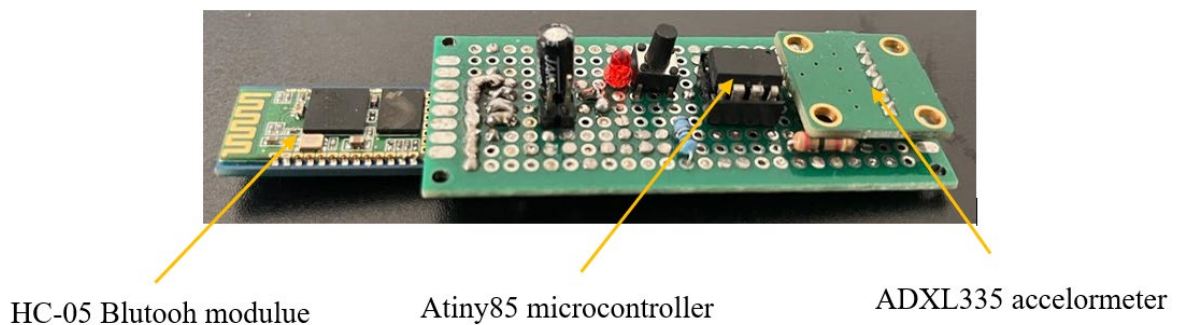


Figure 6.5: Initial prototype of the wearable sensor

The prototype was also used to test the code used on the microcontroller, as it required calibration. Any issues or mistakes with the code were sorted during this process. The initial calibration was conducted through a “static gravity” test, which is carried out by tilting the prototype on each one of its axes. The output voltage for the axis parallel to the gravity direction was noted and correlated to a 1 g reading (acceleration due to static gravity). In contrast, the output at the other two axes represented the voltage output at 0 g.

After the breadboard prototype was confirmed to be in working order in terms of the components, the connection, and the code, the PCB manufacturing step was undertaken. The schematics of the PCB shown in Figure 6.4 were produced using PROTEUS software. The manufacturing process is conducted using a VOLTERA – showcased in Figure 6.6 – printing machine, where the generated schematics of the PCB are supplied to the machine. As the machine is printing-based, copper is added to the wafer to generate the connection tracks rather than being etched. Since the PCB is double-sided, tracks on both faces are printed. The resulting PCB is showcased in Figure 6.7.

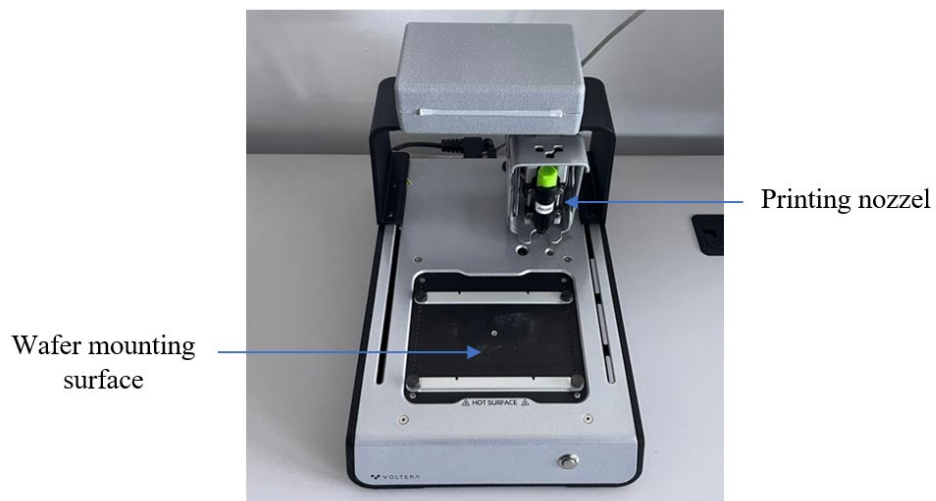
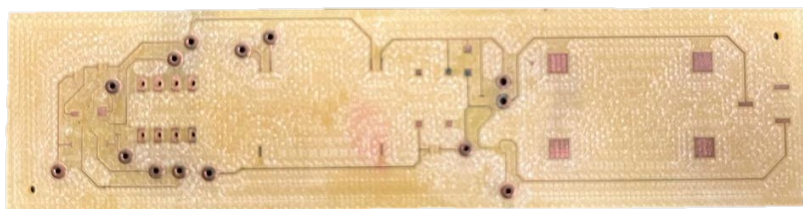
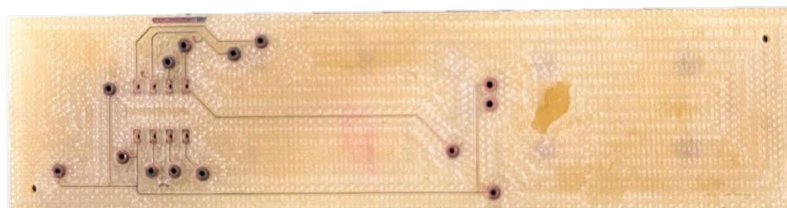


Figure 6.6: VOLTERA PCB printing machine. The wafer is placed on the mounting surface while the printing nozzle supplies cooper onto it



(a)



(b)

Figure 6.7: The printed PCB. (a) The top side of the wafer. (b) the bottom side of the wafer. The connection between the two sides was established by inserting copper rods through the connection holes

The different components of the PCB were then added by applying chemical liquid soldering paste on the connection points. The components are then carefully placed on these connection points. The PCB is then placed in a surface oven, where it is baked at 90 °C for about two hours. The purpose of this process is to evaporate all the moisture in the PCB in order to solidify the liquid solder.

Housing for the PCB is then designed and 3-D printed out of plastic to ensure that the device weight is kept at a minimum. The final product is showcased in Figure 6.8 as it is $12.5 \times 3.5 \times 1.8$ cm in terms of dimensions and has a weight of 35 g. Straps were added to the PCB housing to keep the PCB secure when it is attached to the patient's ankle. The entire manufacturing process was carried out in-house at LJMU labs.

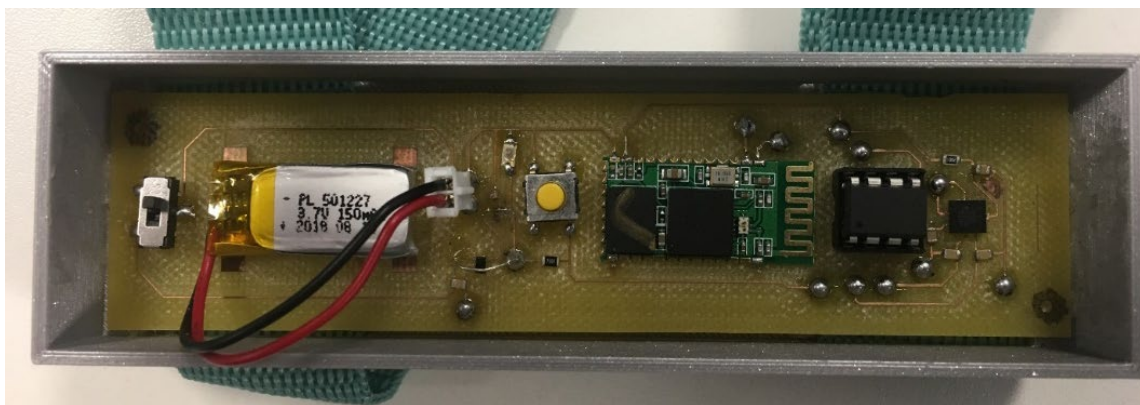


Figure 6.8: Completed version of the wearable accelerometer-based sensor

6.4 Wearable Device Programming

Although C language is normally used, the coding language used on the PCB microcontroller is C++. The microcontroller's programming was carried out using Arduino IDE, and hence, an Arduino was used as a programming platform. This was used as an alternative to AVRISP – a platform that is used to program AVR microcontrollers – as it is simpler and was already used during the prototyping of the PCB.

The microcontroller was programmed using a breadboard to establish the necessary connections to the Arduino. This is the main reason why a THM version of the Attiny85 was used since detaching it from the PCB is simpler compared to the surface mount type. This was of great importance as the device went through several calibration procedures that required the C++ code to be modified.

The accelerometer data sheet states that 0 g output is correlated to an output voltage of 1.5 V for all three axes. However, due to accelerometer bias (offset), the device was manually calibrated through a “static gravity” test mentioned in section 6.3. Based on the test results, initial calibration values – shown in Table 6.1 – were noted and used to program the wearable device instead of the default values. On the other end, python was used to connect the PC with the PCB to extract and plot the acceleration data. Figure 6.9 showcases the flowchart of the data-gathering process for both the PCB end and the computer end.

Codes for both the PCB and computer ends are shown in Appendices-8 and -9, respectively. It is important to note that the codes for the PCB and the computer – where Python was used – are written and must be initiated separately. This translates to the fact that after the wearable device is switched on, the code on the computer needs to be started manually to receive and plot the data.

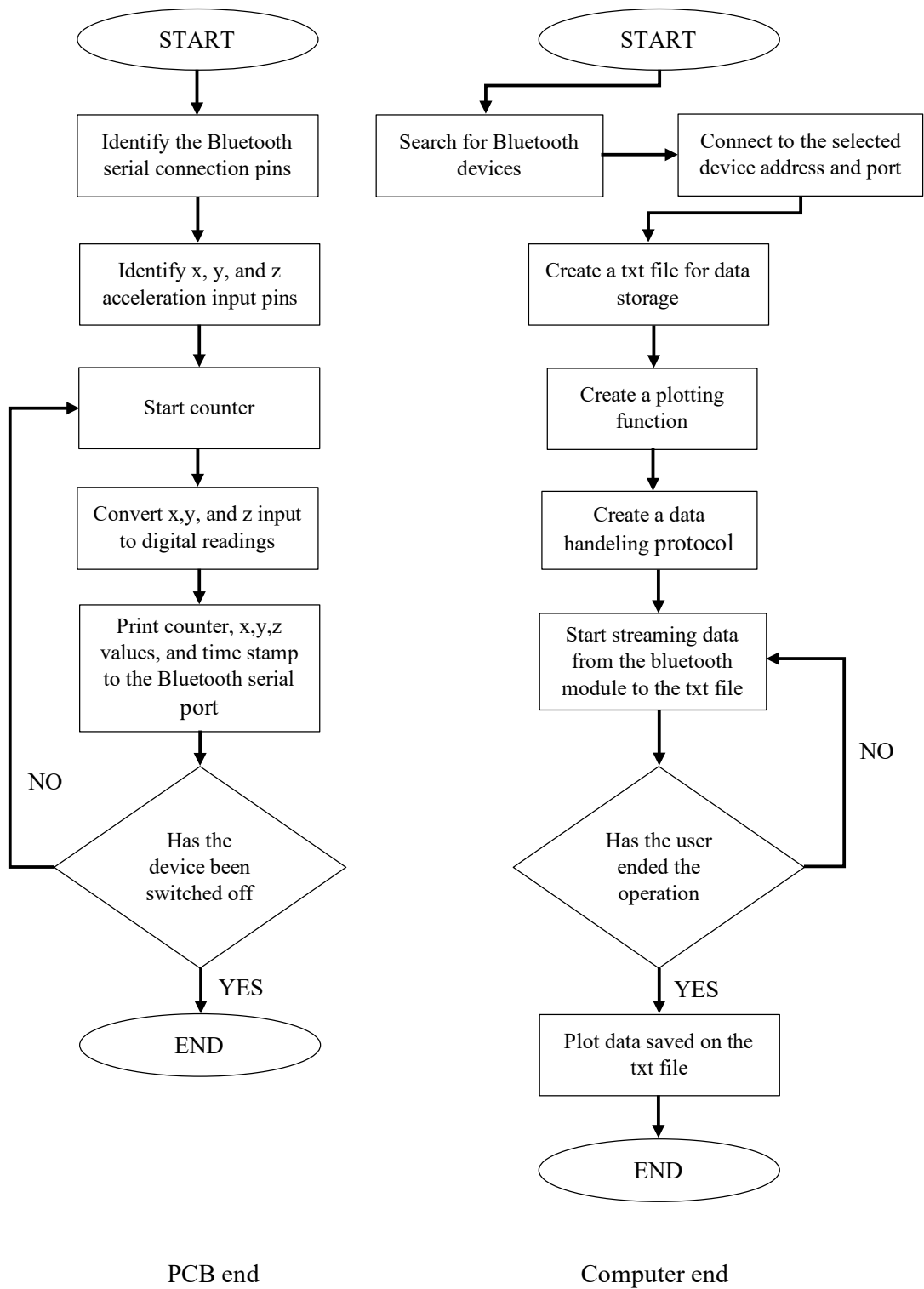


Figure 6.9: PCB acceleration data gathering flowchart

6.5 Conclusion

The key feature of NPH is that it is not associated with an increase in ICP pressure. As a result, the hakim-triad group of symptoms – the main symptom being the gait disorder – is used to diagnose and monitor the development of the patient's condition. This proposes a challenge as the active shunting system is unable to monitor this condition by only using the pressure sensor input. As gait disorder is the most common symptom of the hakim-triad, a wearable device was proposed to monitor it for both diagnosis and monitoring purposes. Currently, the physician analyses gait visually during the gait test without the input of any quantitative data. The choice to use a wearable ankle-attached accelerometer-based wearable device for gait analysis was made as it is the most practical option out of the available methods. Most importantly, it offers mobility and can be used by the patient at home to provide data on a regular basis.

The device mainly consists of a small microcontroller, a 3-axis 3.7 g accelerometer, a bluetooth module, and a 3.7 V battery. The choice to use an accelerometer over a gyroscope was made as the accelerometer can provide a more usable type of data and would result in fewer restrictions regarding the placement of the wearable device. The microcontroller is programmed using C++ to send accelerometer readings through the bluetooth module to a nearby computer. A Python script on the computer handles oncoming real-time data and provides a graph of measured readings. An initial prototype was assembled to ensure the operation of the wearable components and to calibrate the code used on the microcontroller. The device was manufactured by utilising a PCB printing machine, where copper tracks were printed on a wafer to print the tracks needed for the PCB to function. The components were then attached to their connection points on the wafer by using liquid solder. The resulting wearable device is $12.5 \times 3.5 \times 1.8$ cm and weighs around 35 g.

Chapter 7

VALIDATION AND EVALUATION

7.1 Introduction

This chapter presents the validation and performance evaluation of the designed electromechanical valve and the developed wearable NPH gait device. The validation of the electromechanical valve is carried out through the verification of the data produced from the structural and fluid dynamic simulations conducted in chapter five. In terms of performance evaluation, comparisons between the designed valve and current systems – both currently used shunts and systems proposed in literature – are carried out.

Validation is achieved for the wearable gait device by carrying out a vibrational analysis test. This test showcased the functionality and accuracy of the device and was used to properly calibrate it, as the static gravity test – mentioned in section 6.3 – used to calibrate the device initially was not the ideal method. This functional experimental test is used to ensure that the device is operating as designed. For the evaluation process, comparisons between the developed device and the other devices available in the literature are also carried out.

The validation process showcases that the parameters of the different components of the designed electromechanical valve are accurate. The developed NPH wearable sensor is proven to produce accurate acceleration data. Performance evaluation of both devices showcases their prospective advantages and disadvantages compared with other devices.

7.2 The Electromechanical Valve

The designed valve validation process is conducted by verifying the produced data during fluid and structural simulations. The validation process is not for the entire valve but rather for the individual components designed in chapter 5. The validation of the flow compartment simulation, the spring structural analysis, and the piezoelectric element design are carried out separately. Evaluation of the valve is conducted through comparisons between the design and the valves available in the literature showcased in section 2.3.2. Mathematical modelling is also carried out to assess the electromechanical shunt performance in comparison with passive and fully automated valves.

7.2.1. Valve Validation

The first step is to verify the computational fluid dynamics results used to understand the flow in the flow compartment. Usually, the process of validating CFD results includes comparing them to other similar studies and simulations using absolute values. It can also be conducted using experimental results as a reference point. However, since neither is available for the CFD simulation conducted, the second-best option is verifying that the simulations have produced accurate results. This is achieved by carrying out a mesh independence analysis. This is not a full validation, but it can assist in evaluating the accuracy of the simulation conducted.

Mesh independence means that the simulation mesh (cells) has reached a point where it will yield the same or very similar results even if a finer mesh is used. To this end, nine simulations were conducted for the same pressure point using the same settings and only increasing the number of cells in each iteration. The pressure point used for this validation is 20 mmHg at the supine position. A total of nine points (simulations) are used to produce Figure 7.1. At first, the output values (force on the ball) change significantly with the increase in mesh size. This is because the mesh is still too coarse to yield accurate results at that point. However, at the point

of 50,000 cells and onward, the profile starts to flatten. This indicates that the simulation is reaching a mesh independence status.

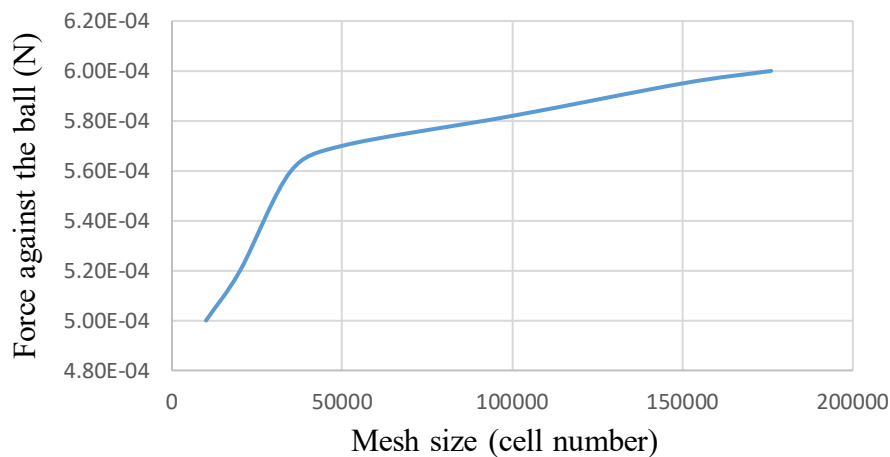


Figure 7.1: CFD simulation mesh independence chart. The pressure point used is 20 mmHg at the supine position. The minimum number of cells used is 10,000, and the maximum number used is 176,000

The last two simulations used a cell count of 150,000 and 176,000, yielding 5.95 and 6 E-4 N force outputs, respectively. This is an insignificant difference of 0.8% between the two outputs, so it was concluded that mesh independence was achieved at 176,000 cells. Table 7.1 showcases the resulting forces from the first simulation with the minimum cell count and the last two simulations conducted.

Table 7.1: CFD mesh independence analysis force output

Simulation No.	Cell count	Force output (E-4 N)	Error
1st	10,000	4.98	16%
8th	150,000	5.95	0.8%
9th	176,000	6	<0.8%

The next step is the validation of the results obtained from the structural simulation during the spring design step. This is achieved by checking the reaction forces (RF) resulting from the displacement applied during simulation. These RFs should be equal to the forces resulting from the pressure points in Table 5.3 or F_{max} and F_{min} in Table 5.4. This means that the reaction forces should be equal to the forces correlating to the displacement applied in the simulation. The reaction forces during maximum and minimum pressure in both the supine and flat conditions are obtained from simulations. The RFs are obtained at the fixed boundary condition – Figure 5.6 – and are measured as shown in Table 7.2. The measured reaction forces are equal to the previously calculated values in Table 5.3, thus validating the spring's dimensions.

Table 7.2: FEA measured reaction forces (RFs)

ICP	Supine position	Reaction force (E-3 N)	Standing position	Reaction force (E-3 N)
20		0.58		1.46
10		0.13		1.06

A mesh independence analysis is carried out to ensure that the number of cells and mesh used during the structural analysis is sufficient and that the results obtained from the simulations are accurate. A total of eight points (simulations) are used to produce Figure 7.2. These eight simulations were run at maximum loading conditions of 20 mmHg. As can be seen at first, the output values (von-mises stress) change significantly with the increase in mesh size as the mesh is too coarse to yield accurate results. However, at 70,000 cells and onward, the profile starts to flatten, indicating that the simulation is reaching a mesh independence status.

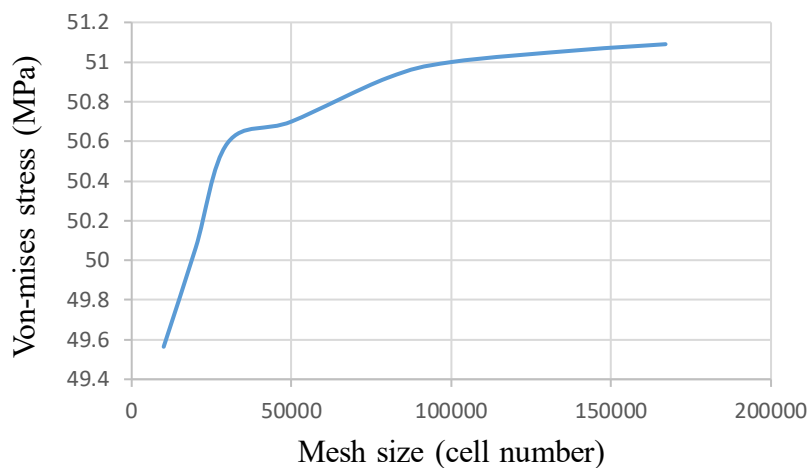


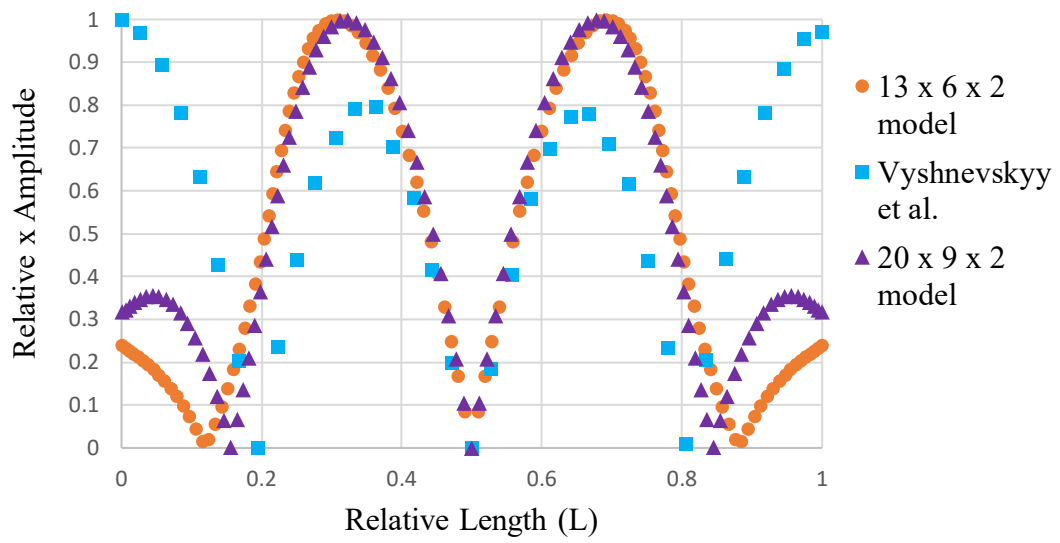
Figure 7.2: FEA simulation mesh independence chart. The spring condition used was at maximum conditions of 20 mmHg, corresponding to a 2.22 mm displacement. The minimum number of cells used was around 10,500, while the maximum was 167,000

The last two simulations used a cell count of 140,000 and 167,000. The resulting von-mises stress for both simulations is force outputs of 51.06 and 51.09 MPa, respectively. This is a difference of 0.05%, so it was concluded that mesh independence was achieved at 167,000 cells. Table 7.3 showcases the force output from the first and last two simulations.

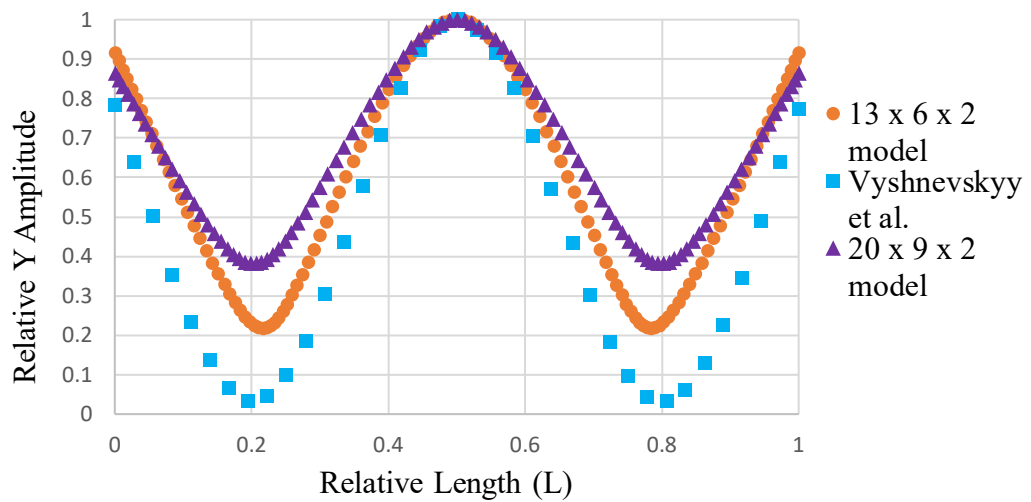
Table 7.3: FEA mesh independence analysis force output

Simulation No.	Cell count	Force output (MPa)	Error
1st	10,500	49.5	3%
7th	140,000	51.06	0.06%
8th	167,000	51.09	<0.06%

The last step is the validation of the ultrasonic element design and parameters. This is achieved through the validation of the E (3,1) mode showcased in Figure 5.12. During the design process, it was assumed that the piezoelectric element exhibits an E (3,1) excitation mode when deformation is mirrored on both major axes of the piezoelectric sheet. Since the frequency analysis produces relative displacement values that are not real, they can be compared to other simulation displacement results. Hence, the produced results are compared with those of Vyshnevskyy et al. [146]. This was carried out for the $13 \times 6 \times 2$ mm and the $20 \times 9 \times 2$ mm sheets under 294.8 kHz and 178 kHz excitation, respectively. Figure 7.3 shows relative displacement on the top plane of the piezoceramic element – Figure 5.11 – at $t/2$, where the X and Y relative displacement (amplitude) is compared with Vyshnevskyy et al. [146] results. Note that although the three sets of points – Figure 5.15a – are not an exact match for X amplitude, their profiles are the same. This is the same case when it comes to the Y amplitude seen in Figure 5.15b, where the two sets of points also do not exactly match but have the same profile. This is most likely a result of the difference in size between the piezoceramic sheets as Vyshnevskyy et al. [146] sheet size was $60 \times 9 \times 30$ mm, which is much larger than the sheets used in this study. The symmetry in both the X and Y amplitudes around the middle section of the sheet ($L/2$) is very clear in all profiles. This validates that the two piezoelectric elements do exhibit E (3,1) modes under the specified frequencies.



(a)



(b)

Figure 7.3: Piezoceramic sheet deformation results. The data taken from Vyshnevskyy et al. [146] is experimental and not from a simulation. (a) Relative X amplitude. (b) relative Y amplitude

7.2.2. Valve Evaluation

Mathematical modelling for both fully automated and passive valves was carried out in chapter four. It showed how each of these valves has its prospective advantages and disadvantages. Another mathematical simulation is carried out for the proposed electromechanical valve to showcase its advantages over the fully automated and passive valves. The Simulink simulation layout showcased in Figure 4.1 with the parameters in Table 4.1 are used again. However, the blocks representing the controlled and passive valves are replaced with a block representing the electromechanical valve. This block is showcased in Figure 7.4, as it takes into consideration both the ultrasonic motor and the passive ball-in-cone systems.

CSF volume drained by the ball-in-cone system is the same as outlined by eq 4.8, where CSF is only drained when the pressure difference at the inlet of the valve exceeds the designated valve opening pressure (OP). This OP is not fixed in the electromechanical valve, as the ultrasonic motor controls it. It changes with the change in hydrostatic pressure to ensure over-drainage does not occur. The motor controls the OP, as shown by the following equation:

$$OP(t) = \begin{cases} P_{setting} - P_{distal} & , P_{hydrostatic} \leq 0 \\ P_{setting} - P_{distal} + P_{hydrostatic}(t) & , P_{hydrostatic} \geq 0 \end{cases} \quad \text{eq 7.1}$$

Where $P_{setting}$ is the pressure that ICP must be kept at (mmHg). In the simulation conducted, the valve was set to keep ICP at 15 mmHg. The rest of the parameters and ICP simulation blocks are obtained from Table 4.1 and Figure 4.1.

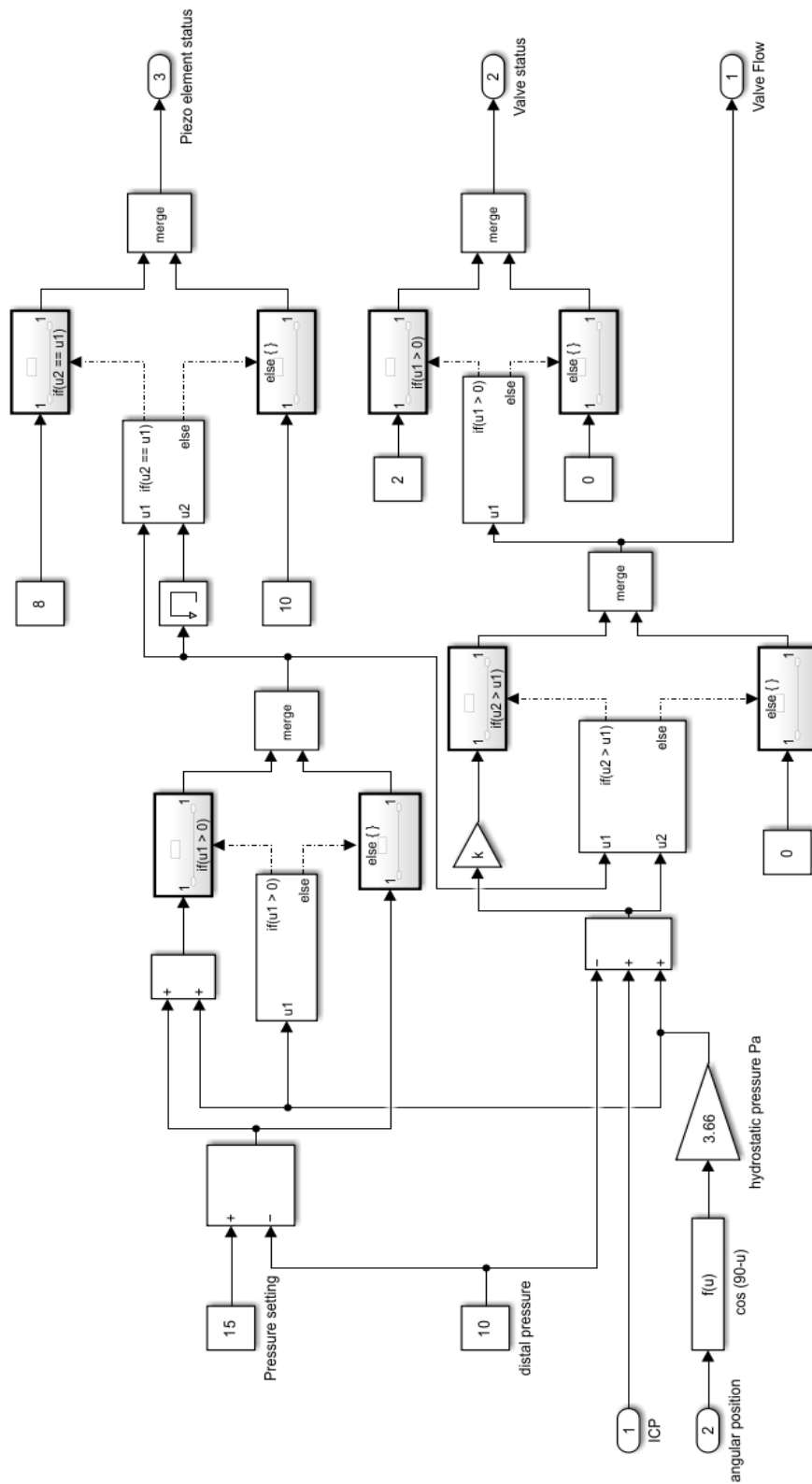


Figure 7.4: The electromechanical valve simulation block. Both the passive valve status and the ultrasonic motor status are available as outputs

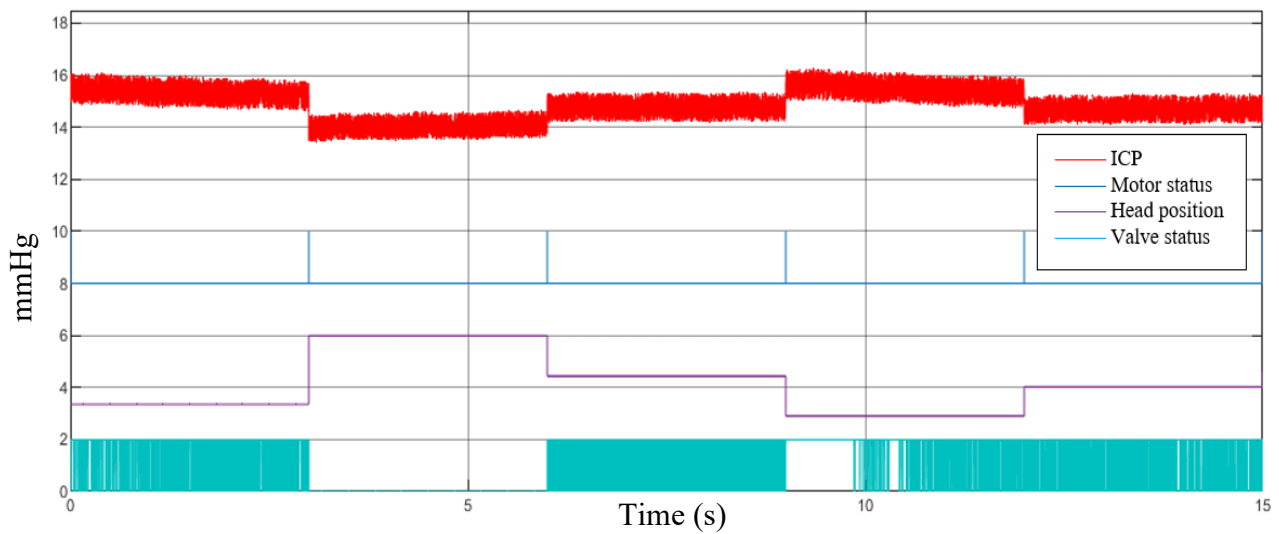


Figure 7.5: Electromechanical valve dynamic modelling results. It shows both the passive valve status and the ultrasonic motor status

The modelling results of the electromechanical valve seen in Figure 7.5 above show the nature of the resulting ICP signal. The smooth signal is a direct result of the continuous operation – as discussed in section 4.2.3 – of the passive side of the valve. The electromechanical valve goes through 427 open/close cycles, making it ten times more active than the fully automated valves – with 41 open/close cycles – and about three times more active than the passive – with 132 open/close cycles – valves. Furthermore, ICP is minimally affected by the hydrostatic pressure resulting from changes in the patient's head position, as ICP is still kept within the 15 mmHg limit. This is the result of the motor's interference as it changes the OP of the valve to accommodate the increased pressure. This is achieved with minimal activation of the ultrasonic element, keeping power draw to a minimum. To summarise, the results showcase how the electromechanical valve makes use of the standard valve's active response and the fully automated valve's controllability while negating the issues of hydrostatic pressure effects, power draw, and low activeness associated with both types of valves.

Different aspects of the electromechanical valve must be considered when its evaluation is conducted. These aspects include how the valve manages both the fundamental and operational challenges facing the current passive valve discussed in section 2.2.2. To this end, the valve operation must be weighed against both passive valves and new types of valves found in literature in terms of how they manage these issues, as showcased below.

a. Malfunctions Detection

Of the valves reviewed, only the electromechanical and Webster et al. [27] shunts offer the feature of malfunction detection. Webster et al. [27] STB shunt offers the option to detect only blockage occurring within the valve as it does not support the detection of any other types of faults, such as disconnections or catheter migration. Furthermore, for this detection process to be carried out, the patient must undergo an ultrasound scan as the valve STB shell deformation – which indicates the status of the valve – can only be seen through ultrasound imaging. On the other hand, the electromechanical valve can keep track of fault status without the need for external intervention or machinery. The system makes use of multiple sensory inputs – such as ICP and accelerometer sensors – to monitor and detect malfunctions within the shunt. In addition, the patient feedback is considered as reports of any unexpected symptoms or issues can be made through the mobile app linked to the shunt implanted system. The main advantage of the electromechanical shunt detection method over Webster et al. [27] is that it can offer constant monitoring of the shunt status without the need for an external process such as an ultrasound scan.

b. Blockage Management

Chung et al. [25] produced the only shunt design that is capable of managing or clearing blockage. The issue with blockage management is that 60 % of it occurs in the proximal catheter. As the proximal catheter is connected to the cranial cavity, any flushing motion in

an attempt to clear the blockage can interfere with the brain hydrodynamics. For this exact reason, Chung et al. [25] attempt to create this flushing motion on all parts of the shunt except for the proximal catheter, as his design includes a silicon check valve to make sure this motion does not reach the brain. The electromechanical valve does not offer any solution regarding the blockage management issue, as all possible solutions reviewed were deemed disadvantageous.

c. Siphoning Management

Managing hydrostatic pressure is a feature that the majority of the systems reviewed offer. The passive shunts navigate the issue through the use of gravitational valves, which can alter the valve OP based on the patient's position. The issue is that due to their nature, these valves can cause under-drainage as they need to be precisely implanted since any change or rotation in their positions can change their pressure setting. Johansson et al. [13] design offers siphoning management through the use of a third catheter to compensate for that excess hydrostatic pressure. In addition to the larger footprint caused by the third catheter, this system also has reverse flow issues. Chappel's [26] solution to this issue is to ensure a constant outflow of CSF regardless of ICP pressure or the effects of hydrostatic pressure. The issue with this design is that it focuses on constant flow rather than ICP management. Miniature shunts [28–30,32] do not face the hydrostatic pressure issue as these valves are implanted directly above the brain without the need for catheters. The electromechanical valve utilises accelerometer feedback to change the system OP based on the patient's position. The miniature valves are more suited for combating this issue because they circumvent it entirely.

d. Events Recognition

The electromechanical valve is the only option equipped with the hardware needed to identify sneezing and coughing events. When the system identifies these events, the valve can be temporarily locked to ensure no unnecessary drainage can take place. Chappel's [26] device does not recognize events, but it does not permit them to cause over-drainage as its operation method provides a constant CSF flow.

e. Ranged Pressure Settings

The only two devices that offer ranged pressure settings are the electromechanical shunt and the passive – the programable – valves. However, while the passive valves require pressure setting revisions to be made on-site using specific magnetic tools, the electromechanical shunt can utilise its actuator and internet connection to achieve the same results without the need for a hospital visit.

Table 7.4 showcases those comparisons between these valves and the electromechanical valve. It is clear that the main drawback of the electromechanical valve is its inability to manage blockage issues. This was discussed in section 4.3.2, as introducing a micro pump to the electromechanical system is the only method that can resolve this issue. However, it was decided that the issues associated with the use of a pump outweigh the benefits. Of the five main features showcased in Table 7.4, the electromechanical shunt possesses four of them. Unexpectedly, the next best performance – in addition to the Chappel [26] valve – is for the passive classical shunts currently in use. Another possible drawback of the electromechanical shunt – not included in Table 7.4 – is its cost. A single passive shunt ranges between £1100 and £2300 [14–16]. The cost of a single electromechanical valve is estimated at around £1755, as shown in Appendix-11. However, additional costs are associated with the overall system of the electromechanical shunt, such as database setup and sensors. It is obvious that the startup

costs of the electromechanical shunt system are higher than those of other systems. However, the operating costs are lower because this system does not require pressure settings revisions to be made onsite in the clinic.

It can be summarised that the electromechanical shunt has a better performance than current passive shunts and those proposed in the literature. The proposed shunt covers five out of the six main features associated with the challenges that face hydrocephalus shunting. The fact that current passive shunts deliver the second-best performance further shows the stagnation in innovation associated with HC shunts.

Table 7.4: Performance evaluation of the electromechanical valve. The evaluation revolves around how the electromechanical valve manages certain issues compared with other valves

Features	Shunts	Electromechanical shunt	Passive shunts	Chung et al. [25]	Johansson et al. [13]	Chappel [26]	Webster et al. [27]	Miniature shunts [28–30,32]	Comments
Malfunctions detection		✓	✗	✗	✗	✗	✓	✗	Webster et al. [27] shunt only detects blockage malfunction, while the electromechanical shunt can detect other types of malfunctions.
Blockage management		✗	✗	✓	✗	✗	✗	✗	Blockage management proposed by Chung et al. [25] is manual in nature.
Siphoning management		✓	✓	✗	✓	✓	✗	✓	Miniature valves are the best when it comes to the problem of the siphoning effect, as they circumvent the issue entirely.
Events Recognition		✓	✗	✗	✗	✓	✗	✗	The electromechanical shunt can recognize coughing and sneezing events that lead to ICP spikes.
Ranged pressure settings		✓	✓	✗	✗	✗	✗	✗	Revisions of passive shunts must be conducted manually in the clinic, while the revision for electromechanical shunts is conducted wirelessly.

7.3 The Wearable Device

The ideal method to test the usability of the wearable device to identify and detect gait pattern changes related to NPH is through patient trials. The second-best option is to conduct a functionality test on the wearable device, as this can showcase the device's ability to produce accurate data. Performance evaluation is carried out by comparing the developed device against other devices used in the literature.

7.3.1. Wearable Device Validation

The most crucial step is the validation of the device readings, where its ability to deliver accurate data is tested and confirmed. Furthermore, the calibration conducted during prototyping – section 6.3 – relied only on the static gravity test, which can be accurate to an extent. However, the calibration during the experimental testing of the device is more accurate as it is conducted using different levels of acceleration (g).

Accelerometers are usually tested using what is called a vibration testing and analysis system, also termed the “shaker” test. The shaker is a device that delivers vertical measured oscillation. The shaker used to test the wearable device is the K2004E004 miniature shaker – showcased in Figure 7.6 – that PCB PIEZOTRONICS produces since it is an ideal shaker for testing low g systems as the wearable device has a low range of ± 3.7 g. The wearable device is glued to the platform that supplies this vertical oscillation. The g data resulting from the sensor is then compared to the shaker’s supplied oscillation. Figure 7.7 shows the wearable device axes orientation when it is attached to a patient's ankle. Three separate tests are conducted for each one of the three axes.

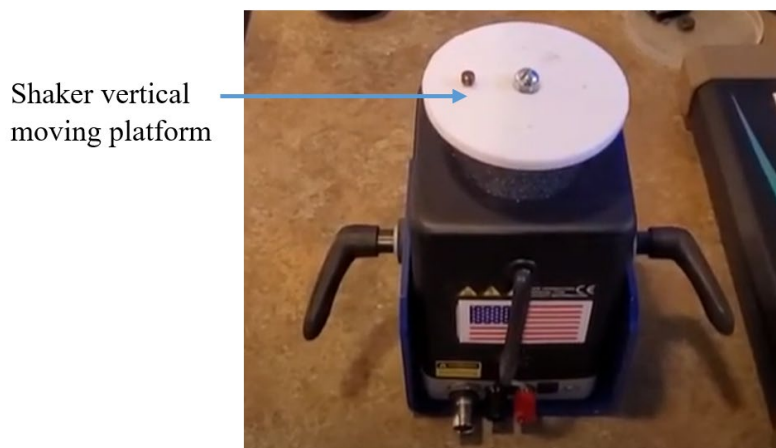


Figure 7.6: K2004E004 miniature shaker. The wearable device is attached to the moving platform

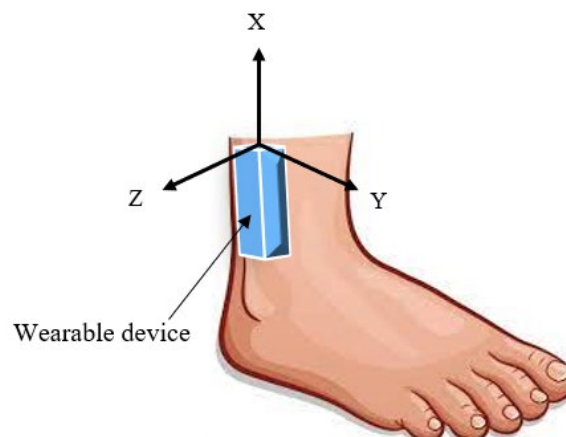


Figure 7.7: Wearable device axes orientation

The normal shaker test procedure consists of attaching two accelerometers to the moving platform, the one that requires testing and a high precision already calibrated reference accelerometer. The results of both accelerometers' outputs are compared with those of the shaker oscillation and each other. For this to be possible, both accelerometers must be hardwired to the shaker control module as this enables the three acceleration data sets to be in

sync with each other, which means that they can be compared together in a single time and acceleration graph. However, the wearable device to be tested streams data wirelessly and does not have the hardware required to link it to the shaker control unit. That means the normal test procedure will produce two separate profiles, which are the shaker and reference accelerometer and the wearable device profile. Hence, the comparison between the two profiles is going to be strictly visual, which can be problematic since the differences between them can be too small to assess visually.

A different testing procedure was used to work around this sync issue. The shaker was set to deliver vertical oscillation at a frequency of 5 Hz and a magnitude of 2 g. The resulting movement profile is an almost ideal sine wave. The wearable device is placed on the moving platform, delivering this sine wave oscillation to the sensor. After that, the output voltage data – which correlates to the resulting acceleration – is gathered wirelessly from the wearable. The accelerometer results are then compared to a mathematically generated sine wave of the same magnitude and frequency as the shaker's vertical oscillation. This solves the issue of syncing the two data sets. The test was conducted three times, where one of the three axes was positioned parallel to the oscillation direction each time.

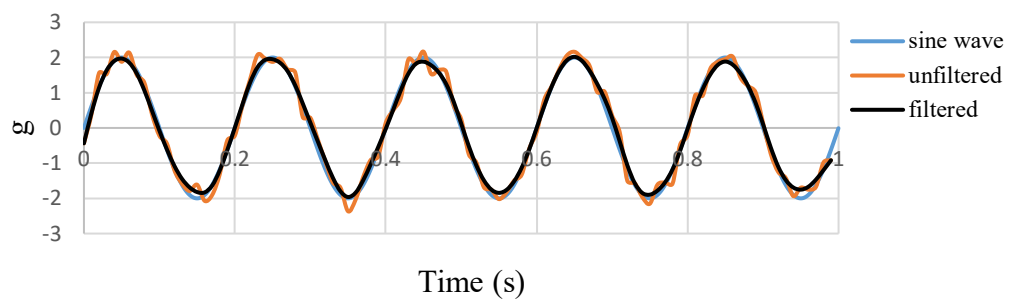
The voltage output of each axis is obtained during the shaker test and then post-processed for calibration purposes. This process includes the calibration of each axis's sensitivity and each axis's 0 g voltage. The offset values showcased in Table 6.1 are based only on the static gravity test conducted during prototyping and are not considered very accurate. These parameters are adjusted so that the resulting g from the gathered voltage data matches the generated sine wave. The parameters were calibrated to the values showcased in Table 7.5 and used to produce Figures 7.8, 7.9, and 7.10. They showcase the five cycles results obtained from the wearable device's X, Y, and Z axes.

The data obtained from the wearable device is filtered using a digital low pass filter of the fifth order and a cut-off frequency of 20 Hz. The filter was implemented using MATLAB, which is a mathematical modelling package. The resulting X-axis unfiltered g profile of the wearable device – Figure 7.8a – seems to match the generated sine wave where the seen discrepancies are assumed to be due to noise embedded within the signal. This is further confirmed as the filtered g profile is an almost ideal match to the sine wave. Figure 7.8b showcases a closer look at the unfiltered and filtered g profile to further showcase their profiles compared to the generated sine wave. Figures 7.9 and 7.10 showcase similar results where both the unfiltered Y- and Z-axis profiles match the generated sine wave profile. It is also noticed that the filtered profiles are an almost ideal match to the sine wave.

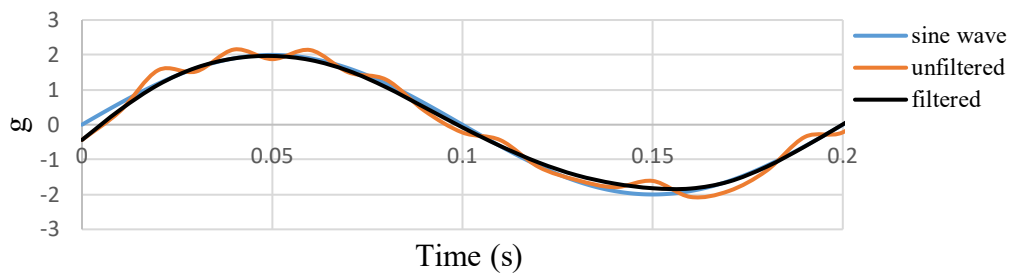
It can be noticed that the unfiltered signal irregularity is more present in the X-axis results – Figure 7.8 – compared to the other two axes. This is assumed to be a result of not only the embedded noise but also a result of the presence of resonance during testing. The device was attached to the shaker where its length protruded from the moving platform during the test since the X-axis is parallel to the length – Figure 7.7 – of the wearable device. This causes the device to exhibit minute resonance along its length, which is picked up by the device as signal noise. The other two axes do not seem to encounter this issue as they are attached to the shaker without having a significant part of the device protruding from the platform. This is a well-documented issue when it comes to the vibrational analysis of accelerometers, which is why it is always recommended that the accelerometer is attached as close as possible to the shaker's platform [151,152].

Table 7.5: Calibration values for the used accelerometer

Axes	Sensitivity	0 g Voltage
X-axis	300 mV/g	1.592 V
Y-axis	310 mV/g	1.638 V
Z-axis	307 mV/g	1.638 V

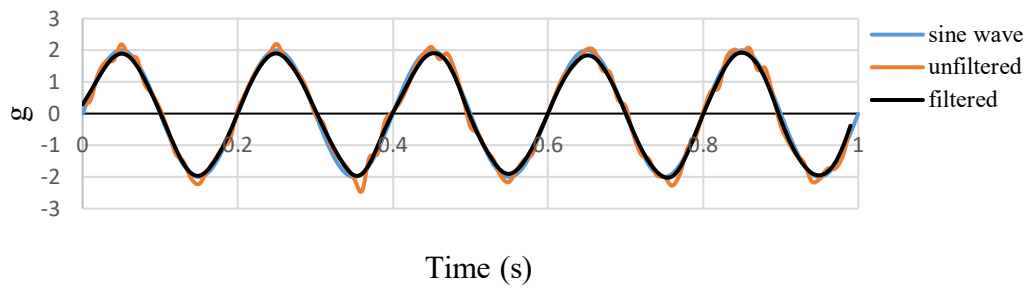


(a)

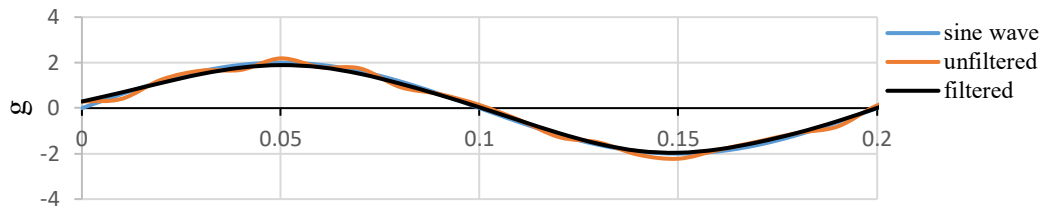


(b)

Figure 7.8: Acceleration results of the X-axis shaker test. (a) A 5-cycle g profile. (b) A single cycle g profile

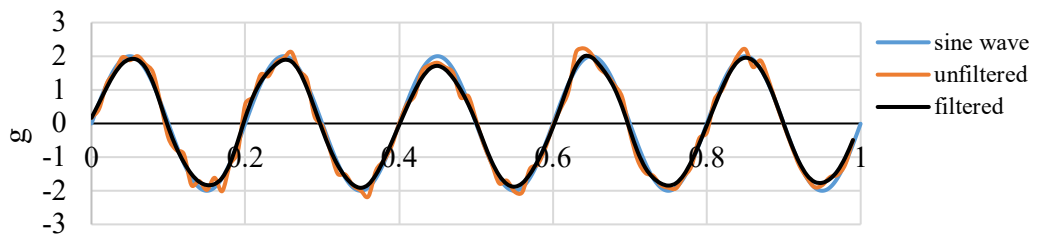


(a)

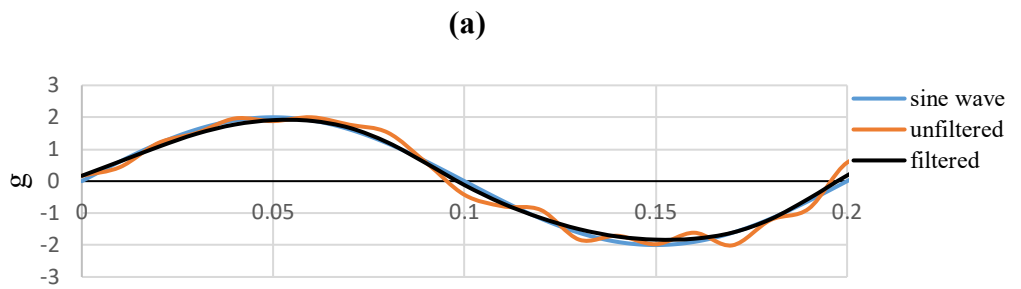


(b)

Figure 7.9: Acceleration results of the Y-axis shaker test. (a) A 5-cycle g profile. (b) A single cycle g profile



(a)

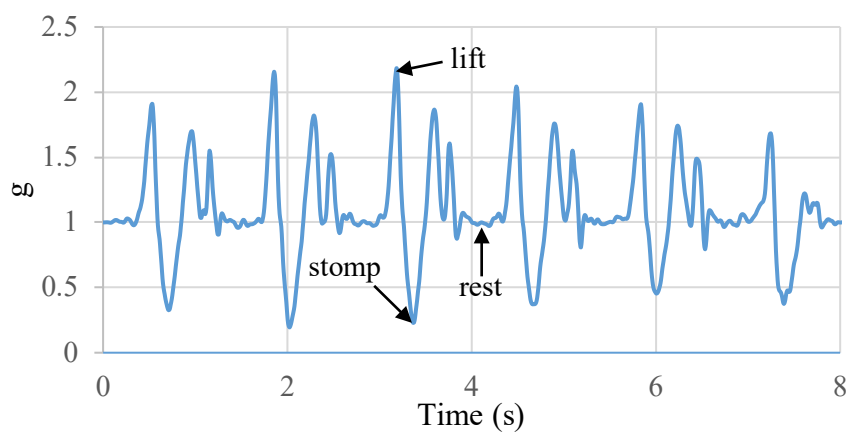


(b)

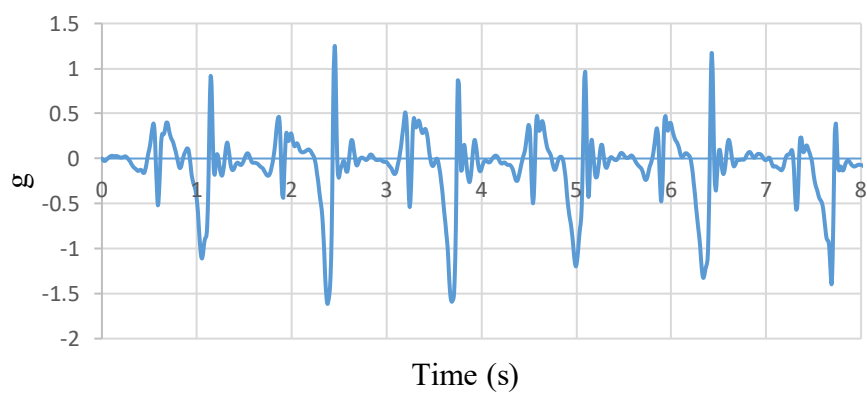
Figure 7.10: Acceleration results of the Z-axis shaker test. (a) A 5-cycle g profile. (b) A single cycle g profile

Based on the results discussed, it can be concluded that the wearable device output is valid as it provides accurate acceleration data. However, an NPH patient trial is still required to validate the diagnosis ability of this evidence as the vibrational analysis test conducted is considered a functional validation. A gait analysis sample is obtained to assist in showcasing the PCB functionality. The sample is provided to showcase that the device can identify a clear gait pattern and that it is probable that it can identify any change or disorder to that pattern in the case of NPH patients. The PCB is attached to the ankle with the same orientation shown in Figure 7.7. The random gait sample readings in Figure 7.11 showcase the gait's obvious periodic nature in the X- and Y-direction. A normal gait is sectioned into three phases, which are lift motion, stomp motion, and rest phase. Although an NPH patient is not restricted to these phases, it is important to examine how these phases translate in terms of the accelerometer readings. This assists in identifying the start and end of each step cycle, as shown in Figure 7.11.

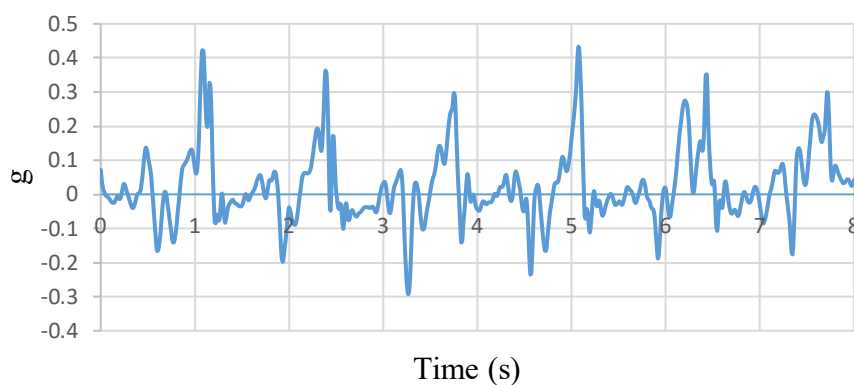
The rest phase g measurement in the X-direction – Figure 7.11a – is 1 (gravity) as the axis is parallel to the gravity direction. Note how when the lift phase starts, the acceleration is in the same direction as gravity, causing the measured g to increase. As the stomp phase starts, negative acceleration causes the measured g to reach roughly a zero. Based on the expected X-axis readings, the start and end of the step cycle are identified. For g in the Y-axis showcased in Figure 7.11b, significant acceleration occurs when the front moving motion of the foot happens. This axis is not parallel to the direction of gravity, so its rest status measurement is zero. The three gait sections cannot be applied to the Z-axis profile. However, a clear cycle can be identified in Figure 7.11c. This is considered the motion resulting from the side-to-side shuffle that occurs during the gait. This is considered an important profile as the gait associated with NPH patients is often described as a shuffle.



(a)



(b)



(c)

Figure 7.11: Gait pattern filtered readings. (a) Accelerating readings in the X-direction. (b) Acceleration readings in the Y-direction. (c) Acceleration readings in the Z-direction

7.3.2. Wearable Device Evaluation

The evaluation of the wearable NPH device is related to specific specifications that can help deliver accurate data. Comparisons between the introduced NPH wearable and the devices available in the literature are carried out below.

a. Device Setup

Accelerometers are more suited for gait measurements as they provide a more suitable g readings data type compared to the angular values provided by gyroscopes. Sensors with multiple axes provide more data than those with a single one. For example, a 3-axis gyroscope can provide data that describes the status of the gait better than a single-axis accelerometer. The introduced NPH wearable device and Hickey et al. [76] utilise a 3-axis accelerometer to gather data on all three planes from a single reference point. Tong and Granat's [71] device provides the least reliable data of the wearables reviewed as a result of its single-axis gyroscope. Gafurov et al. [73] used two 2-axis accelerometers to measure readings on the same axes. Although this adds the benefit of having two reference points, it still neglects measurements from the third axis. Bamberg et al. [74] and Tao et al. [77] have a similar setup consisting of 2-axis accelerometers and single-axis gyroscopes. However, Tao et al. [77] sensors gather readings from different locations and axes to ensure a more comprehensive set of data is obtained. Thus, their device is considered the best performer in terms of setup compared to the other wearables.

b. Sensitivity

In terms of sensitivity, Gafurov et al. [73] and Bamberg et al. [74] devices possess the highest voltage-to-gravity sensitivity of 350 mv/g. The introduced NPH device has the second-best sensitivity of 300mV/g. The least sensitive device of the wearables reviewed is

Hickey et al. [76], a device with a sensitivity of 60 mV/g. Wearables that utilise gyroscopes cannot be used as a comparison since different units are used to evaluate their sensitivity.

c. Range

The wearable device that offers the top g range is Hickey et al. [76], as it can measure up to ± 8 g. While the developed NPH gait device has the second-highest range of ± 3.7 g, the significant difference between its range and that of Hickey et al. [76] device must be noted. The rest of the wearables reviewed – the ones that utilise an accelerometer - possess a range of only ± 2 g. Devices that utilise gyroscopes also cannot be used as a comparison as a result of measurement unit differences.

d. Location

Tao et al. [77] device consists of sensors placed on three different reference points, including the foot, knee, and hip. This means that a more comprehensive quality of data is obtained. The rest of the devices reviewed – including the developed NPH device – have sensors placed in the ankle/foot except for Hickey et al. [76], as their sensor is placed on the lower back. The ankle/foot is the area where g fluctuation is heightened in terms of gait measurement, and that is why it is considered a better sensor placement position for a single reference point device.

e. Sampling Rate

The max sampling rate of the devices reviewed – including the developed NPH device – is 100 Hz. Gafurov et al. [73] device has a sampling rate of 16 Hz, which is the lowest of the reviewed devices. This is an important parameter since a high sampling rate provides gait patterns with higher definition.

The accelerometer used on the NPH device provides g readings on all three axes, meaning that a single sensor is sufficient to provide inclusive data. There is a trade-off between the range and the sensitivity of accelerometers. An accelerometer of median range and sensitivity is used as it is ideal for the application at hand. The accelerometer is sensitive enough to provide accurate data – as seen in Figures 7.8, 7.9, and 7.10 – and has enough range to carry out gait analysis, as showcased in Figure 7.11. Sensor placement is very important as the ankle is chosen since it is the area where g values are heightened. The sampling rate is important as the higher it is, the more accurate the data obtained is. However, the capability of both the sensor and the microcontroller means that there is a cap to that sampling rate.

A summary of the specifications of the wearable device compared to other devices used in the literature is showcased in Table 7.6. This device's main advantage is its high V/g sensitivity, which is apparent from the accurate readings obtained from the shaker test. This corresponds to the device's main drawback of a median g range, as the lower the range, the higher the obtained sensitivity. However, the device has a better sensitivity to range balance compared to the other accelerometer-based devices. It is important to note that this device is intended to be used by the patient off-site (outside the clinic) to monitor the progression of their NPH condition. Hence, a simple setup is extremely important, which is why a single sensor attached to a single location is used rather than a complex setup of multiple sensors attached to multiple locations.

Table 7.6: Evaluation of the wearable device. The evaluation is in terms of the specifications required for the devices to produce accurate and usable data

Devices Features	Wearable NPH device	Tong and Granat [71]	Gafurov et al. [73]	Bamberg et al. [74]	Hickey et al. [76]	Tao et al. [77]
Setup	3-axis accelerometer	1-axis gyroscope	Two 2-axis accelerometers	Two 2-axis accelerometers and two 1-axis gyroscopes	3-axis accelerometer	2-axis accelerometer and two 1-axis gyroscopes
Sensitivity	300 mV/g	11 mV/°/s	350 mV/g	350 mV/g and 12.5 mV/°/s	60 mV/g	312 mV/g and 12.5 mV/°/s
Range	±3.7 g	90 °/s	±2 g	±2 g and 150 & 300 °/s	±8 g	±2 g and 300 °/s
Location	Ankle	Ankle	Ankle	Foot	Lower back	Hip, Knee, and foot
Sampling rate (Hz)	100	50	16	75	100	100

7.4 Conclusion

The electromechanical valve validation process is conducted by validating the valve's flow compartment, spring system, and ultrasonic element. The flow compartment CFD simulation was validated by carrying out a mesh independence analysis, proving that the simulation yielded accurate results at a 176,000 cell count. A similar analysis for the spring structural simulation proved that appropriate results were obtained at a mesh of 167,000 cells. Another validation was conducted for the spring structural simulation through a reaction forces (RFs) check, where the RFs obtained from the simulation – shown in Table 7.1 – are found to be equal to forces – Table 5.4 – obtained during the spring initial design. The ultrasonic element design was validated by ensuring that the E (3,1) mode during the design step is indeed an E (3,1) excitation mode. This was achieved by comparing the displacement results obtained from the frequency analysis – Figure 7.3 – to those of Vyshnevskyy et al. [146], as they both showed similar profiles. Through mathematical modelling, the shunt proved that it is capable of combating the hydrostatic pressure associated with the use of passive systems while maintaining an activeness level that is three times higher than those passive systems. The electromechanical shunt's evaluation revolved around general features related to the issues that face HC shunting. The electromechanical shunt showed that it possesses four of these five main features, with its only main drawback being its lack of blockage management.

A vibrational analysis test was carried out to validate the wearable device. The test utilized a shaker that supplied a 5 Hz sine wave vertical oscillation. The device output while it was attached to the shaker was recorded and compared to a mathematically generated sine wave similar to that of the shaker. This was carried out as the device cannot be connected to the shaker's controller, which means its output could not be synced to the shaker's recorded

oscillation. At a 0 g voltage of 1.5923 V for the X-axis and 1.6385 V for the Y- and Z-axis, the device proved that it could provide accurate g data, as showcased in Figures 7.8, 7.9, and 7.10.

An experiment was intended to be carried out on NPH-suspected patients at the Walton Centre for Neurology and Neurosurgery. However, at the time this work was being conducted, the COVID-19 virus became a global epidemic. As a result, accessibility to the patients became complicated as they are in a high-risk category due to their age. A detailed protocol for the trial is available in Appendix-10.

Chapter 8

CONCLUSION

8.1 Conclusion

This study aimed to design an agile and active HC management framework that is capable of addressing and combating the challenges, shortcomings, and failures of the currently used CSF shunting systems and to further knowledge on hydrocephalus management. These shortcomings are fundamental and are a direct result of the nature of the systems currently being used. An active shunting concept – shown in Figure 3.4 – based on a closed-loop system was proposed to address these issues. The system utilises a proximal catheter-mounted micro piezoelectric-based pressure sensor, a piezoresistive-based 3-axis accelerometer, a 3.9 V lithium cobalt-based oxide rechargeable battery, a control unit, and a drainage algorithm that is also responsible for fault detection. The last component is the electromechanical controllable valve, which is responsible for diverting CSF. A dynamic analysis was conducted to further understand the difference between automated valves and passive valves in terms of how they manage ICP and CSF drainage. Results showed that while automated valves can combat hydrostatic pressure, passive valves can be up to three times more operationally active than automated valves, causing a smoother pressure profile output. Based on these results, it was decided that a hybrid system that utilises both the advantages of automated and passive valves is needed. It was concluded that the combination of a piezoelectric ultrasonic element and a

ball-in-cone spring mechanism – shown in Figure 4.3 – possessed the most advantages and was chosen as the layout for the electromechanical valve.

The design process of the electromechanical valve consisted of a CFD analysis to assess the level of force subjected to the ball in the ball-in-cone mechanism. The spring design was carried out using general design formulas and FEA structural analysis, resulting in spring parameters showcased in Table 5.5. The last step was the design of the ultrasonic element used to control the spring. A modal analysis was conducted on three PZT-5H models of different sizes to obtain their E (3,1) resonance modes. A dynamic FEA analysis was conducted on the selected model, where a voltage input with a frequency equal to the model resonance mode was applied to it. The resulting PZT-5H element provides a 4 nm step definition when supplied with 3.5 V at 294.8 KHz frequency. The valve designed has a range of 10 – 20 mmHg and can drain CSF up to 300 mL/h. Mesh independence analysis shows that accurate results are obtained from both the CFD and spring structural simulations. A reaction force validation showed that the RFs obtained during simulation – Table 7.1 – were equal to those used in the initial design step showcased in Table 5.4. The ultrasonic element E (3,1) mode was validated by comparing the element frequency analysis displacement results to those of Vyshnevskyy et al. [146]. The valve evaluation showcased that the valve offers more features than current passive shunts and those available in the literature, with its main drawback being its lack of blockage management.

An accelerometer-based wearable device was developed for the monitoring and diagnosis of NPH patients. The device consists of an Attiny85 microcontroller, an HC-05 bluetooth module, and an ADXL335 3-axis accelerometer. C++ was used on the device to collect g data, while Python was used on the computer end to receive and plot the data. The assembled device has a range of ± 3.7 g with a 100 Hz sampling rate. A vibrational analysis test using a miniature shaker validated the device's ability to generate accurate acceleration readings when its

sensitivity and 0 g voltage were calibrated on all three axes to the values showcased in Table 7.3. The device range, sensitivity, placement, and multi-axis use show that it may produce more accurate results compared to those used in the literature.

8.2 Limitations

Regarding the electromechanical valve, one important design aspect that needs to be sorted is related to the operation of the ultrasonic element, as it requires to be preloaded. The exact value of the preloading force needs to be determined. However, this can only be achieved using experimental methods. Although the level of preloading can affect the ultrasonic element operation, it is suspected that its impact is minute as the forces the system operates against are very low. This means that the required preloading can be kept at a minimum. It was verified that the simulations conducted produced accurate results. However, experimental validation is required to prove that the produced data is correct and that the valves operate as designed. Also, the proposed valve does not provide a method to combat blockage issues, as the only way to approach the issue is through a miniature pump that was deemed unsuitable for the design. Another issue is related to the gait analysis device, as a trial was intended to be carried out on NPH-suspected patients. Although a functional validation experiment was conducted on the device, the trial is needed to confirm if the device is able to assist in the diagnosis and monitoring of these patients.

8.3 Future Work

Further work must include experimental validation of the designed electromechanical valve, as this is a natural second step in obtaining a concrete proof of concept. The experiment is to assess the operation of the proposed valve in terms of whether it can manage ICP and CSF the same way it was designed to. In addition, required preloading measurements can be carried out, and its effects on the valve operation can be identified. The design of this experiment,

including components and methodology, is showcased in Appendix-11. A trial on NPH-suspected patients is still required in addition to the functional validation performed on the wearable device. The trial can deliver a definitive answer on the usability of the device on the diagnosis of NPH by tracking patients' gait patterns before and after CSF drainage.

References

1. Leinonen V, Vanninen R, Rauramaa T. Cerebrospinal Fluid Circulation and Hydrocephalus. In: Handbook of Clinical Neurology. Vol. 145. Elsevier Inc.; 2018. p. 39–50.
2. Filis K, Aghayev K, Vrionis D. Cerebrospinal Fluid and Hydrocephalus: Physiology, Diagnosis, and Treatment. *Cancer Control*. 2017;24(1):6–8.
3. Pople K. Hydrocephalus and Shunts: What The Neurologist Should Know. *J Neurol Neurosurg Psychiatry*. 2002;2(3):17–22.
4. Venkataramana K. Hydrocephalus Indian Scenario – A Review. *J Pediatr Neurosci*. 2011;6(3):11–22.
5. Isaacs AM, Riva-Cambrin J, Yavin D, Hockley A, Pringsheim TM, Jette N, et al. Age-specific Global Epidemiology of Hydrocephalus: Systematic Review, Metanalysis and Global Birth Surveillance. *PLoS One*. 2018;13(10):1–24.
6. Rekaté L, Blitz M. Hydrocephalus in Children. In: Handbook of Clinical Neurology. Vol. 136. Elsevier Inc.; 2016. p. 1261–73.
7. Jetzki S, Kiefer M, Walter M, Leonhardt S. Concepts for a Mechatronic Device to Control Intracranial Pressure. *IFAC Proc Vol*. 2006;39(16):25–9.
8. Thompson D. Hydrocephalus. *Surg*. 2007;25(12):522–5.
9. Maller V, Agarwal A, Kanekar S. Imaging of Ventricular Shunts. *Semin Ultrasound, CT MRI*. 2016;37(2):159–73.
10. Momani L, Alkharabsheh A, Al-Nuaimy W. Design of an Intelligent and Personalised Shunting System for Hydrocephalus. In: 30th Annual International Conference of the IEEE Engineering in Medicine and Biology Society. Vancouver; 2008. p. 779–82.
11. Momani L, Al-Nuaimy W, Al-Jumaily M, Mallucci C. A Mechatronic Valve in the Management of Hydrocephalus: Methods and Performance. *Med Biol Eng Comput*. 2011;49(1):121–32.
12. Alkharabsheh A, Momani L, Al-Zubi N, Al-Nuaimy W. A Multi-agent Approach for Self-diagnosis of a Hydrocephalus Shunting System. In: 3rd International Conference on Developments in eSystems Engineering. 2010. p. 39–43.
13. Johansson S, Eklund A, Malm J, Stemme G, Roxhed N. A MEMS-based Passive Hydrocephalus Shunt for Body Position Controlled Intracranial Pressure Regulation. *Biomed Microdevices*. 2014;16(4):529–36.
14. Agarwal N, Kashkoush A, McDowell M, Lariviere W, Ismail N, Friedlander R. Comparative durability and costs analysis of ventricular shunts. *J Neurosurg*. 2018;130(4):1252–9.
15. Kameda M, Yamada S, Atsuchi M, Kimura T, Kazui H, Miyajima M, et al. Cost-effectiveness Analysis of Shunt Surgery for Idiopathic Normal Pressure Hydrocephalus Based on The SINPHONI and SINPHONI-2 Trials. *Acta Neurochir (Wien)*. 2017;159(6):995–1003.
16. Tullberg M, Persson J, Petersen J, Hellström P, Wikkelsö C, Lundgren-Nilsson A. Shunt Surgery in Idiopathic Normal Pressure Hydrocephalus is Cost-effective – a Cost Utility Analysis. *Acta Neurochir (Wien)*. 2018;160(3):509–18.
17. Lam S, Srinivasan V, Luerksen T, Pan I-W. Cerebrospinal Fluid Shunt Placement in The Pediatric Population: a Model of Hospitalization Cost. *Neurosurg Focus*. 2014;37(5):1–10.
18. Lim J, Tang A, Liles C, Hysong A, Hale A, Bonfield C, et al. The cost of hydrocephalus: A Cost-effectiveness Model for Evaluating Surgical Techniques. *J Neurosurg Pediatr*. 2019;23(1):109–18.
19. Tinelli M, Guldemond N, Kehler U. Idiopathic Normal-pressure Hydrocephalus: The Cost-effectiveness of Delivering Timely and Adequate Treatment in Germany. *Eur J Neurol*. 2021;28(2):681–90.

20. Momani L, Alkharabsheh A, Al-Zu'bi N, Al-Nuaimy W. Instantiating a Mechatronic Valve Schedule for a Hydrocephalus Shunt. In: 31st Annual International Conference of the IEEE Engineering in Medicine and Biology Society: Engineering the Future of Biomedicine. Minneapolis; 2009. p. 749–52.
21. Alkharabsheh A, Momani L, Ababneh J, Alkharabsheh H, Alhadidi M, Aladwan Y. Diagnosis and Fault Detection of a Mechatronic Hydrocephalus Shunting System. *Aust J Basic Appl Sci.* 2013;7(11):449–57.
22. Elixmann I, Kwiecien M, Goffin C, Walter M, Misgeld B, Kiefer M, et al. Control of an Electromechanical Hydrocephalus Shunt-A New Approach. *IEEE Trans Biomed Eng.* 2014;61(9):2379–88.
23. Narayanaswamy A, Nourani M, Tamil L, Bianco S. A Wireless Monitoring System for Hydrocephalus Shunts. In: 37th Annual International Conference of the IEEE Engineering in Medicine and Biology Society. Milan; 2015. p. 829–32.
24. Momani L, Alkharabsheh A. Programming and Managing Mechatronic Hydrocephalus Shunt : System and Method. *J Biomed Syst Emerg Technol.* 2017;4(2):8.
25. Chung S, Kim J, Wang K, Han D, Chang J. Development of MEMS-based Cerebrospinal Fluid Shunt System. *Biomed Microdevices.* 2003;5(4):311–21.
26. Chappel E. Design and Characterization of a Passive Flow Control Valve Dedicated to The Hydrocephalus Treatment. *Cogent Eng.* 2016;3(1):13.
27. Webster JG, Iskandar B, Medow J, Luzzio C, Zhang X, Guan C, et al. Intracranial Pressure Sensor and Valve to Control Hydrocephalus. In: The Annual International Conference of the IEEE Engineering in Medicine and Biology Society. 2018. p. 3442–8.
28. Oh J, Kim G, Kralick F, Noh H. Design and Fabrication of a PDMS/Parylene Microvalve for The Treatment of Hydrocephalus. *J Microelectromechanical Syst.* 2011;20(4):811–8.
29. Schwerdt H, Bristol R, Chae J. Miniaturized Passive Hydrogel Check Valve for Hydrocephalus Treatment. *IEEE Trans Biomed Eng.* 2014;61(3):814–20.
30. Lee S, Bristol R, Preul M, Chae J. Three-Dimensionally Printed Microelectromechanical-System Hydrogel Valve for Communicating Hydrocephalus. *ACS Sensors.* 2020;5(5):1398–404.
31. Lee S, Liu S, Bristol R, Preul M, Christen J. Hydrogel Check-Valves for the Treatment of Hydrocephalic Fluid Retention with Wireless Fully-Passive Sensor for the Intracranial Pressure Measurement. *Gels.* 2022;8(5):14.
32. Lylyk P, Lylyk I, Bleise C, Scrivano E, Lylyk P, Beneduce B, et al. First-in-human Endovascular Treatment of Hydrocephalus with a Miniature Biomimetic Transdural Shunt. *J Neurointerv Surg.* 2022;14(5):495–9.
33. McAllister J, Williams M, Walker M, Kestle J, Relkin N, Anderson A, et al. An Update on Research Priorities in Hydrocephalus: Overview of The Third National Institutes of Health-Sponsored Symposium “Opportunities for Hydrocephalus Research: Pathways to Better Outcomes.” *J Neurosurg.* 2015;123(6):1427–38.
34. Szczesny S, Jetzki S, Leonhardt S. Review of Current Actuator Suitability for Use in Medical Implants. In: 2006 International Conference of the IEEE Engineering in Medicine and Biology - Proceedings. IEEE; 2006. p. 5956–9.
35. Miethke C. Hydrocephalus Valve. United States; U.S. Patent US6926691, 2005. p. 9.
36. Ludin L, Mauge C. Programmable Shunt with Electromechanical Valve Actuator. United States; U.S. Patent US8123714B2, 2012. p. 16.
37. Toma A. Hydrocephalus. *Surg.* 2015;33(8):384–9.
38. Salih O, Smadi H, Messina M, Mallucci C, Mustafina J, Aljaaf A. Smart shunting and monitoring of hydrocephalus patients. In: Proceedings - International Conference on Developments in eSystems Engineering, DeSE. 2019. p. 861–6.
39. Salih O, Messina M, Al-Jumeily D. An Intelligent Hydrocephalus Shunt: A New Concept. In: 14th

- International Conference on Developments in eSystems Engineering (DESE). 2021. p. 109–13.
40. Salih O, Messina M, Al-Jumeily D. Design of a Piezoelectrically Actuated Hydrocephalus Shunt Valve. *Med Biol Eng Comput.* 2023;61(1):2281–90.
 41. Kahle K, Kulkarni A, Limbrick Jr D, Warf B. Hydrocephalus in Children. *Lancet.* 2016;387(10020):788–99.
 42. Koenig M, Turtzo L. Cerebrospinal Fluid Examination, Monitoring, and Diversion Techniques. In: *Cerebrospinal Fluid in Clinical Practice.* 1st ed. Philadelphia: Elsevier Inc.; 2009. p. 45–53.
 43. Williams MA. Approach to The Patient with Altered Cerebrospinal Pressure Dynamics. In: *Cerebrospinal Fluid in Clinical Practice.* 1st ed. Elsevier Inc.; 2009. p. 259–66.
 44. Chatterjee S, Harischandra L. Cerebrospinal Fluid Shunts – How They Work: The Basics. *Neurol India.* 2018;66(1):24–35.
 45. Chabrierie A, Black PM. Ventricular Shunts. *J Intensive Care Med.* 2002;17(5):218–29.
 46. Chakraborty A, Drake J, Warf B. Methods for Cerebrospinal Fluid Diversion in Pediatric Hydrocephalus: From Shunt to Scope. In: *Schmidek and Sweet Operative Neurosurgical Techniques: Indications, Methods, and Results.* 6th Edit. Philadelphia: Elsevier Inc.; 2012. p. 631–53.
 47. Memorial Sloan Kettering Cancer Center. About Your Ventriculoperitoneal (VP) Shunt Surgery [Internet]. 2022. Available from: <https://www.mskcc.org/cancer-care/patient-education/about-your-ventriculoperitoneal-vp-shunt-surgery>
 48. Ziebell M, Wetterslev J, Tisell M, Gluud C, Juhler M. Flow-regulated Versus Differential Pressure-regulated Shunt Valves for Adult Patients with Normal Pressure Hydrocephalus. *Cochrane Database Syst Rev.* 2013;(5):10.
 49. Ringel F, Schramm J, Meyer B. Comparison of Programmable Shunt Valves vs Standard Valves for Communicating Hydrocephalus of Adults: A Retrospective Analysis of 407 patients. *Surg Neurol.* 2005;63(1):36–41.
 50. Xu H, Wang Z, Liu F, Tan G, Zhu H, Chen D. Programmable Shunt Valves for The Treatment of Hydrocephalus: A Systematic Review. *Eur J Eur Paediatr Neurol.* 2013;17(5):454–61.
 51. Thomale U, Gebert A, Haberl H, Schulz M. Shunt Survival Rates by Using The Adjustable Differential Pressure Valve Combined with a Gravitational Unit (proGAV) in Pediatric Neurosurgery. *Child’s Nerv Syst.* 2013;29(3):425–31.
 52. MIYAKE H. Shunt Devices for the Treatment of Adult Hydrocephalus: Recent Progress and Characteristics. *Neurol Med Chir (Tokyo).* 2016;56(5):274–83.
 53. Aghayev K, Iqbal S, Asghar W, Shahmurzada B, Vrionis F. Advances in CSF Shunt Devices and Their Assessment for the Treatment of Hydrocephalus. *Expert Rev Med Devices.* 2021;18(9):865–73.
 54. Francel P, Stevens F, Tompkins P, Pollay M. The Importance of Valve Alignment in Determining The Pressure/flow Characteristics of Differential Pressure Shunt Valves with Anti-gravity Devices. *Child’s Nerv Syst.* 2001;17(3):163–7.
 55. Sophysa. Sophy Mini SM8 [Internet]. Available from: <http://www.sophysa.com/en/page/valve-introduction-2>
 56. B.Braun. proGAV 2.0 [Internet]. Available from: <https://www.bbraun.com/en/products/b0/miethke-progav-20.html>
 57. Hanak B, Bonow R, Harris C, Browd S. Cerebrospinal Fluid Shunting Complications in Children. *Pediatr Neurosurg.* 2017;52(6):381–400.
 58. Hull J, Harkness W. Common Complications of Cerebrospinal Fluid Shunts. *Curr Paediatr.* 1992;2(2):77–9.
 59. Pickard J, Richards H, Seeley H, Mendez R, Joannides A. UK Shunt Registry Report. UK Shunt Regist.

- 2017;48.
60. Browd S, Ragel B, Gottfried O, Kestle J. Failure of Cerebrospinal Fluid Shunts: Part I: Obstruction and Mechanical Failure. *Pediatr Neurol.* 2006;34(2):83–92.
 61. Panagopoulos D, Karydakis P, Themistocleous M. Slit Ventricle Syndrome: Historical Considerations, Diagnosis, Pathophysiology, and Treatment Review. *Brain Circ.* 2021;7(3):167–77.
 62. Bradley W. Normal Pressure Hydrocephalus: New Concepts on Etiology and Diagnosis. *Am J Neuroradiol.* 2000;21(9):1586–90.
 63. Shprecher D, Schwalb J, Kurlan R. Normal Pressure Hydrocephalus: Diagnosis and Treatment. *Curr Neurol Neurosci Rep.* 2008;8(5):371–6.
 64. Rosseau G. Normal Pressure Hydrocephalus. In: *Encyclopedia of Movement Disorders.* Academic Press; 2010. p. 307–11.
 65. Lieb J, Stippich C, Ahlhelm F. Normal Pressure Hydrocephalus. *Radiologe.* 2015;55(5):389–96.
 66. Vanneste J. Diagnosis and Management of Normal-Pressure Hydrocephalus. *J Neurol.* 2000;247(1):5–14.
 67. Bräutigam K, Vakis A, Tsitsipanis C. Pathogenesis of Idiopathic Normal Pressure Hydrocephalus: A Review of knowledge. *J Clin Neurosci.* 2019;61:10–3.
 68. Song M, Lieberman A, Fife T, Nielsen M, Hayden S, Sabbagh M, et al. A Prospective Study on Gait Dominant Normal Pressure Hydrocephalus. *Acta Neurol Scand.* 2019;139(4):389–94.
 69. Derawi M. Accelerometer-Based Gait Analysis, a Survey. In: *Norwegian Information Security Conference.* 2010. p. 33–44.
 70. Tao W, Liu T, Zheng R, Feng H. Gait Analysis Using Wearable Sensors. *Sensors.* 2012;12(2):2255–83.
 71. Tong K, Granat M. A Practical Gait Analysis System Using Gyroscopes. *Med Eng Phys.* 1999;21(2):87–94.
 72. Williams M, Thomas G, De Lateur B, Imteyaz H, Rose J, Shore W, et al. Objective Assessment of Gait in Normal-Pressure Hydrocephalus. *Am J Phys Med Rehabil.* 2008;87(1):39–45.
 73. Gafurov D, Helkala K, Sondrol T. Biometric Gait Authentication Using Accelerometer Sensor. *J Comput.* 2006;1(7):51–9.
 74. Bamberg S, Benbasat A, Scarborough D, Krebs D, Paradiso J. Gait Analysis Using a Shoe-Integrated Wireless Sensor System. *IEEE Trans Inf Technol Biomed.* 2008;12(4):413–23.
 75. Bora D, Dutta R, Das R, Kumar N. Novel Approach to Gait Angle Measurement using Tri-axial MEMS Accelerometer. In: *International Conference on Innovative Advancements In Engineering And Technology.* Jaipur; 2014. p. 4.
 76. Hickey A, Gunn E, Alcock L, Del Din S, Godfrey A, Rochester L, et al. Validity of a Wearable Accelerometer to Quantify Gait in Spinocerebellar Ataxia Type 6. *Physiol Meas.* 2016;37(11):105–17.
 77. Liu T, Inoue Y, Shibata K. Development of a Wearable Sensor System for quantitative gait Analysis. *Meas J Int Meas Confed.* 2009;42(7):978–88.
 78. Del Din S, Hickey A, Hurwitz N, Mathers J, Rochester L, Godfrey A. Measuring Gait with an Accelerometer-Based Wearable: Influence of Device Location, Testing Protocol and Age. *Physiol Meas.* 2016;37(10):1785–97.
 79. Lutz B, Venkataraman P, Browd S. New and Improved Ways to Treat Hydrocephalus: Pursuit of a Smart Shunt. *Surg Neurol Int.* 2013;4(2):38–50.
 80. Thomale UW. Integrated Understanding of Hydrocephalus — A Practical Approach For A Complex Disease. *Child’s Nerv Syst.* 2021;37(11):3313–24.
 81. Bertrand W, Harper D, Speckman L, Kiehl A, Scheer R. Implantable Cerebral Spinal Fluid Drainage System. United States; U.S. Patent US8292856B2, 2012. p. 8.

82. Kim B, Jin W, Baldwin A, Yu L, Christian E, Krieger M, et al. Parylene MEMS Patency Sensor for Assessment of Hydrocephalus Shunt Obstruction. *Biomed Microdevices*. 2016;18(5):1–13.
83. European Directive 90/358/EEC. On The Harmonised Standards for Active Implantable Medical Devices. 2020.
84. Joung Y. Development of Implantable Medical Devices: From an Engineering Perspective. *Int Neurourol J*. 2013;17(3):98–106.
85. Zhang X, Medow JE, Iskandar B, Wang F, Shokouejinjad M, Koueik J, et al. Invasive and Noninvasive Means of Measuring Intracranial Pressure: A Review. *Physiol Meas*. 2017;38(8):143–82.
86. Zhong J, Dujovny M, Park H, Perez E, Perlin A, Diaz F. Advances in ICP Monitoring Techniques. *Neurol Res*. 2003;25(4):339–50.
87. Popovic D, Khoo M, Lee S. Noninvasive Monitoring of Intracranial Pressure. *Recent Patents Biomed Eng*. 2009;2(3):165–79.
88. Khan M, Shallwani H, Khan M, Muhammad S. Noninvasive Monitoring Intracranial Pressure – A Review of Available Modalities. *Surg Neurol Int*. 2017;8(51):7.
89. Piper I, Barnes A, Smith D, Dunn L. The Camino Intracranial Pressure Sensor: Is it Optimal Technology? An Internal Audit with a Review of Current Intracranial Pressure Monitoring Technologies. *Neurosurgery*. 2001;49(5):1158–65.
90. Roriz P, Frazão O, Lobo-Ribeiro A, Santos J, Simões J. Review of Fiber-optic Pressure Sensors for Biomedical and Biomechanical Applications. *J Biomed Opt*. 2013;18(5):18.
91. Martínez-Mañas R, Santamarta D, De Campos J, Ferrer E. Camino® Intracranial Pressure Monitor: Prospective Study of Accuracy and Complications. *J Neurol Neurosurg Psychiatry*. 2000;69(1):82–6.
92. Zhang X. Intracranial Pressure Sensor. University of Wisconsin-Madison; 2014.
93. Poca M, Martínez-Ricarte F, Sahuquillo J, Lastra R, Torné R, Armengol M. Intracranial Pressure Monitoring with The Neurodur-P epidural Sensor: a Prospective Study in Patients with Adult Hydrocephalus or Idiopathic Intracranial Hypertension. *J Neurosurg*. 2008;108(5):934–42.
94. Antes S, Stadie A, Müller S, Linsler S, Breuskin D, Oertel J. Intracranial Pressure–Guided Shunt Valve Adjustments with The Miethke Sensor Reservoir. *World Neurosurg*. 2018;109:642–50.
95. Welschehold S, Schmalhausen E, Dodier P, Vulcu S, Oertel J, Wagner W, et al. First Clinical Results with a New Telemetric Intracranial Pressure-Monitoring System. *Oper Neurosurg*. 2012;70(1):44–9.
96. Arbour A. Intracranial Hypertension Monitoring and Nursing Assessment. *Crit Care Nurse*. 2004;24(5):19–32.
97. Raboel P, Bartek J, Andresen M, Bellander B, Romner B. Intracranial Pressure Monitoring: Invasive Versus Non-invasive Methods-A Review. *Crit Care Res Pract*. 2012;2012:14.
98. Pascoli G. The Sagnac Effect and its Interpretation by Paul Langevin. *Comptes Rendus Phys*. 2017;18(9):563–9.
99. Li Z, Gao S, Jin L, Liu H, Guan Y, Peng S. Design and Mechanical Sensitivity Analysis of a MEMS Tuning Fork Gyroscope with an Anchored Leverage Mechanism. *Sensors (Switzerland)*. 2019;19(16):19.
100. Zhanshe G, Fucheng C, Boyu L, Le C, Chao L, Ke S. Research Development of Silicon MEMS Gyroscopes: a Review. *Microsyst Technol*. 2015;21(10):2053–66.
101. Passaro V, Cuccovillo A, Vaiani L, De Carlo M, Campanella C. Gyroscope Technology and Applications: a Review in The Industrial Perspective. *Sensors*. 2017;17(10):22.
102. Faisal I, Purboyo T, Ansori A. A Review of Accelerometer Sensor and Gyroscope Sensor in IMU Sensors on Motion Capture. *J Eng Appl Sci*. 2019;15(3):826–9.
103. Yang C, Hsu Y. A Review of Accelerometry-Based Wearable Motion Detectors for Physical Activity

- Monitoring. *Sensors*. 2010;10(8):7772–88.
104. Fiorillo AS, Critello CD, Pullano AS. Theory, Technology and Applications of Piezoresistive Sensors: a Review. *Sensors Actuators, A Phys*. 2018;281:156–75.
105. Georgescu T. Classification of Coughs Using The Wearable RESpeck Monitor. University of Edinburgh; 2019.
106. Fukakusa M, Sto T, Furuhashi H. Use of an Accelerometer to Measure Coughing. *J Japanese Respir Soc*. 1998;36(4):343–6.
107. Bock D, Marschilok A, Takeuchi K, Takeuchi E. Batteries Used to Power Implantable Biomedical Devices. *Electrochim Acta*. 2012;1(84):31.
108. Reddy T. Linden's Handbook of Batteries. 4th ed. New York: McGraw-Hill Education; 2011.
109. Pethig R. Dielectric Properties of Body Tissues. *Clin Phys Physiol Meas*. 1987;8:5–12.
110. Werber D, Schwentner A, Biebl E. Investigation of RF Transmission Properties of Human Tissues. *Adv Radio Sci*. 2006;4:357–60.
111. Gabriel S, Lau R, Gabriel C, Gabriel C, Gabriel S, Corthout E, et al. The Dielectric Properties of Biological Tissues: II. Measurements in The Frequency Range 10 Hz to 20 GHz. *Phys Med Biol*. 1996;41(11):2251–69.
112. Czosnyka M, Czosnyka Z, Agarwal-Harding K, Pickard J. Modeling of CSF Dynamics: Legacy of Professor Anthony Marmarou. *Acta Neurochir Suppl*. 2012;113:9–14.
113. Wakeland W, Goldstein B. A Review of Physiological Simulation Models of Intracranial Pressure Dynamics. *Comput Biol Med*. 2008;38(9):1024–41.
114. Czosnyka M, Czosnyka Z, Momjian S, Pickard J. Cerebrospinal Fluid Dynamics. *Physiol Meas*. 2004;25(5):51–76.
115. Ursino M. A Mathematical Study of Human Intracranial Hydrodynamics Part 1-The Cerebrospinal Fluid Pulse Pressure. *Ann Biomed Eng*. 1988;16(4):379–401.
116. Walter M, Jetzki S, Leonhardt S. A Model for Intracranial Hydrodynamics. In: *Engineering in Medicine and Biology 27th Annual Conference [Online]*. Shanghai, China; 2006. p. 5603–6. Available from: <https://doi.org/10.1109/IEMBS.2005.1615756>
117. Schley D, Billingham J, Marchbanks R. A Model of in-vivo Hydrocephalus Shunt Dynamics for Blockage and Performance Diagnostics. *Math Med Biol A J IMA*. 2004;21(4):347–68.
118. Wakeland W, Goldstein B. A Computer Model of Intracranial Pressure Dynamics During Traumatic Brain Injury That Explicitly Models Fluid Flows and Volumes. *Acta Neurochir Suppl*. 2005;95:321–6.
119. Al-Zubi N. Personalised Shunt Optimisation for The Management and Treatment of Hydrocephalus. University of Liverpool; 2011.
120. Anderson S. Modeling Changes in Brain Pressures, Volumes, and Cerebral Capillary Fluid Exchange: Hydrocephalus. 2004.
121. Kwang W., Chong H. A Review of Microvalves. *J Micromechanics Microengineering*. 2006;16(5):13–39.
122. Spanner K, Koc B. Piezoelectric Motors, an Overview. *Actuators*. 2016;5(1):18.
123. Anjewierden D. An Electrostatic Microvalve for Pneumatic Control of Microfluidic Systems. *Journal of Micromechanics and Microengineering*. University of Utah; 2011.
124. Uchino K. Piezoelectric Ceramics. In: *Handbook of Advanced Ceramics*. 1st ed. Elsevier Inc; 2003. p. 107–59.
125. Uchino K. The Development of Piezoelectric Materials and the New Perspective. In: *Advanced Piezoelectric Materials*. 2nd ed. Elsevier Inc.; 2010. p. 1–85.

126. Marth H, Lula B. Advancements in Linear Piezoelectric Actuator Mechanisms. In: Proc SPIE 7424, Advances in Optomechanics. San Diego; 2009. p. 12.
127. Versteeg H., Malalasekera W. Conservation Laws of Fluid Motion and Boundary Conditions. In: An Introduction to Computational Fluid Dynamics: The Finite Volume Method. 2nd ed. Essex: Pearson Education; 2007. p. 9–38.
128. Zhuming B. Application - Fluid Mechanics. In: Finite Element Analysis Applications. 1st ed. London: Academic Press; 2018. p. 379–45.
129. Felber S. Water Fundamentals Handbook. 1st ed. Minneapolis: DRI-STEEM Corporation; 2017. 55 p.
130. Lindstrom EK, Ringstad G, Mardal K-A, Eide PK. Cerebrospinal Fluid Volumetric Net Flowrate and Direction in Idiopathic Normal Pressure Hydrocephalus. *Neuroimage Clin.* 2018;(20):731–41.
131. Chin W. Pipe Flow Modeling in General Ducts. In: Computational Rheology for Pipeline and Annular Flow. 1st ed. Oxford: Elsevier Inc.; 2001. p. 168–89.
132. Bayston R. Cerebrospinal Fluid Shunts. In: Comprehensive Biomaterials II [Online]. Elsevier; 2017. p. 612–27. Available from: <https://doi.org/10.1016/B978-0-12-803581-8.10083-9>
133. Keulenaer B, Malbraine M, Powell B, Waele J. What is Normal Intra-abdominal Pressure and How is It Affected by Positioning, Body Mass and Positive End-expiratory Pressure. *Intensive Care Med.* 2009;35:969–76.
134. Sanchez N, Tenofsky P, Dort J, Shen L, Helmer S, Smith R. What is Normal Intra-abdominal Pressure. *Am J Surg.* 2001;67(3):243.
135. Thakar SS, Thorat ML, Chaudhari T. Design of The Instrumentation Check Valve. *Int Eng Res J.* 2016;5(7):392–7.
136. Childs P. Springs. In: Mechanical Design Engineering Handbook. 1st ed. Butterworth-Heinemann; 2014. p. 625–75.
137. Simmons C, Maguire D, Phelps N. Springs. In: Manual of Engineering Drawing. 5th ed. Butterworth-Heinemann; 2020. p. 445–60.
138. Marghitu D, Diaconescu C, Craciunoiu N. Machine Components. In: Mechanical Engineer's Handbook. 1st ed. Academic Press; 2001. p. 243–337.
139. Hearn E. Springs. In: Mechanics Of Materials 1. 3d ed. Butterworth-Heinemann; 1997. p. 297–325.
140. Amar K. Bar Element. In: Introduction to Finite Element Analysis Using Matlab and Abaqus. 1st ed. Boca Rotan: CRC Press; 2013. p. 5–57.
141. Li J. Lead-Free Piezoelectric Materials. In: Fundamentals of Piezoelectricity. 1st ed. Berlin: Wiley and Sons; 2021. p. 1–18.
142. Arnau A, Soares D. Fundamentals Of Piezoelectricity. In: Piezoelectric Transducers and Applications. 1st ed. Berlin: Springer; 2009. p. 1–38.
143. Abrahams S, Nassau K. Piezoelectric Materials. In: Concise Encyclopedia of Advanced Ceramic Materials. 1991. p. 351–4.
144. Spanner K, Vyshnevskyy O, Wischnewskiy W. Design of Linear Ultrasonic Micro Piezo Motor for Precision Mechatronic Systems. *Phys Instrumente.* 2005;1–5.
145. Tian X, Liu Y, Deng J, Wang L, Chen W. a Review on Piezoelectric Ultrasonic Motors for The Past Decade : Classification, Operating Principle, Performance, and Future Work Perspectives. *Sensors Actuators A Phys.* 2020;306:23.
146. Vyshnevskyy O, Kovalev S, Wischnewskiy W. A Novel, Single-Mode Piezoceramic Plate Actuator for Ultrasonic Linear Motors. *IEEE Trans Ultrason Ferroelectr Freq Control.* 2005;52(11):2047–53.
147. Atmel. Atmel 8-bit AVR. 2013. p. 203.

148. ITead Studio. Hc-05 Bluetooth to Serial Port Module. 2010. p. 13.
149. Analog Devices. ADXL335 Accelerometer. 2010. p. 16.
150. Zumbahlen H. Analog Filters. In: *Linear Circuit Design Handbook*. 1st ed. Newnes; 2011. p. 581–679.
151. Shokrollahi S, Adel F, Ahmadian H. An Investigation Into The Accelerometer Mounting effects on Signal Transmissibility in Modal Measurements. *Sci Iran*. 2017;24(5):2436–44.
152. Dumont M, Cook A, Kinsley N. Acceleration Measurement Optimization: Mounting Considerations and Sensor Mass Effect. In: *Conference Proceedings of the Society for Experimental Mechanics*. Cham; 2016. p. 61–71.
153. Ferziger F, Perić M, Street R. Solution of the Navier–Stokes Equations: Part 1. In: *Computational Methods for Fluid Dynamics*. 4th ed. Springer; 2020. p. 183–226.
154. Michel A. Ordinary Differential Equations. In: *Encyclopedia of Physical Science and Technology*. 3rd ed. Academic Press; 2003. p. 373–405.
155. Strang G. *Calculus*. 3rd ed. Wellesley Cambridge Press; 2017. 620 p.

Appendix-1: Simulink ICP Model Blocks

These blocks form the general ICP-generating Simulink block in Figure 4.1. They are based on the mathematical model showcased in section 4.2.1. The exact blocks that represent the used equations are showcased below.

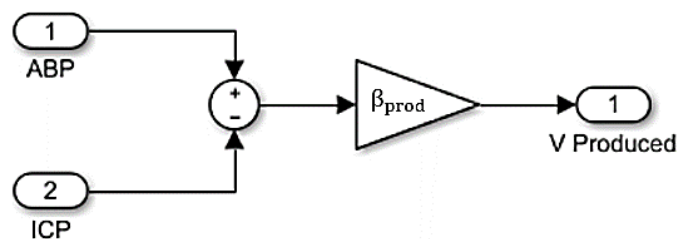


Figure A1.1: CSF production volume block. It represents the V_Production block in the general simulation block and is based on eq 4.3

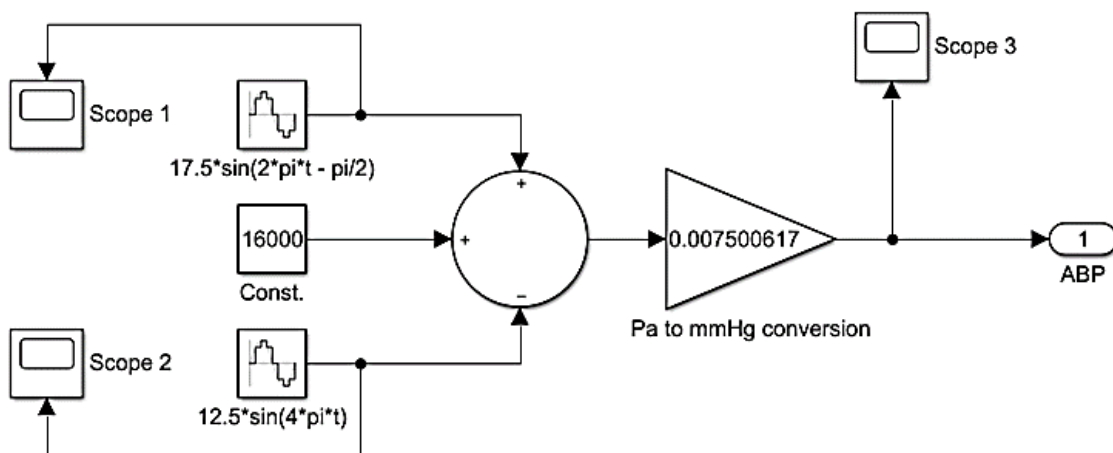


Figure A1.2: ABP sine wave block. It represents the ABP block in the general simulation block and is based on eq 4.4

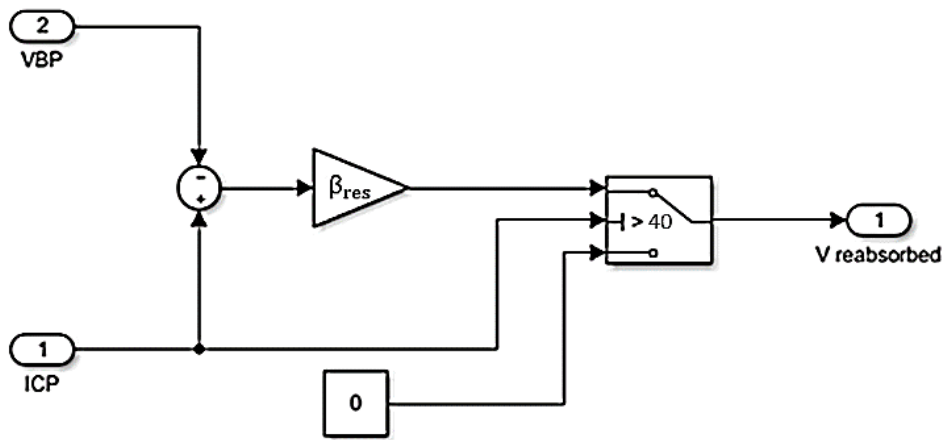


Figure A1.3: CSF reabsorbed volume block. It represents the V_Reabsorbition block in the general simulation block and is based on eq 4.5

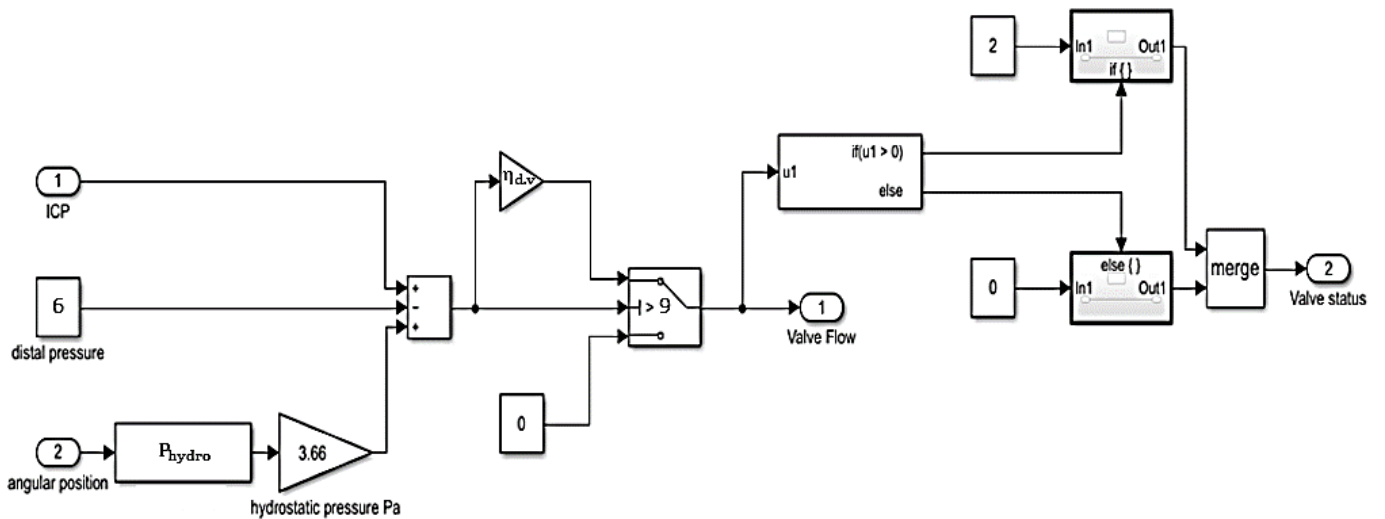


Figure A1.4: Standard valve block. It represents the Standard_Valve block in the general simulation block and is based on equations 4.8, 4.9, and 4.10

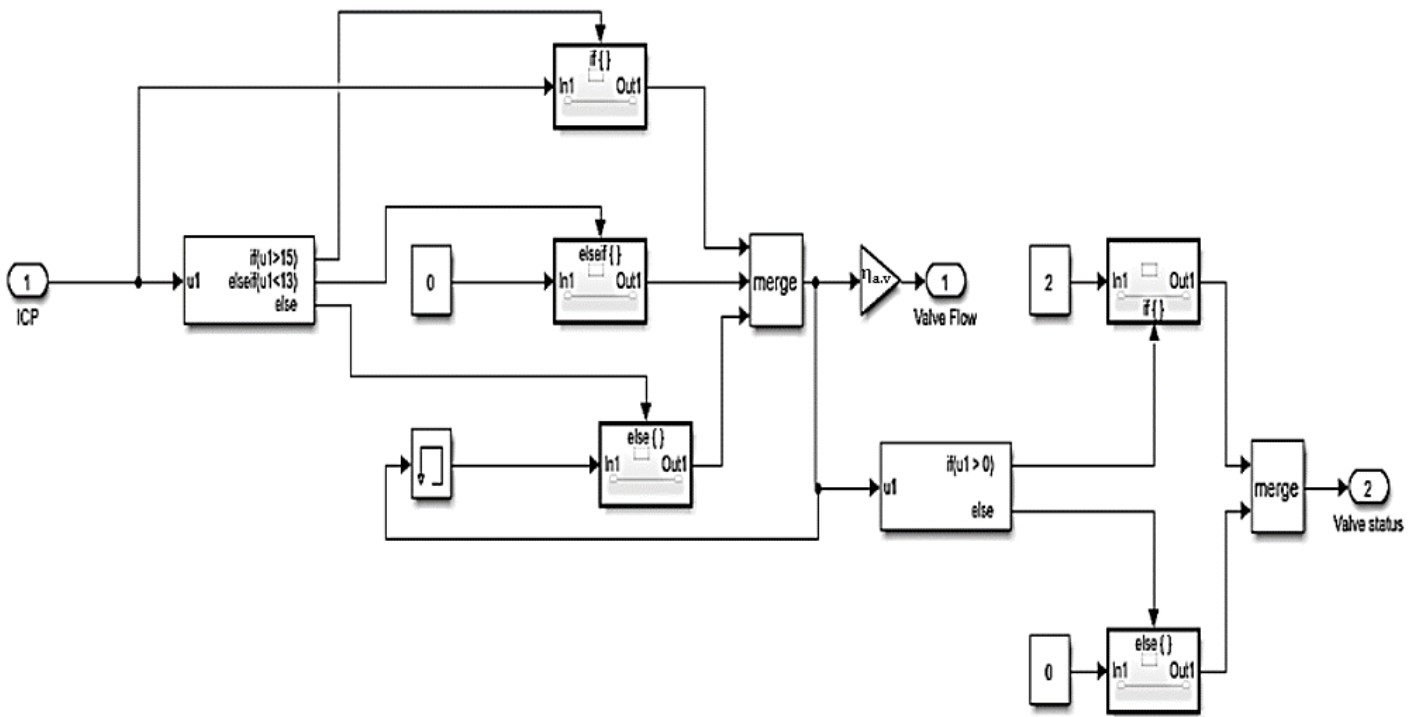


Figure A1.5: Closed-loop valve block. It represents the Closed_Loop block in the general simulation block and is based on eq 4.11

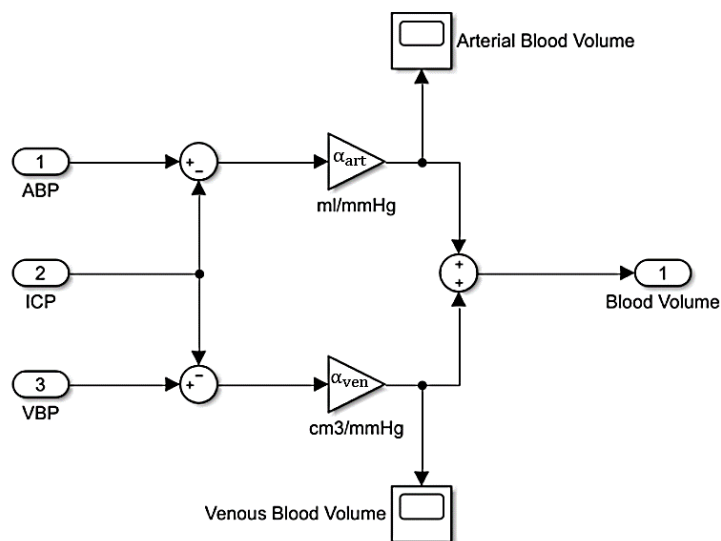


Figure A1.6: Blood volume block. It represents the V_Blood block in the general simulation block and is based on equations 4.12 and 4.13

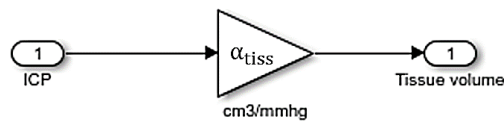


Figure A1.7: Tissue volume block. It represents the V_Tissue block in the general simulation block and is based on eq 4.14

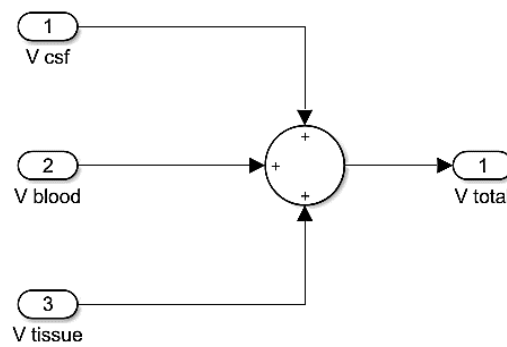


Figure A1.8: Total volume block. It represents the Closed_Loop block in the general simulation block and is based on eq 4.1

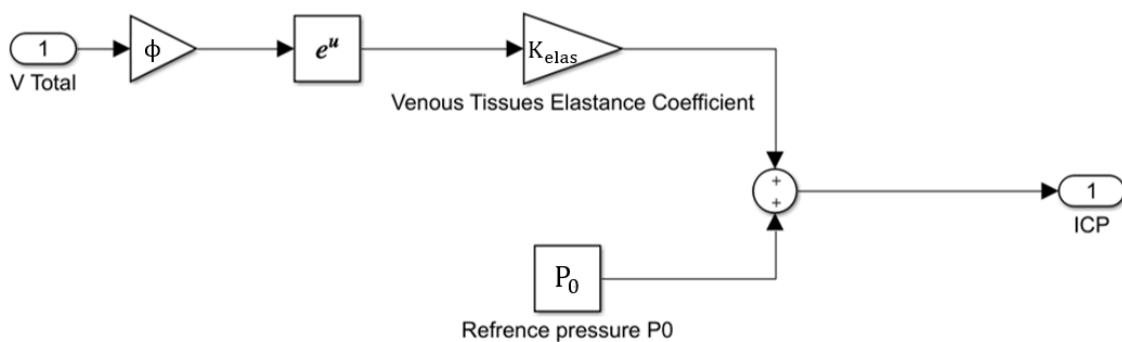


Figure A1.9: ICP and total volume block. It represents the V_Total block in the general simulation block and is based on eq 4.15

Appendix-2: CFD Simulation Methodology

The CFD simulation relies on Navier-Stokes equations – equations 5.1 and 5.2 – showcased in chapter five. These two equations describe the behaviour and motion of fluids as they make use of Newton's second law and apply it to the fluid behaviour. These equations undergo discretization, which refers to the method by which these differential equations can be approached as a set of algebraic equations. The three methods by which this is achieved include the finite difference method (FD), the finite element method (FE), and the finite volume method (FV).

The finite difference method (FD) method is mainly used on geometries that are considered simple. While the finite element (FE) and finite volume (FV) are similar in principle since they break the flow domain into a number of elements (mesh), the majority of CFD simulation packages use the FV method. This includes STAR-CCM+, which is the software used for the flow simulation in this study.

The FV discretization method functions by separating the flow domain into a number of cells (mesh). The governing differential equations are then integrated over those cells. The first step of this method is to introduce the governing equation for the general transport equation – the transport equation is how a scalar quantity is transported through the fluid - of any property or variable, which is given as [128]:

$$\frac{d(\rho \phi)}{dt} + \Delta (\rho \phi \vec{u}) = \Delta (\Gamma \Omega \phi) + S_{\phi} \quad \text{eq A2.1}$$

Where ϕ represents a specific scalar such as pressure or temperature, ρ the fluid density (Kg/m^3), u is the fluid velocity vector (m/s), Γ the diffusion coefficient (m^2/s), and S_ϕ is a source term. Δ is the divergence, which represents the scalar flux leaving or entering the fluid element. Ω is the gradient of the scalar, which points to the direction where the scalar is rapidly increasing. This equation basically represents how a scalar rate of increase is equal to the flux on convection minus the flux of diffusion of that scalar. This equation is then integrated over a 3-dimension controlled volume (V) as [153]:

$$\int_V \frac{d(\rho \phi)}{dt} dv + \int_V \Delta (\rho \phi \vec{u}) dv = \int_V \Delta (\Gamma \Omega \phi) dv + \int_V S_\phi dv \quad \text{eq A2.2}$$

Eq A2.2 can take multiple forms based on the flow type, such as Steady or unsteady convection-diffusion flow. The task of all simulation packages is to find a solution to this equation. The difficult part of CFD analysis is the simulation of turbulence flow. However, the nature of the flow modelled in this study was only laminar, requiring no turbulence models to be used.

Appendix-3: Additional CFD Results

These are samples of the remaining results of the CFD simulation of the valve. Figures 5.3 and 5.4 were showcased earlier as they represent the results for the upper and lower range of the pressures subjected to the system. As discussed in section 5.2, the total number of pressure points simulated is 22. The figures below showcase additional samples of the velocity profile results related to some of these pressure points.

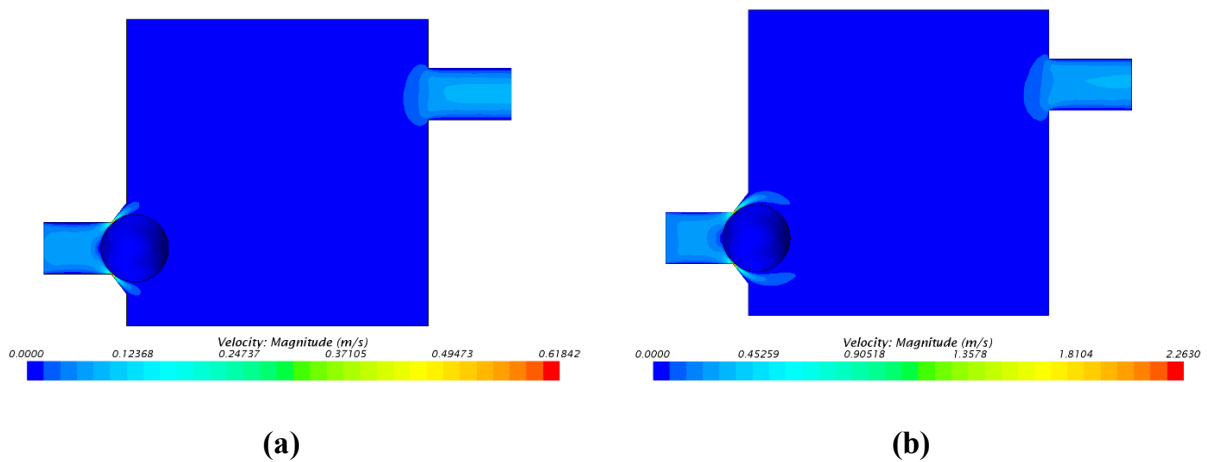


Figure A3.1: CFD simulation results at 12 mmHg. (a) velocity profile at the supine position. (b) velocity profile at the standing position

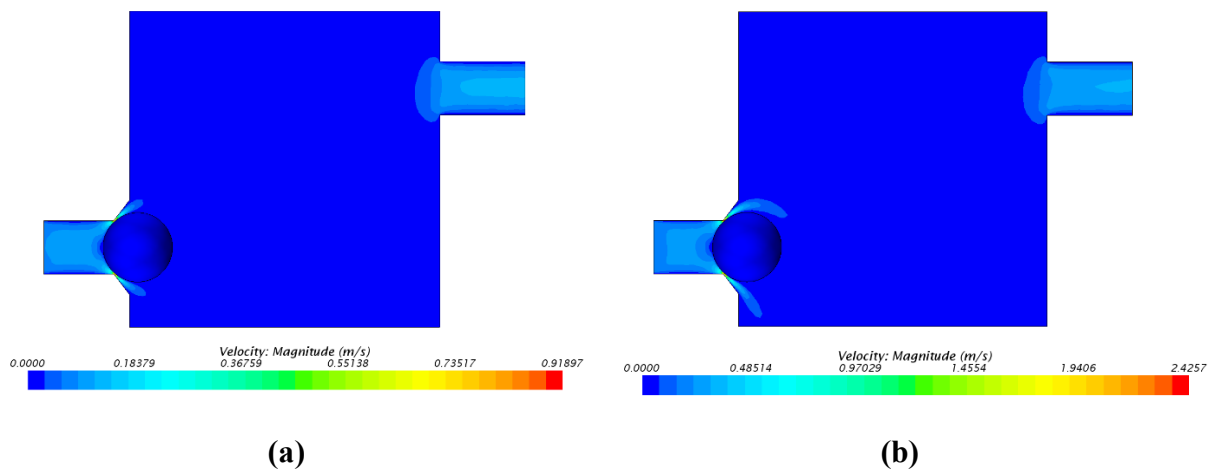


Figure A3.2: CFD simulation results at 15 mmHg. (a) velocity profile at the supine position. (b) velocity profile at the standing position

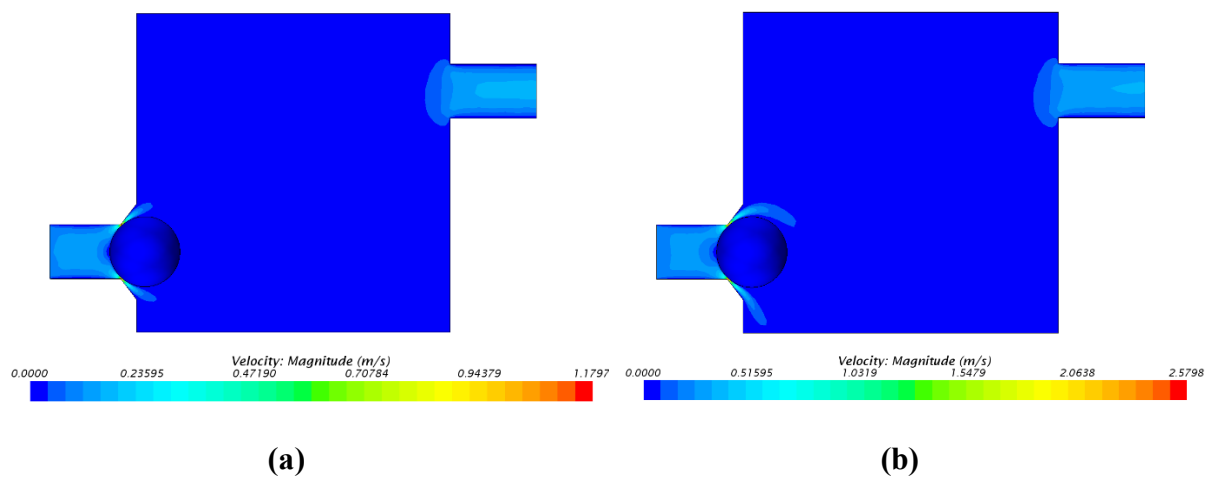


Figure A3.3: CFD simulation results at 18 mmHg. (a) velocity profile at the supine position. (b) velocity profile at the standing position

Appendix-4: Spring Mathematical Model

The general design equations used in section 5.3.1 are based on this model. A simple second-order mass-spring-damper-external force mechanical system is used to describe the spring. Figure A4.1 showcases the model for this system, where B is the dampening factor (N) that represents all dampening effects whether they are mechanical due to spring structure or dampening as a result of fluid flow, K is the spring stiffness (N/m), m is system mass (Kg), $F(t)$ is the external force applied to the system, and x is the displacement of the system due to deformation (m).

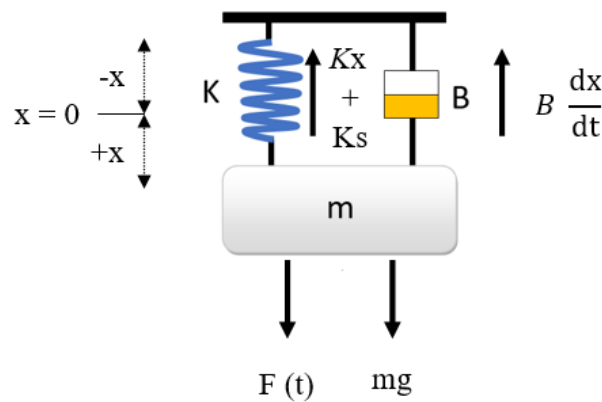


Figure A4.1: Model for the mass-spring-damper mechanical system

Starting with Newton's second law:

$$\Sigma F = m \cdot a \qquad \text{eq A4.1}$$

Where a is acceleration (m/s^2), which is the second derivative of distance leading to the following equation:

$$\Sigma F = m \frac{d^2x}{dt^2} \quad \text{eq A4.2}$$

There are five force components affecting the mass-spring-damper mechanical system. The first is the force created by gravity acceleration (g), which is proportionate to the mass (m). The second is the force exerted as a result of the spring stiffness that actively works in the direction of the spring reference point. It is proportionate to the spring stiffness (K) and spring displacement (x). The third is the force opposing the weight of the mass in order to restore the spring, which is proportionate to spring stiffness and initial starting point displacement resulting from gravity (s). The fourth force component is the damping force that actively works to prevent displacement and is proportionate to the damping factor (B) and velocity ($\frac{dx}{dt}$) of deflection. The last component is the external force applied to the system $F(t)$ [154,155]. An illustration of these components can be seen in Figure A4.1. This leads to the following equation:

$$\Sigma F = mg - Kx - Ks - B \frac{dx}{dt} + F(t) \quad \text{eq A4.3}$$

By setting the reference point as the equilibrium point, the term $mg - Ks$ can be taken as 0. From eq A4.2 and eq A4.3, the below equation is conceived, which is the model used for this system.

$$F(t) = m \frac{d^2x}{dt^2} + B \frac{dx}{dt} + Kx \quad \text{eq A4.4}$$

Appendix-5: Additional Spring Designs

The spring properties calculated and selected in Table 5.5 are based on a wire diameter (d) of 0.06 mm, a mean diameter (D) of 1.8 mm, and the strength properties of Magnesium AZ91E-T6. The tables below showcase some of the other design attempts using different wire and mean diameters and other materials. The red cells on the tables indicate that the property showcased has deteriorated, while a green cell indicates that the property has improved compared to the selected design in Table 5.5.

Table A5.1: Calculated spring parameters for a wire diameter (d) of 0.08 mm. Compared with the selected spring, this diameter provides better stability as it lowers the value of C . However, the spring's natural frequency has also decreased, making the spring susceptible to surge. The number of total coils also increased significantly, which can cause difficulties during manufacturing

Parameter	Value	Parameter	Value	Parameter	Value
K	0.66 N/m	τ_{\max}	14 MPa	δ	2.23 mm
L_f	4.2 mm	N_a	22.5	δ/L_f	0.52
D	1.8 mm	N_T	22.5	L_f/D	2.3
d	0.08 mm	L_L	1.8 mm	F_b	1.917E-05 N
C	22.5	F_L	1.6 E-3 N	m	1.16E-06 Kg
K_w	1.06	τ_L	149 MPa	f_n	378 Hz

Table A5.2: Calculated spring parameters for aluminium 6061-T6. Compared with the selected spring, this material has a shear modulus of 26 GPa, which is higher than Magnesium AZ91E-T6. The spring's natural frequency is less than the selected design, making the spring more susceptible to surge, and the number of total coils also increased

Parameter	Value	Parameter	Value	Parameter	Value
K	0.66 N/m	τ_{\max}	32 MPa	δ	2.23 mm
L_f	4.2 mm	N_a	11	δ/L_f	0.52
D	1.8 mm	N_T	11	L_f/D	2.3
d	0.06 mm	L_L	0.6 mm	F_b	1.917E-05 N
C	30	F_L	2.3 E-3 N	m	3.15E-07 Kg
K_w	1.04	τ_L	514 MPa	f_n	726 Hz

The results showcased represent a sample of the multiple calculations carried out using different materials and different parameters. The selected spring parameters in Table 5.5 proved to provide the best spring parameters.

Appendix-6: Additional Spring FEA Results

The finite element structural analysis results that were used to verify the spring initial design are showcased in section 5.3.2. The figures below showcase additional results for the spring under different operational conditions.

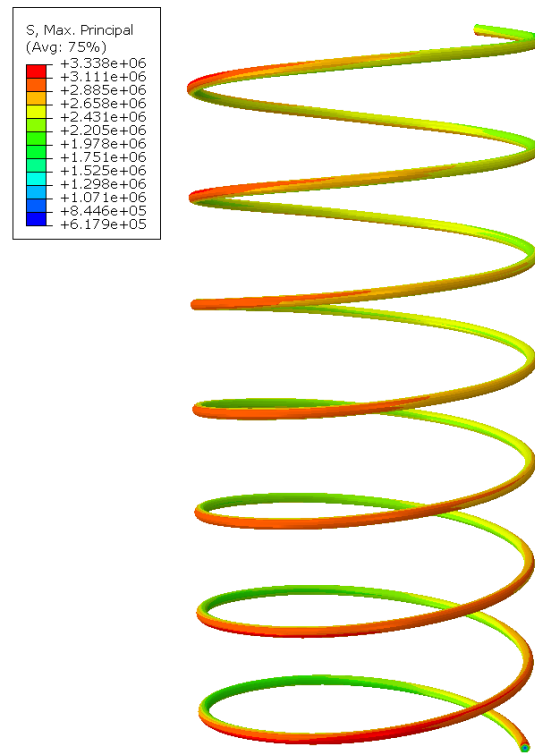


Figure A6.1: FEA principal stress results at 10 mmHg at the supine position

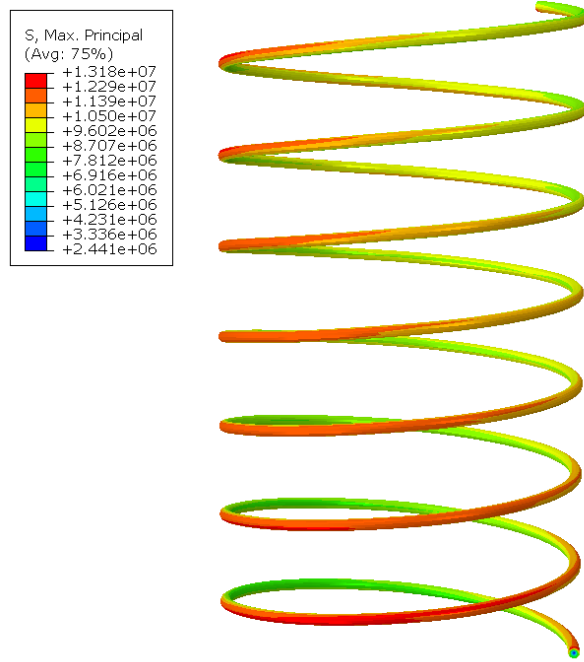


Figure A6.2: FEA principal stress at 20 mmHg at the supine position

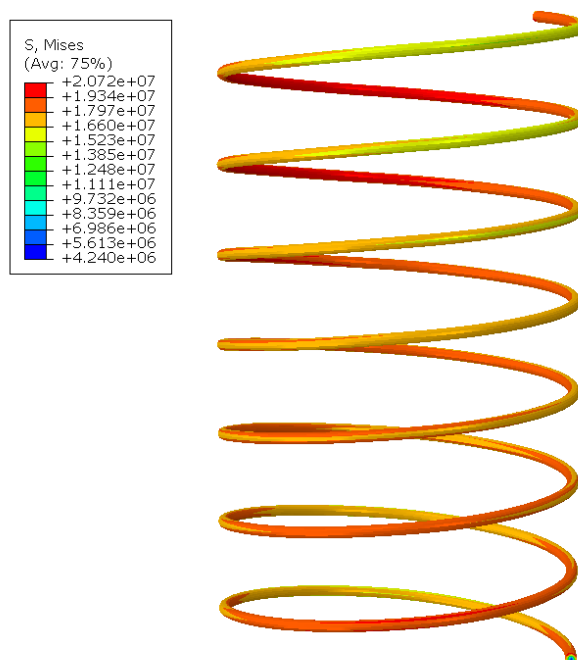


Figure A6.3: FEA von-mises stress results at 20 mmHg at the supine position

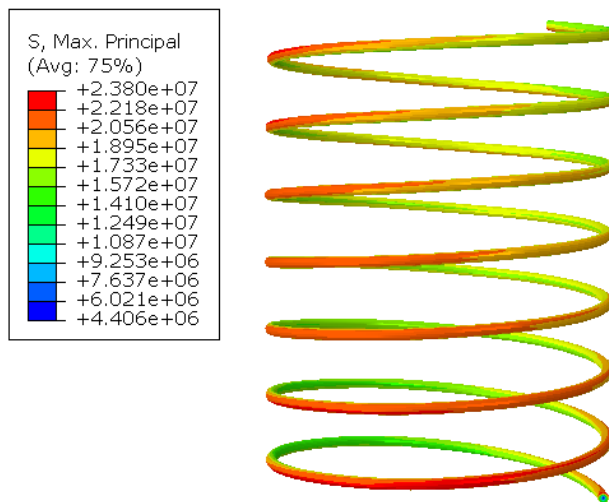


Figure A6.4: FEA principal stress results at 10 mmHg at the standing position

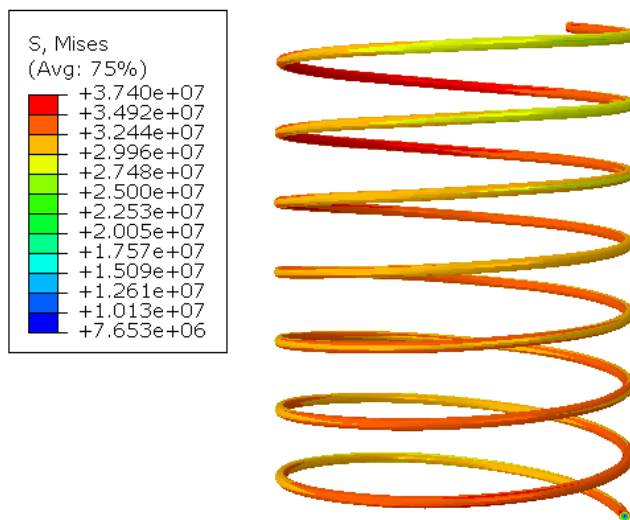


Figure A6.5: FEA von-mises stress results at 10 mmHg at the standing position

Appendix-7: Additional Modal Analysis Results

As mentioned in section 5.4.2, three sheets were used in the modal analysis process. The first 200 resonance frequencies were extracted for all three sheets during this process. These resonance modes are then reviewed until frequencies that produce an E (1,3) mode are identified for each sheet. Figure 5.12 represents the identified E (3,1) modes for the two largest sheets, as no E (3,1) mode was identified for the smallest sheet. Below are samples of these 600 resonance modes that were obtained and reviewed.

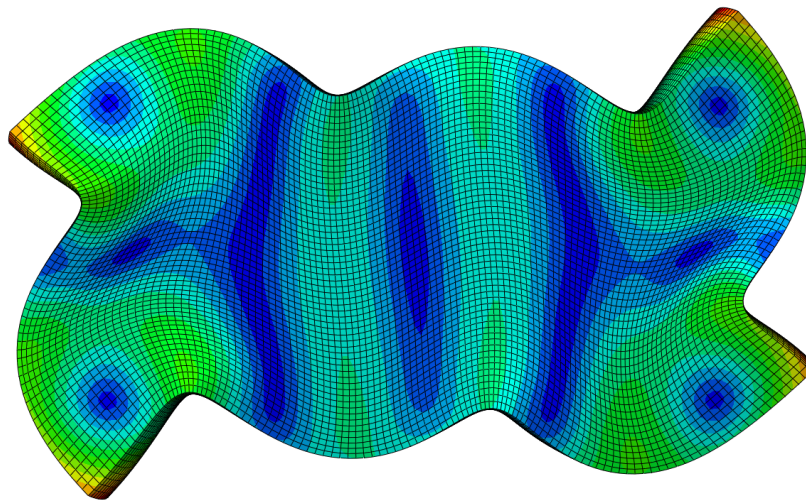


Figure A7.1: Resonance mode of the $7 \times 3 \times 1$ piezoelectric sheet at 318 KHz

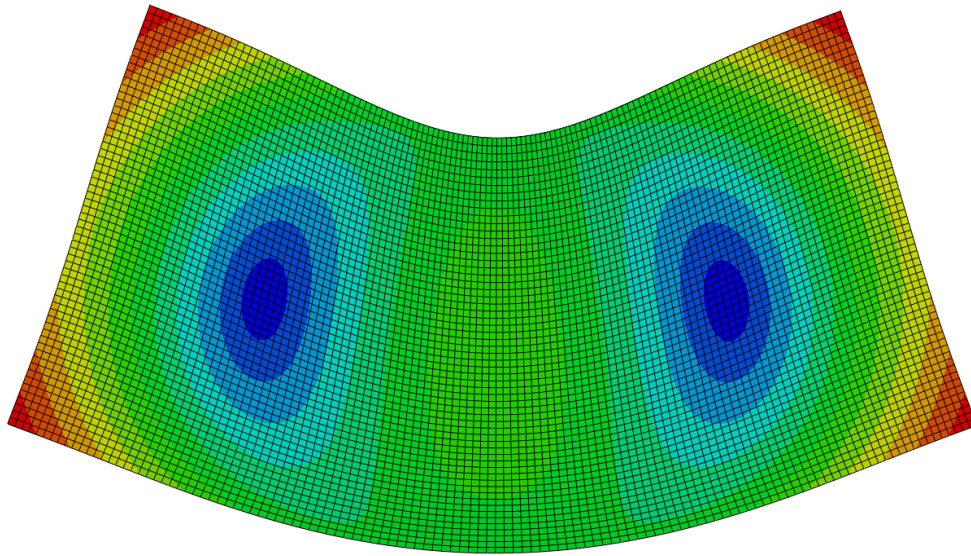


Figure A7.2: Resonance mode of the $13 \times 6 \times 2$ piezoelectric sheet at 81.9 Hz

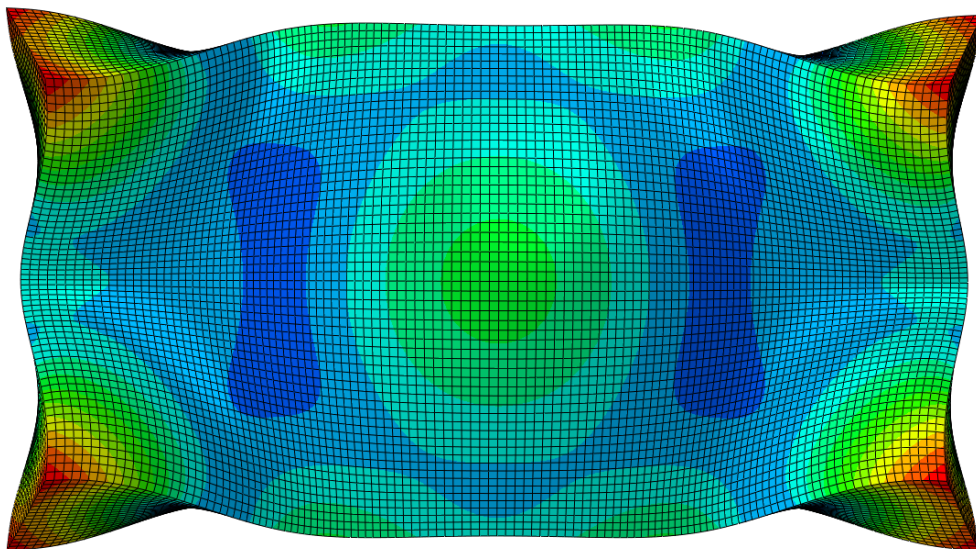


Figure A7.3: Resonance mode of the $20 \times 9 \times 2$ piezoelectric sheet at 143 KHz

Appendix-9: Python Code

```

import bluetooth as b                                #import bluetooth library for connection
import matplotlib.pyplot as plt                     #import matplotlib library for plotting
import numpy as np                                  #import numpy library
import keyboard as k                                #reading and writing library
import csv

print("")                                           #visual output to signal code start-up
print ('initializing.....')

print ("Searching for devices...")                  #visual output to signal bluetooth search
print ("")
available_devices = b.discover_devices()            #search available bluetooth devices
num = 0
print (" Available devices are:")
for i in available_devices:                          #a loop to print a list of available bluetooth devices
    num+=1
    print (num , ": " , b.lookup_name( i ))
print("")
selection = int(input("select number of desired device >>>>> ")) - 1    #user input their device list number
print ("You have selected", b.lookup_name(available_devices[selection])) #device selection based on user input
device_address = available_devices[selection]        #address of the selected device

print("")
port = 1
sock = b.bluetoothSocket( b.RFCOMM )               #defining an SPP socket
sock.connect((device_address, port))                #establish socket connection to the device
file_name = input("file to be created for data storage >>> ")    #creation of a txt file name
file = open(file_name + ".txt", "w+")                #file creation
stream = 0
command = ""
print ("device ready.....")                          #visual output to signal data gathering start
print("press s to start / p to pause / e to end process")

def plotting():                                     #define a plotting function
    t = []                                           #defining plots variables
    ti = []
    gx = []
    gy = []
    gz = []
    with open(file_name + ".txt", 'r') as csvfile:    #opened the created txt file
        plots = csv.reader(csvfile, delimiter='t')  # link variable to file and identify data dividers
        for row in plots:
            ti.append(float(row[4]))                 #specify each data type within the file
            gx.append(float(row[1]))
            gy.append(float(row[2]))
            gz.append(float(row[3]))

    tr = np.array(ti)                                #define a time counter
    t = tr - ti[0]
    plt.subplot(2, 1, 1)                             #plot x-axis data
    plt.plot(t,gx, label='raw data')
    plt.ylabel('acceleration in x direction (vertical)')
    plt.title('3-axis acceleration pattern')

```

```

plt.legend()

plt.subplot(2, 1, 2)                                #plot y-axis data
plt.plot(t,gy, label='raw data')
plt.xlabel('time (milli-second)')
plt.ylabel('acceleration in y direction (longitudinal)')
plt.legend()

plt.subplot(2, 1, 3)                                #plot z-axis data
plt.plot(t,gy, label='raw data')
plt.xlabel('time (milli-second)')
plt.ylabel('acceleration in y direction (longitudinal)')
plt.legend()
plt.savefig(file_name + ".png")
plt.show()

def data_protocol():                                #received data protocol
    counter = ""                                    #defining variables
    x_g = ""
    y_g = ""
    z_g = ""
    tim = ""
    while True:                                    #data stream loop
        buffer = sock.recv(1)                       #recieve data stream one byte at a time
        if buffer.decode("utf-8") == "s":           #if the current byte is an "s" run the next loop

            while True :                            # counter stream loop
                buffer = sock.recv(1)               #if the current byte is "b" write the counter value
                if buffer.decode("utf-8") == "b":
                    file.write(counter + "\t")
                    break
                counter = counter + buffer.decode("utf-8")
                #finish counter loop
                #add all bytes before "b" to each other

            while True:                             #x acceleration loop
                buffer = sock.recv(1)
                if buffer.decode("utf-8") == "b":
                    file.write(x_g + "\t")
                    break
                x_g = x_g + buffer.decode("utf-8")

            while True:                             #y acceleration loop
                buffer = sock.recv(1)
                if buffer.decode("utf-8") == "b":
                    file.write(y_g + "\t")
                    break
                y_g = y_g + buffer.decode("utf-8")

            while True:                             #z acceleration loop
                buffer = sock.recv(1)
                if buffer.decode("utf-8") == "b":
                    file.write(z_g + "\t")
                    break
                z_g = z_g + buffer.decode("utf-8")

            while True:                             #timer loop
                buffer = sock.recv(1)
                if buffer.decode("utf-8") == "e":
                    file.write(tim + "\n")
                    break

```

```
        tim = tim + buffer.decode("utf-8")
    else:
        continue
    break

while True:
    #keyboard input
    if k.is_pressed("s"):
        command = "start"
    elif k.is_pressed("p"):
        command = "pause"
    elif k.is_pressed("e"):
        command = "exit"

    if (command == "start" and stream == 0):
        print ("operation started")
        data_protocol()
        stream = 1

    elif (command == "start" and stream == 1):
        data_protocol()
        stream = 1

    elif (command == "pause" and stream == 1):
        print ("operation paused")
        stream = 0
    #terminate and exit
    elif command == "exit":
        break

print ("operation ended")
file.close()
sock.close()
plotting()
```

#active operation loop

#if "s" is pressed on keyboard command is start

#if "p" is pressed on keyboard command is pause

#if "e" is pressed on keyboard command is exit

#if the user start operation and there is no stream

run received data protocol

#if the user start operation and there is stream

Continue with received data protocol

#if the user pause operation and there is stream

#pause stream

#if user ended operation exit the loop

#run the plotting function

Appendix-10: NPH Device Trial Design

This section showcases the NPH patients' trials related to the usability of the gait analysis wearable device discussed in chapter six. The trial design consists of three main sections, starting with recruitment, where requirements are placed to target NPH-suspected patients and remove patients with a history of diseases that already cause a gait disorder. The protocol section discusses how the trial is to be conducted to ensure data accuracy and patient safety. The third section is about general rules regarding the trial. These sections are discussed below as follows:

a) Recruitments

The targeted participant must fulfil the below requirements:

- 1- Clinical or radiographic indication of Idiopathic Normal pressure.
- 2- Symptoms of either urinary incontinence or cognitive impairment.
- 3- No prior or existing shunting.
- 4- No diagnosis of Parkinson's or Alzheimer's disease.
- 5- The participant must be able to give informed consent.

b) Protocol

The experiment is conducted as follows:

I. Pre-test

- 1- The device is to be mounted to the participant's right ankle as low and close to the foot as possible. It is to be mounted and secured using a Strap.
- 2- The device is to be turned on, and a bluetooth connection must be established with the data collection PC.

II. During test

- 1- The participant must walk in a straight line for 10 meters, turning 180⁰ and then walk back for another 10 meters. The first 10 meters are for familiarization, as the data to be used are from the second 10-meter walk.
- 2- The participants must be tested using their normal shoes.
- 3- Participants who use assistive devices (such as canes) are tested using those devices as well.
- 4- For safety, an assistant must walk by their side to provide support if the participant is unstable.
- 5- Notes must be recorded regarding assistive devices, age, height, weight, gender, and whether assistance was provided or not.

III. After test

- 1- Data must be stored and plotted immediately.
- 2- A note of the physician's visual assessment on the gate is to be made.

c) General rules

Additional steps include:

- 1- A total of 10 to 15 participants are to be recruited, and the trials are to be conducted in the span of 6 to 8 months.
- 2- Data must be collected before and after drainage. If the patient is deemed to require shunting, data must be collected after shunting as well.
- 3- Gait patterns before and after drainage are compared for each patient. This, combined with the physician's diagnosis, can determine the device's ability to produce an NPH diagnosis.

Appendix-11: E. Valve Experiment Design

The experiment detailed is designed for an upscaled version of the device. This is carried out to keep the experiment costs at a minimum while obtaining validation and proof of concept.

The experiment setup discussed below is divided into three categories. They are experiment components, methodology, and protocol.

a) Experiment Components

These are all the components required for the experiment to be conducted, including the electromechanical valve, data management equipment, and other hardware components. They are listed in Table A11.1 below.

Table A11.1: Upscaled electromechanical valve experiment components

Components	Cost	comments
Compression Spring	£ 10	<ul style="list-style-type: none"> - It must be upscaled from the original design. This changes the flow pressure values. This must be considered when selecting the pump. - The ball attachment can be 3D printed as it does not have to be metallic.
Piezo ultrasonic element manufacturing (PZT-5H)	£ 1000	<ul style="list-style-type: none"> - Original dimensions can be used as they can easily be ordered. Hence, the designed control voltage and frequency can be used. - It must be tested with preload to see if displacement is affected (it should have a minimal effect as the pressure values used in the experiment are low; hence, low preloading can suffice). - Can be acquired with electrodes installed on them.

Housing manufacturing and assembly	£ 0	<ul style="list-style-type: none"> - It must be upscaled from the original design. - The preload mechanism must be considered when manufacturing the housing. - It can be printed using an LJMU 3D printer. 	
Peristaltic pump	£ 150 - 400	<ul style="list-style-type: none"> - It must be selected based on the upscaled design values, as flow specifications must be selected. 	
Catheters/joints	£ 70 - 100	<ul style="list-style-type: none"> - It must be chosen based on the upscaled housing input and output diameter. - Joints are needed to mount pressure sensors and can be manufactured using 3D printers in LJMU. - Joint sizing must follow the pressure sensor chosen. 	
Pressure sensors x 3 (2PCBFA6G)	£ 100	<ul style="list-style-type: none"> - It requires joints to be mounted on. 	
Printed Circuit Board “Components used should be pin mounted to ensure the PCB assembly is not complicated with the use of surface-mounted components”.	Micro-controller	£ 90	<ul style="list-style-type: none"> - A controller with a high number of I/O pins allows for more control options.
	Battery	£ 20	<ul style="list-style-type: none"> - Although the experiment does not require a battery, voltage levels from a battery are more appropriate since they cancel much extra hardware if power is drawn from the main lines.
	Programming platform (Arduino)	£ 20	<ul style="list-style-type: none"> - Needed for programming the microcontroller.
	Voltage regulator x 2	£ 5	<ul style="list-style-type: none"> - One for PCB input and one for input to both pressure sensors. - It must be chosen depending on the microcontroller and pressure sensor.
	capacitors	£ 5	<ul style="list-style-type: none"> - Required for power stability.
	Solder-able Bread Board	£ 5	<ul style="list-style-type: none"> - It is simpler than building an actual PCB, as there is room for prototyping without ruining components.
Total	£ 1755		

